

EXPERIMENTAL STUDY ON SCOUR AROUND FOUNDATIONS FOR MARINE ENERGY HARVESTING TECHNOLOGIES IN COMPLEX SOILS

FILIFE DA COSTA MIRANDA

Dissertation submitted for partial requirements attendance for the degree on
MASTER ON CIVIL ENGINEERING – HYDRAULICS SPECIALIZATION

Supervisor: Professor Doctor Francisco de Almeida Taveira Pinto

Co-Supervisor: Professor Doctor Paulo Jorge Rosa Santos

Co-Supervisor: Professor Doctor Tiago João Fazerres Marques Ferradosa

2022, SEPTEMBER

MESTRADO EM ENGENHARIA CIVIL 2021/2022

DEPARTAMENTO DE ENGENHARIA CIVIL

Tel. +351-22-508 1901

✉ m.ec@fe.up.pt

Editado por

FACULDADE DE ENGENHARIA DA UNIVERSIDADE DO PORTO

Rua Dr. Roberto Frias

4200-465 PORTO

Portugal

Tel. +351-22-508 1400

Fax +351-22-508 1440

✉ feup@fe.up.pt

🌐 <http://www.fe.up.pt>

Reproduções parciais deste documento serão autorizadas na condição que seja mencionado o Autor e feita referência a *Mestrado em Engenharia Civil - 2021/2022 - Departamento de Engenharia Civil, Faculdade de Engenharia da Universidade do Porto, Porto, Portugal, 2022.*

As opiniões e informações incluídas neste documento representam unicamente o ponto de vista do respetivo Autor, não podendo o Editor aceitar qualquer responsabilidade legal ou outra em relação a erros ou omissões que possam existir.

Este documento foi produzido a partir de versão eletrónica fornecida pelo respetivo Autor.

Aos meus pais,

“The best advice I’ve ever received is, ‘No one else knows what they’re doing either.’”

Ricky Gervais.

ACKNOWLEDGMENTS

To the author's supervisor, Professor Doctor Francisco de Almeida Taveira Pinto, and co-supervisors Professor Doctor Paulo Jorge Rosa Santos, e Professor Doctor Tiago João Fazerer Marques Ferradosa, for the availability, and all the teachings given throughout the author's academic path, also, for providing all the necessary conditions for the development of this dissertation. A special acknowledgement to Professor Doctor Tiago João Fazerer Marques Ferradosa, for the support, motivation, and tireless daily mentoring.

To Eng. João Chambel and Sr Miguel, for all the aid and companionship demonstrated during the laboratory work. To Eng. Mahdi Alemi and Eng. Francisco Taveira Pinto, for the crucial help provided in the bathymetry data processing. To Eng. Tomás Cabral, for the development of the 3D model. Also acknowledge Eng. Ana Bento, for the support and discussion concerning the contents of this document.

An acknowledge is also made to the Marine energy group (CIIMAR) and to the Haedes Portugal Lda. Team, for all the knowledge and experience shared that lead to the development of the present dissertation.

To all the author's friends, for the friendship, support, motivation, and for all the unforgettable moments. They made this journey of 5 year the greatest adventure of the author's life.

Finally, the author acknowledges his mother, father, brother, and the remaining family members, for the unconditional support, effort, sacrifice, and comprehension. Without their unpayable contribution nothing would be possible.

This work was financially supported by: Project POCI-01-0145-FEDER-032170 (ORACLE project), funded by the European Fund for Regional Development (FEDER) through COMPETE2020, Programa Operacional Competitividade e Internacionalização (POCI), and by national funds through FCT/MCTES (PIDDAC); and Project PTDC-ECI-EGC-5177-2020 (POSEIDON project), funded by national funds through FCT – Portuguese Foundation for Science and Technology.



ABSTRACT

Due to an increasing concern and awareness about the effects of fossil fuel energy in the climate change, and an recent increased tension inside the geo-political climate of Europe, a new all-time high interest in alternative renewable energy technologies was reached. Although underdeveloped and understudied, the marine energy harvesting technology sector presents an extremely high potential. Foundation design is a crucial step towards optimization of offshore wind turbines, it accounts for roughly 25% to 34% of the total cost of implementation.

Even though scour mechanisms for monopile foundations have been extensively studied, there is considerable knowledge gaps in scour mechanisms around foundations with complex geometry, such as gravity-based foundation solutions. Furthermore, scour research considering complex soils, such as layered sand, are still scant. In order to increase the short database of scour tests in literature to date for GBF foundations and complex soils, two distinct sets of scour tests were performed. The first set of tests using a simple soil configuration of uniform fine sand including two different foundation models, a monopile model and a GBF model. The second set of tests was performed using a layered soil, with a coarse sand layer over a fine sand layer, also for both foundation models. Most studies and literature in scour phenomena in offshore environment commonly consider the effect of currents in combination with waves. In order to simulate the sea state conditions, the wave and current flume at FEUP was used.

Optimization can also be sought after through hybridization of technologies, such as the deployment of wave energy converters in the vicinity of the offshore wind farms. Studies and literature regarding this type of solutions are very scarce. The current research will also include an innovative laboratory study on the scour effects of the implementation of a wave oscillating wave surge, such as an oscillating wave surge converter, to the bottom, near the foundation of offshore wind turbines. This innovative study was performed in combination with both sets of tests referred before. The oscillating wave surge converter tests extended to three different distances from the foundation.

The present research focuses on three main key areas. Firstly, with the GBF tests, it is intended to expand the current small database of scour tests for complex geometry foundations. Secondly, expansion of existing laboratory scour tests for layered sand soils. Lastly, the present dissertation aims to set a preliminary work and serve as a first step towards further and deeper studies of hybrid solutions towards offshore energy optimization. Results for layered soil indicated an increase in scour depths compared with the uniform fine sand. The test results in the presence of the oscillating wave surge converters indicates an average 60% decrease in scour depth near the foundations.

KEYWORDS: Marine energy, Gravity-based foundation, Scour, Wave Energy Converter, Layered sand.

RESUMO

Devido a uma crescente preocupação e atenção com os efeitos da energia de combustíveis fósseis nas alterações climáticas e a um recente aumento da tensão geopolítica na Europa, um novo pico de interesse em tecnologias alternativas de energia renovável foi atingido. Embora subdesenvolvido e pouco estudado, o sector das tecnologias de conversão de energia marinha apresenta um potencial de desenvolvimento extremamente elevado. O dimensionamento das fundações é um passo crucial para otimização das turbinas eólicas offshore, representando cerca de 24% a 34% do custo total de implantação.

Embora os mecanismos de erosões localizada em fundações do tipo monopilar já tenham sido extensivamente estudadas, existem consideráveis lacunas de conhecimentos nos mecanismos de erosões localizadas junto a fundações de geometria complexa, tais como as fundações por gravidade. Além disso, a investigação de erosões localizadas considerando solos complexos, tais como solo com camadas, é ainda extremamente escassa. A fim de aumentar a atual curta base de dados existente na literatura de testes de erosão localizada em fundações de gravidade, e em solos complexos, dois conjuntos distintos de testes de erosão localizada foram realizados simultaneamente. O primeiro conjunto de testes utilizando uma configuração simples do solo de areia fina, incluindo dois modelos diferentes de fundação, um modelo de monopilar e um modelo de fundação por gravidade. O segundo conjunto de testes foi realizado utilizando um solo por camadas com uma camada de areia grossa sobre uma camada de areia fina, também para ambos os modelos de fundação. A maioria dos estudos e da literatura sobre fenómenos de erosão localizada em ambiente offshore consideram geralmente o efeito das correntes em combinação com as ondas. A fim de simular as condições marítimas, foi utilizada o canal de correntes e ondas do laboratório de hidráulica da FEUP.

Um outro caminho possível para otimização é a implementação de soluções híbridas, como a instalação de conversores de energia das ondas nas proximidades dos parques eólicos offshore. Estudos realizados na literatura sobre este tipo de soluções são praticamente inexistentes. Esta investigação incluirá também um estudo laboratorial inovador sobre os efeitos na erosão localizada da implementação de um conversor de energia de ondas a três distâncias diferentes da fundação.

A presente investigação centra-se em três áreas-chave. Primeiro, com o conjunto de testes em fundações por gravidade pretende-se aumentar a atual pequena base de dados de testes de erosões localizadas em fundações de geometria complexa. Segundo, a expansão dos testes laboratoriais existentes de erosões localizadas para solos por camadas. Por último, a presente dissertação visa estabelecer um trabalho preliminar e servir como ponto de partida para estudos mais aprofundados sobre soluções híbridas de otimização do sector de energia offshore. Os resultados para solos por camadas indicaram um aumento das profundidades de erosão em comparação com a areia fina. Os resultados dos ensaios na presença do conversor de energia de ondas revelaram uma diminuição média de 60% da profundidade erosão localizadas junto das fundações.

PALAVRAS-CHAVE: Energia marinha, Fundações por gravidade, Erosão localizada, Conversor de energia de ondas, Areia por camadas

TABLE OF CONTENTS

ACKNOWLEDGMENTS	i
ABSTRACT	iii
RESUMO	v
1. INTRODUCTION	1
1.1. EUROPEAN WIND SECTOR.....	1
1.2. OFFSHORE WIND OPTIMIZATION.....	2
1.3. MAIN OBJECTIVES.....	2
1.4. DISSERTATION OUTLINE.....	3
2. SCOUR PHENOMENA IN MARINE ENVIRONMENT	5
2.1. Types of fixed bottom foundations for offshore wind farms.....	5
2.2. North Sea complex soil.....	6
2.3. SOIL-FLUID-STRUCTURE INTERACTION.....	7
2.4. BED SHEAR STRESS.....	9
2.4.1. Current induced.....	10
2.4.2. Wave induced.....	11
2.4.3. Combined wave and current induced.....	12
2.5. THRESHOLD OF MOTION.....	13
2.6. AMPLIFIED BED SHEAR STRESS.....	14
2.7. CLEAR-WATER SCOUR AND LIVE-BED SCOUR.....	15
2.8. WAVE CLIMATE.....	16
2.8.1. Regular waves.....	16
2.8.2. Irregular waves.....	17
2.8.3. Breaking point.....	21
2.9. SCOUR DEPTH.....	22
2.9.1. Scour depth for waves.....	23
2.9.2. Scour depth for currents.....	23
2.9.3. Scour depth for combined waves and currents.....	24
2.9.4. Scour Hole.....	24
2.10. SCOUR IN GRAVITY BASED FOUNDATIONS (GBF).....	25

2.10.1. Scour Depth Prediction Under Current.....	25
2.10.2. Scour Depth Prediction Under Waves.....	26
2.10.3. Scour Depth Prediction Under Waves and Currents Combined	26
2.10.4. Transition shapes	27
2.10.5. Shortcomings In Scour Prediction around GBS	27
2.11. SEDIMENT CHARACTERISTICS.....	28
2.12. HYBRID MARINE RENEWABLE ENERGY (MRE) INVESTMENTS.....	28
2.13. SCOUR TESTS REVIEW.....	30
2.13.1. Scour Tests For Monopile Foundation	30
2.13.2. Scour Tests for GBS.....	31
2.14. SCALE AND MODEL EFFECTS	33
3. PHYSICAL MODEL SET-UP.....	37
3.1. LABORATORY SET-UP	37
3.1.1 Flume at Faculty of Engineering of the University of Porto FEUP	37
3.2. FOUNDATIONS AND WEC MODELS	41
3.2.1 Foundation models	41
3.2.2 WEC model.....	44
3.3. SOIL MODELS	44
3.3.1 Uniform fine sand.....	45
3.3.2 Layered sand with upper coarse sand	45
3.4. TARGET HYDRODYNAMIC CONDITIONS	46
3.5. SCALE AND MODEL EFFECTS CONSIDERATIONS.....	47
4. EXPERIMENTAL STUDY.....	49
4.1. FLOW CONDITIONS CALIBRATION.....	49
2.1.1. Velocity Profiles	49
2.1.2. Wave dissipation system	54
2.1.3. Wave analysis tool.....	56
2.1.3.1. Wave probe calibration	57
2.1.3.2. Reflection analysis.....	58
4.2. NEW TARGET CONDITIONS.....	61
4.3 LABORATORY TESTS.....	62

4.3.1 Test plan.....	62
4.3.2 Laser scans	64
4.3.3 Faro SCENE software	67
4.3.4 Point Cloud analysis.....	68
4.3.5 Wave data acquisition	71
4.3.6 Wavemaker software (HR Merlin)	73
4.4 RESULTS, ANALYSIS, AND DISCUSSION	74
4.4.1. Wave data measured	74
4.4.2. Foundation scour depth analysis	77
4.4.3. WEC Scour depth Analysis	81
4.4.4. Scour pattern Analysis	83
4.4.5. Layered sand scour holes analysis	87
5. CONCLUSIONS AND FUTURE WORKS	89
5.1. CONCLUSIONS.....	89
5.2. FUTURE WORKS	90
REFERENCES	91
APPENDIX.....	95

Figures Index

Figure 1 - Total wind energy capacity growth in Europe (WindEurope, 2022b).	1
Figure 2 - Gravity based foundation (Lavanya & Kumar, 2020).....	5
Figure 3 - Monopile foundation (Lavanya & Kumar, 2020).	6
Figure 4 - Multipod Foundation (Tripod and Jacket) (Lavanya & Kumar, 2020).....	6
Figure 5 - Schematic overview of a typical stratigraphy of the southern parts of the North Sea ((Fleischer et al., 2022) adapter from Coughlan et al. (2018)	7
Figure 6-Configuration of flow patterns around monopile foundations (Petersen et al., 2015).	8
Figure 7- Scour pattern around the base of the monopile foundation (Whitehouse, 1998).	8
Figure 8- Boundary layer (Liu, 1998).....	9
Figure 9-Wave induced bed shear stress related to grain size , according to different authors (De Vos et al., 2011).	11
Figure 10- Non-linearity of bed shear stress in combined wave and current interaction (Soulsby, 1997).....	12
Figure 11- Shields diagram (adapted from (Shields, 1936)).	13
Figure 12- Shields diagram adapted by Soulsby (Soulsby, 1997).	14
Figure 13 - Scour development in clear-water and live-bed scour conditions (Brandimarte et al., 2012).....	16
Figure 14 - Wave characteristics - regular linear wave (De Vos, 2008).	16
Figure 15 - Representation of a real irregular wave train (Loosveldt & Vannieuwenhuysse, 2012).	18
Figure 16 - Individual wave identified with zero-down crossing method (Chambel, 2019)	18
Figure 17 - Energy spectral density (De Vos, 2008).	19
Figure 18 -Pierson-Moskowitz and JONSWAP (Abu Husain et al., 2013)	21
Figure 19 - Scour development as function of time ((Fazeres-Ferradosa, 2018) adapted from (Sumer et al., 2001).	22
Figure 20 - Scour hole representation (Fazeres-Ferradosa, 2018).....	24
Figure 21 - Different GBF types (Esteban et al., 2015).....	25

Figure 22 - Scour depth for GBS with different transition shapes (Whitehouse et al., 2011); a)conical transition b)flat-topped transition.....	27
Figure 23 - Oscillating water column (MOREnergy lab, 2022).....	29
Figure 24 - Oscillating wave surge converter (MOREnergy lab, 2022).	29
Figure 25 - Overtopping device (MOREnergy lab, 2022).....	30
Figure 26 - Small scale foundation geometries (Tavouktsoglou, 2018).	32
Figure 27 – Large scale foundation geometries (Tavouktsoglou, 2018).	32
Figure 28 - Layout scheme of FEUP flume (dimensions in meters).....	37
Figure 29 – Flume general views.	38
Figure 30 - Constant head reservoir.....	38
Figure 31 - Structural (left) and electrical (right) components.	39
Figure 32 - Wavemaker main components scheme (Adapted from (Chambel, 2019)).....	40
Figure 33 - Wave generator computer.....	40
Figure 34 - Monopile model.	41
Figure 35 - GBF model dimensions (dimensions in mm).	42
Figure 36 – Isolated parts (left) and final model assembled (right).	42
Figure 37 - First GBF model disintegrated.....	43
Figure 38 - Outside mold (left); and final concrete GBF model (right).....	43
Figure 39 - WEC models.....	44
Figure 40 - SP 55 fine sand grading curve ((Chambel, 2019) adapted from (Silva, 2010))...	45
Figure 41 - Coarse sand grading curve.	46
Figure 42 - ADV and support structure.....	50
Figure 43 - Flowmeter (Left); Adjustable Mechanical gate (Right).	50
Figure 44 – 1st velocity profile.....	51
Figure 45 – 2nd velocity profile.	52
Figure 46 – 3rd velocity profile.	52

Figure 47 – 4th velocity profile.	54
Figure 48 - Upstream box (left); and downstream box (right).	55
Figure 49 - Dissipation system fixed to the flume.	55
Figure 50 - Gravel profile.	56
Figure 51 - Wave analysis tool.....	57
Figure 52 - Reflection analysis probe spacing.....	57
Figure 53 - Wave calibration series (HR DAQ).....	58
Figure 54 - New wave probe spacing.....	60
Figure 55 - Foundation only scour test disposition in fine sand.	62
Figure 56 - Hybrid foundation scour tests disposition in fine sand.	63
Figure 57 - Foundation only scour test disposition for layered soil.	63
Figure 58 - Hybrid foundation scour tests disposition for layered soil.	63
Figure 59 - FARO laser scanner.	64
Figure 60 - Laser scan placement.....	65
Figure 61 - Artificial reference (checkerboard).	65
Figure 62 - Checkerboard placement 1.....	66
Figure 63 - Checkerboard placement 2.....	66
Figure 64 -Checkerboard placement 3.....	67
Figure 65 - Point cloud in the SCENE software.....	68
Figure 66 - Individual clipping boxes (SCENE software).	68
Figure 67 - Cloud to cloud distances tool from CloudCompare software.	69
Figure 68 - CloudCompare color scale interface.	69
Figure 69 - Distance cloud from CloudCompare software.	70
Figure 70 - Laser scan inadequacies.	70
Figure 71 - New proposed laser scan placements.	71

Figure 72 - Wave probe placement.	71
Figure 73 - Data acquisition series (HR DAQ).	72
Figure 74 - Post-processing tool (HR DAQ).	72
Figure 75 - HR Merlin test conditions: Project dimensions (left); wave spectra conditions (right).	73
Figure 76 - Paddle time series (HR Merlin).	73
Figure 77 - Hm0 variation line chart.	75
Figure 78 - Tp variation line chart.	76
Figure 79 - Um variation line chart.	76
Figure 80 - Scour variation in fine sand tests.	78
Figure 81 - Scour variation in layered sand tests.	78
Figure 82 - Monopile Scour depths.	79
Figure 83 - GBF scour depths.	80
Figure 84 - Residue deposition in "WEC 6" (left); and "WEC 4" (right).	80
Figure 85 - WEC scour (sine sand vs layered sand).	82
Figure 86 - "Waves 1" Monopile scour patterns (scour grading scale in meters).	83
Figure 87 - "Waves 2" GBF scour patterns (scour grading scale in meters).	84
Figure 88 - "WEC 6" GBF Scour patterns (scour grading scale in meters).	84
Figure 89 - Coarser sand layer limits (GBF).	85
Figure 90 - Coarser sand layer limits (Monopile).	85
Figure 91 - "WEC3" Monopile scour pattern symmetry (scour grading scale in meters).	86
Figure 92 - Differences in shape of the scour hole "Waves1" (top); and "Waves2" (bottom).	86
Figure 93 - Increased sediment deposition "Waves1" (top); and "WEC1" (bottom).	87
Figure 94 - Layered sand scour hole "Waves2" (Left); and "WEC4" (Right).	88
Figure 95 - "Waves 1" Monopile Scour patters; Scour grading scale in meters.	95

Figure 96 - "Waves 1" GBF scour patterns; Scour grading scale in meters.	95
Figure 97 - "WEC1" Monopile scour patterns; Scour grading scale in meters.	96
Figure 98 - "WEC1" GBF scour patterns; Scour grading scale in meters.	96
Figure 99 - "WEC2" Monopile scour patterns; Scour grading scale in meters.	97
Figure 100 - "WEC2" GBF scour patterns; Scour grading scale in meters.	97
Figure 101 - "WEC3" Monopile scour patterns; Scour grading scale in meters.	98
Figure 102 – "WEC3" GBF Scour patterns; Scour grading scale in meters.	98
Figure 103 - "Waves 2" Monopile scour patterns; scour grading scale in meters.	99
Figure 104 - "Waves 2" GBF scour patterns; Scour grading scale in meters.	99
Figure 105 - "WEC4" Monopile scour patterns; Scour grading scale in meters.	100
Figure 106 - "WEC4" GBF scour patterns; Scour grading scale in meters.	100
Figure 107 - "WEC5" Monopile scour patterns; Scour grading scale in meters.	101
Figure 108 - "WEC5" GBF scour patterns; Scour grading scale in meters.	101
Figure 109 - "WEC6" Monopile scour patterns; Scour grading scale in meters.	102
Figure 110 - "WEC6" GBF scour patterns; Scour grading scale in meters.	102

Table Index

Table 1- Typical shear stress amplification factor, from (Whitehouse, 1998).....	15
Table 2 - Breaking point estimations.	22
Table 3 - Review on existing Scour tests results.	31
Table 4 - Summary of results from (Tavouktsoglou, 2018).	33
Table 5 - Some of the most important scale factors.	35
Table 6 - List of main wavemaker components (Adapted from (Chambel, 2019)).....	39
Table 7 - Sediment analysis of SP 55 fine sand (Adapted from (Silva, 2010)).....	45
Table 8 - Sediment analysis of the coarse sand performed by LEMC.	46
Table 9 – Target prototype conditions.....	47
Table 10 - Target model conditions.....	47
Table 11 - Target prototype flow conditions	47
Table 12 - Average velocity values collected from VectrinoPlus in cm/s.....	51
Table 13 - Average velocity collected from VectrinoPlus in cm/s (4th Profile).	53
Table 14 - Target frequency ranges.....	56
Table 15 - Initial wave tests features.....	59
Table 16 - Reflection coefficients of test 4 ($T_p, \text{model} = 1.7 \text{ s}$).	59
Table 17 - 2° target frequency range.....	60
Table 18 - Wave tests for $T_p, \text{model} = 1.41 \text{ s}$	60
Table 19 - Reflection coefficient values for test 9 ($T_p, \text{model} = 1.41 \text{ s}$).	61
Table 20 - New target conditions.....	61
Table 21 - Full test plan.	64
Table 22 - Wave data collected.....	74
Table 23 - H_{m0} collected (WEC5).....	75
Table 24 - Orbital wave speed.	77

Table 25 - Table of scour results near the foundations.....	77
Table 26 - WEC scour depth table.	81
Table 27 - Deposition results.....	82

Nomenclature and Abbreviations

A [-] – Constant

a [m] – Wave amplitude

B [-] – Constant

C [-] – Constant

Ch [\sqrt{m}/s] – Chézy coefficient

D [m] – Diameter

D_* [-] – Dimensionless grain size

D_c [m] – Characteristic diameter

D_p [m] – Pile diameter

d [m] – Water depth

d_s [m] – Diameter of the sediment grain

d_{50} [m] – Mean diameter of bed sediments

d_x [m] – Sediment size for which x% is finer by weight

dep_{max} [m] – Maximum deposition height

e [-] – Neper's number

\bar{F}_e [N] – Elastic compression force

\bar{F}_g [N] – Gravitational force

\bar{F}_i [N] – Inertia force

\bar{F}_{il} [N] – Local inertia force

\bar{F}_n [N] – External force

\bar{F}_p [N] – Pressure force

\bar{F}_μ [N] – Friction force

\bar{F}_σ [N] – Surface tension force

Fr [-] – Froude number

f_1 [-] – Wave coefficient

f_2 [-] – Combined waves and currents effect

f_3 [–] – Sediment mobility coefficient

f_4 [–] – Structural height effect

f_5 [–] – Shape factor, ($=K_s$)

f_6 [–] – Flow depth effect

f_c [–] – Friction factor

f_i [s^{-1}] – Wave frequency

f_p [s^{-1}] – Peak frequency

f_w [–] – Wave friction factor

g [m/s^2] – Gravitational acceleration

H [m] – Wave height

$\bar{H}_{1\setminus 3}$ [m] – Average of the highest 1/3 of all waves

$\bar{H}_{1\setminus 10}$ [m] – Average of the highest 1/10 of all waves

$\bar{H}_{1\setminus 100}$ [m] – Average of the highest 1/100 of all waves

H_b [m] – Breaking wave height

H_d [m] – Design wave height

H_i [m] – Individual wave height

H_m [m] – Mean wave height

H_{m0} [m] – Spectral wave height from the 0^{th} order moment of a wave train with N waves

H_{max} [m] – Maximum wave height

H_r [m] – Ripple height

H_{rms} [m] – Root mean square wave height

H_s [m] – Significant wave height

h_c [m] – GBF height

KC [–] – Keulegan-Carpenter number

K_α [–] – Pier alignment factor

K_σ [–] – Grain size distribution factor

K_d [–] – Flow depth factor

K_s [-] – Shape factor

K_{si} [-] – Pier size factor

k [-] – Wave number, $2\pi/L$

k [-] – Von Karman constant

k_s [m] – Bed roughness

L [m] – Wave length

$L(f)$ [m] – Wave length as function of frequency

m_n [-] – n^{th} order moment

m_1 [-] – n^{th} order moment

N [-] – Number of waves

N [-] – Constant

Re [-] – Reynolds number

Re^* [-] – Sediment grain Reynolds number

$P(H \geq H_d)$ [-] – Exceeding probability

S [m] – Scour depth

S_e [m] – Equilibrium scour depth

S_{wec} [m] – Scour depth near the WEC device

$S(f)$ [m^2/s] – Energy spectral density

$Su(f)$ [m^2/s] – Power spectrum of the bottom velocity

s [m] – Specific density, ρ_s/ρ_w

T [s] – Wave period

$T(f)$ [s] – Wave period as function of frequency

T_0 [s] – Total duration of the wave train

T_i [s] – Individual wave period

T_p [s] – Wave peak period

$T_{m-1,0}$ [s] – Energy wave period

$T_{mi,j}$ [s] – Wave period from the i^{th} order moment and the j^{th} order moment

T_z [s] – Mean zero-crossing period

t [s] – time

t_e [s] – Equilibrium scour depth time scale

U [m/s] – Velocity

U_c [m/s] – Depth average flow velocity

U_{cr} [m/s] – Critical velocity

U_{cw} [m/s] – Velocity ratio

U_w [m/s] – Bottom wave orbital velocity

U_m [m/s] – Wave orbital velocity

Ur [–] – Ursell number

u [m/s] – Horizontal velocity

u_* [m/s] – Friction velocity

W [m] – Total scour extent

W [m] – Width

w [rad/s] – Angular frequency

x [m] – Horizontal position

z [m] – Vertical distance

Z_0 [m] – Bed roughness length

α [–] – Amplification factor

α_c – Additional turbulence constant

α_{down} [°] – Downstream scour slope

α_{up} [°] – Upstream scour slope

Υ [–] – Enhancement peak factor

δ [–] – Bottom boundary layer

Δf [–] – Frequency band

θ [–] – Shields parameter

θ_{cr} [–] – Critical shields parameter

λ [-] – Scale factor

μ [$N \cdot s/m^2$] – Dynamic viscosity

ρ_s [Kg/m^3] – Sediment mass density

ρ_w [Kg/m^3] – Water mass density

σ_s [-] – Standard deviation of the scour depth

σ_u [-] – Orbital velocity spectrum

τ [N/m^2] – Amplified bed shear stress

τ_∞ [N/m^2] – Undisturbed bed shear stress

τ_b [N/m^2] – Bed shear stress

$\tau_{b,c}$ [N/m^2] – Current induced bed shear stress

$\tau_{b,w}$ [N/m^2] – Wave induced bed shear stress

τ_{cr} [N/m^2] – Critical bed shear stress

τ_m [N/m^2] – Mean combined shear stress

τ_{max} [N/m^2] – Maximum combined bed shear stress

ν [m^2/s] – Kinematic viscosity

ϕ [$^\circ$] – Angle between the current direction and wave direction

ϕ_i [$^\circ$] – Internal friction angle of the sediment

η [m] – Surface water elevation

ADV – Acoustic Doppler Velocimetry

CPT – Cone Penetration Test

DTM – Digital Terrain Model

DAQ – Data Acquisition System

FEUP – Faculty of Engineering of the University of Porto

GBF – Gravity based foundations

HR – Hydraulic Research

ITTC – International Organization Tank Congress

JONSWAP – Joint North Sea Wave Project

LCoE – Levelized Cost of Energy

LEMC – Construction Materials Testing Laboratory

MDCP – Motor Drive Control Panel

MRE – Marine Renewable Energy

PLA – Polylactic acid

PM – Pierson- Moskowitz

SHRHA – Water Resources and Environment Division

SNR – Signal-to-Noise Ratio

SWL – Still Water Level

UK – United Kingdom

WEC – Wave Energy Converter

INTRODUCTION

1.1. European wind sector

Europe is a global leader in wind energy and, over recent years wind energy has rapidly developed into becoming one of the primary sources of renewable energy (Esteban et al., 2019; Wu et al., 2020). According to the annual report made by (WindEurope, 2022b), wind energy covered 15% of Europe's electricity demand in 2021 with over 235 GWh installed capacity, of which 207 GWh in onshore windfarms and 28 GWh in offshore windfarms.

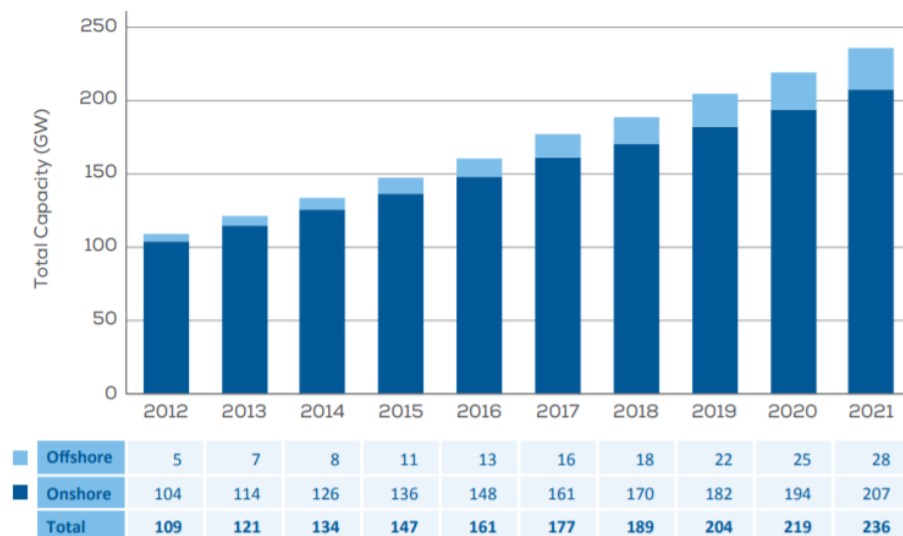


Figure 1 - Total wind energy capacity growth in Europe (WindEurope, 2022b).

Since 1991, with the construction of the first offshore windfarm “Vindeby” in Denmark an increasing trend of new offshore windfarms investments emerged (Colmenar-Santos et al., 2016; Fazeres-Ferradosa, 2018). In 2021 a total of 17.4 GWh of new wind installations were made in Europe, of which only 3.3GWh were allocated in offshore windfarms, corresponding to 19% of the total new installation (WindEurope, 2022b). In the next 5 years (2022-2026), 17.6 GWh per year are expected to be built in Europe, of which offshore windfarms will represent 24% of the total number of new investments, a number well short from the 32 GWh needed to reach the 40% renewable energy target.

Furthermore, the increasing tension in the Europe geo-political climate and uncertainty of future Europe energy supply will urge Europe's efforts to reduce fossil fuel consumption and promote the deployment of renewable energy aiming for Europe energy security and the fight against climate change (WindEurope, 2022a).

The North Sea will be the main stage of the expansion of the Europe offshore power grid, and recently in the joint Esbjerg Declaration the four Heads of State (Germany, Belgium, Denmark, and Netherlands) committed to jointly build 150 GWh of offshore wind energy in the North Sea alone by 2050 as part of the REPowerEU Action Plan, which is a strategic plan to wean Europe off Russian fossil fuel (WindEurope, 2022a).

1.2. Offshore wind optimization

Naturally, with the eminent growth of the offshore wind industry the path toward optimization has accelerated. The main metric used to quantify the level of optimization is the LCoE, the Levelized Cost of Energy. The LCoE is the average lifetime cost per unit of energy, which incorporates all the costs incurred during the life of a power plant, including the total cost of building, operating and maintenance, fuel, among others, and divides the sum of those costs by the lifetime output of the power plant (EY, 2015). In 2017 this value was about 120 to 150 €/MWh, however the goal is to reach the range of 60 to 90 €/MWh in 2030 (EY, 2015; Fazerer-Ferradosa, 2018).

Foundation design is a crucial step towards optimization of offshore wind turbines, as it represents roughly 25% to 34% of the overall cost (Bhattacharya, 2014). It was reported that the development of the Atlantic Array wind farm did not materialize partly due to a high foundation related cost. The vast majority of offshore wind turbines have monopile foundations, however only in recent years gravity based structures have been considered viable support structures to offshore wind turbines due to their size (Tavouktsoglou, 2018).

A crucial step towards reducing the cost of foundations is understanding the soil fluid structure dynamics, which leads to scour processes. Scour is one of the main risks of failure parameters in foundation design in offshore foundations and can be defined as the seabed sediments erosion around the foundation.

1.3. Main objectives

The current dissertation focusses on the study of scour phenomena around offshore foundations such as the monopile and gravity-based foundations. The scour phenomenon is one of the most researched fields in hydraulic engineering, however the vast majority of the existing literature focusses in the scour in monopile foundations. Studies dealing with complex geometries such as the gravity-based foundations are still very scarce. Furthermore, existing literature only verses for one type of sediment in the soil composition.

The current dissertation will include an experimental physical model study conducted at the Hydraulics Laboratory of the Faculty of Engineering of the University of Porto (FEUP). This study expands from former studies made about the same topic by extending the experimental tests for different non-cohesive soils compositions, such as layered soils. The main objective is to create a dataset of scour tests for two of the most common foundation geometries used in marine energy, the monopile and gravity-based foundation. It is expected that the current research will contribute toward the development of new methods of scour prediction, aiming towards optimization.

Furthermore, hybridization of marine renewable technologies, which consist of the deployment of different marine energy converters near existing offshore structures, are currently being investigated.

This type of solution would be one possible optimization strategy by reducing the overall logistics and maintenance costs. For that reason, the current dissertation includes an innovative experimental study regarding the scour effects of the deployment of wave energy converters, such as the oscillating wave surge converter, near the offshore wind turbines foundations.

1.4. Dissertation outline

The present dissertation is divided into 5 chapters and in this subchapter, there is a brief description of the works performed in each chapter.

Chapter 1 intends to contextualize the leading motivations and interest in this research developed and give a summary of the current state and the future of the offshore wind energy sector and provide the main objectives of this dissertation

Chapter 2 provides the basic principles concerning the scour phenomena around offshore foundations including the main design parameters of scour prediction. Also presents basic notions of innovative wave energy converters devices. Moreover, this chapter summarizes some findings from previous studies about this topic and compiles some of their main experimental results.

Chapter 3 is reserved for a description of the experimental setup of the Hydraulic Laboratory at FEUP, including the description of the two foundation models, the WEC model, and the sediment characteristics used to replicate the seabed soil. Also, the presentation of the sea state conditions used in the series of tests. Furthermore, in this chapter can be found some considerations about the scale and model effects that may occur in the experimental phase.

Chapter 4 is focused on the experimental study, with descriptions of the calibration process and presentation of all measuring equipment used. This chapter reports all the laboratory work and the corresponding experimental results. Finally, this chapter provides an in-depth analysis of the results, and further comparison with results from previous studies.

Chapter 5 summarizes and provides all the conclusions obtained from the present dissertation. Besides the conclusions there is a brief discussion of the future work perspectives.

2

SCOUR PHENOMENA IN MARINE ENVIRONMENT

2.1. Types of fixed bottom foundations for offshore wind farms

The present dissertation focuses on the scour phenomenon, which is a common concern in the design of offshore foundations. The cost of the foundation of offshore wind farms increase significantly from shallow waters (water depth of 0 m to 30 m) to deep waters (50 m – 200 m) (Mengé, 2008). The foundation selection and design is an important step in order to achieve sustainability of the project (Lavanya & Kumar, 2020).

In shallow waters, the most commonly used foundations are the monopile foundations, and the gravity-based foundations (GBF). Usually the monopile foundation is most commonly used rather than the gravity type foundation, because the GBF is expensive to construct in water depths beyond 10 m (Lavanya & Kumar, 2020). Multipod type foundations, such as the tripod and jacket foundations, are usually preferred in water depths higher than 30 m.

The stability of the gravity-based foundations derives from the self-weight of the body of the foundation. Consists of a circular pile connected to a larger heavier base (figure 2).

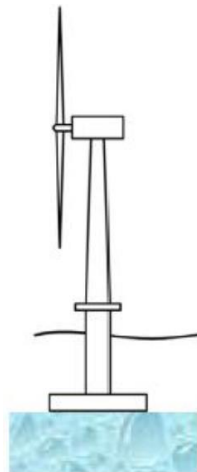


Figure 2 - Gravity based foundation (Lavanya & Kumar, 2020)

The monopile foundation is the most economical solution water depth less than 30 m and for seabed of sand and gravel type (Oh et al., 2013). The monopile foundation consists of a singular circular pile engraved in the seabed (Figure 3).

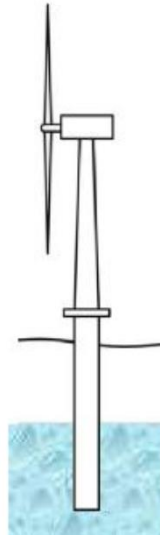


Figure 3 - Monopile foundation (Lavanya & Kumar, 2020).

Multipod foundations, such as the tripod and jacket structures, are effective in transitional waters (water depth of 30 m to 50 m)(Center for Wind Energy, 2012). In the tripod foundation, the wind turbine rest in a steel frame that distributes the loads onto three steel piles. The jacket foundation consists of a multi-chord base formed of multiple section of structural pipes welded together (Figure 4).

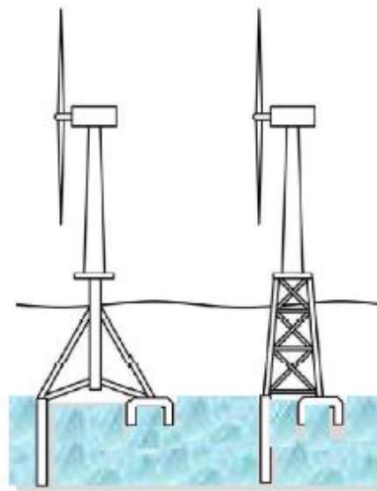


Figure 4 - Multipod Foundation (Tripod and Jacket) (Lavanya & Kumar, 2020).

2.2. North Sea complex soil

The soil composition of the North Sea is complex. Sand are present in almost all area of the North Sea seabed, as a thin layer, interbedded with clays and as the predominant soil type (Bond et al., 1997). The North Sea is divided into four main provinces, as characterized by Thomas (1989), based on the following generalized soil profiles:

- Stiff to very stiff over consolidated clays and silty clays (Thin surface unit of fine sand);
- Very soft to soft normally consolidated clays and silty clays overlying stiff to very stiff over consolidated silty clays (Thin surface unit of fine sand);

- Stiff to very stiff over consolidated silty clays and clays interbedded with dense fine sand (Thin surface unit of fine sand); and
- Fine to coarse sand with scattered seams and beds to soft and stiff clays and silty clays.

The North Sea soil conditions differ greatly from the UK sector in the north to the south and central parts of the North Sea. In the north, stiff to very stiff over consolidated clays are in abundance, although interbedded with dense fine sand in some areas. Interbedded clays and sands are predominant in the central North Sea, whereas in the south are mainly fine and coarse sands. (Bond et al., 1997).

In Figure 5 it can be seen a schematic overview of a typical stratigraphy found in the southern areas of the North Sea. This schematization is an adaptation from the results of *in situ* cone penetration tests (CPT) from Coughlan et al. (2018).

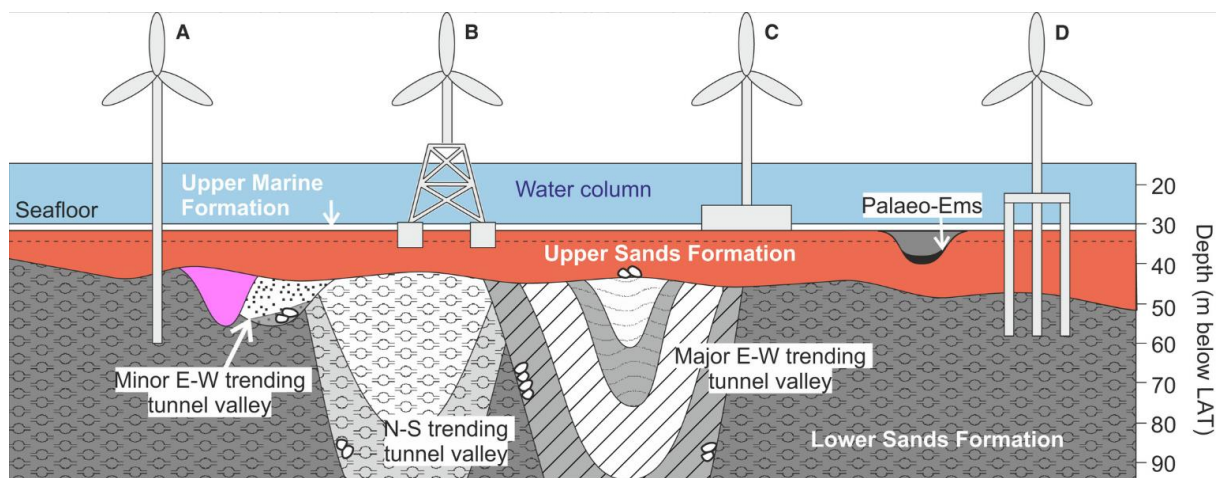


Figure 5 - Schematic overview of a typical stratigraphy of the southern parts of the North Sea ((Fleischer et al., 2022) adapter from Coughlan et al. (2018))

2.3. Soil-fluid-structure interaction

To understand the fundamentals of the scour phenomena that occurs around the fixed-bottom foundations of offshore structures, it is important to understand the basic changes of flow patterns induced by the construction of these structures.

Since the most common type of foundation used in marine environment follow the monopile configuration, the influence in flow patterns induced by monopile foundations has been extensively studied for wave field (Nielsen et al., 2013) and steady current field (Roulund et al., 2005; Soulsby, 1997). Nevertheless, there is a significant shortcoming in studies of flow patterns around complex geometry foundations, and for combined waves and currents.

The figure 6 presents a simplified visual configuration of the most important changes in flow pattern identified by (Sumer & Fredsøe, 2002).

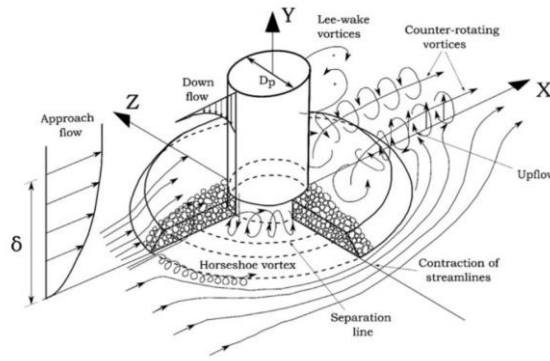


Figure 6-Configuration of flow patterns around monopile foundations (Petersen et al., 2015).

When the flow reaches the obstruction caused by the monopile, both velocity and stagnation pressure decrease downwards from the surface, forming a down pressure gradient (Fazeres-Ferradosa, 2018). This downflow when meeting the seabed and rolling up forms a horseshoe vortex (De Vos, 2008; Petersen et al., 2015), that increases the bed shear stress (phenomena explored in subchapter 2.2). Furthermore, the horseshoe after its formation moves downstream on both sides of the monopile moving the pulled particles due to the increased bed shear stress downstream. The horseshoe vortex is the main scour mechanism around the base of the pile (Petersen et al., 2015; Whitehouse, 1998), which leads to scour patterns as shown in Figure 6.

The separation and bending of the flow upstream of the pile leads to the contraction of streamlines and increase in velocity on both edges of the structure (Fazeres-Ferradosa, 2018). This mechanism of increased flow velocity and bed shear stress explains this increase in scour around the edges of the pile.

Furthermore, the separation of flow by the monopile creates an almost vertical suction force in the downstream face of the pile, due to the roll down of the boundary conditions on both sides of the pile, which generates an increased turbulent state in the form of lee-wake vortices, also considered an important mechanism of scour (Fazeres-Ferradosa, 2018; Sumer & Fredsøe, 2002). The lee-wake vortices increase the bed shear stress downstream of the pile, which results in a significant increase in sediment transport. The lifted particles are then dragged downstream until the deposition occurs

The lifted particles tend to move downflow until their deposition when the amplified bed shear stress caused by the changes in flow patterns is no longer enough for sediment transport, thus, forming a mound further downstream of the pile, the zone of deposition (Figure 7).

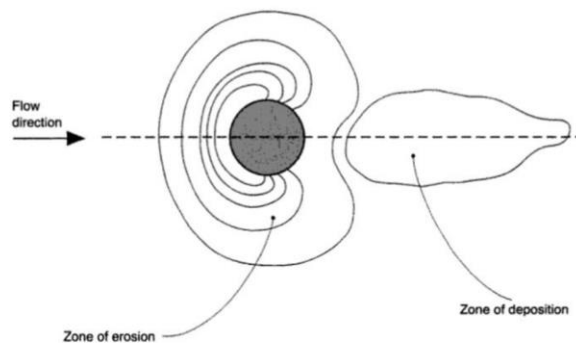


Figure 7- Scour pattern around the base of the monopile foundation (Whitehouse, 1998).

2.4. Bed shear stress

The bed shear stress in the marine environment is the friction generated between a moving body of fluid and the surface of soil. That ultimately is the force responsible for the sediment motion. The movement of water creates friction in the seabed. The common hydrodynamic agents responsible for the movement of water are currents and waves (Soulsby, 1997). The bed shear stress controls how much sediment of the bed layer is in suspension, so it is amply considered to be the physical parameter with largest influence on sediment transport.

The most common representation of bed shear stress comes in the form of tension, $\tau_b (N/m^2)$, units of force per unit of area and can be expressed according to Eq. (1).

$$\tau_b = \rho_w \cdot (u_*)^2 \quad (1)$$

It can also be represented in its dimensionless form presented by the Shields parameter θ (explained in more detail in subchapter 2.3), which is the ratio between the load on the particle and the gravitational force that resist the movement (Shields, 1936), by Eq. (2). In Eq. (2) $g = 9.81 \text{ m/s}^2$, is the gravitational acceleration, $(s - 1)$ is the ratio of densities of sediment and water, and d_s denotes the sediment grain diameter as described in Loosveldt and Vannieuwenhuysse (2012).

$$\theta = \frac{\tau_b}{g(\rho_s - \rho_w)d_s} = \frac{(u_*)^2}{g(s - 1)d_s} \quad (2)$$

To better understand the effects induced by currents and waves, it is important to consider the concept of bed boundary layer (δ) represented in figure 8. As described in Fazeres-Ferradosa (2018) and references therein, the bed boundary layer can be defined as the layer in which the sand-bed is influenced by the flow (De Vos, 2008). This layer is often referred to as the layer located between the boundary surface and the point where the local velocity is equal to 0.995 times the depth-average flow (U_c).

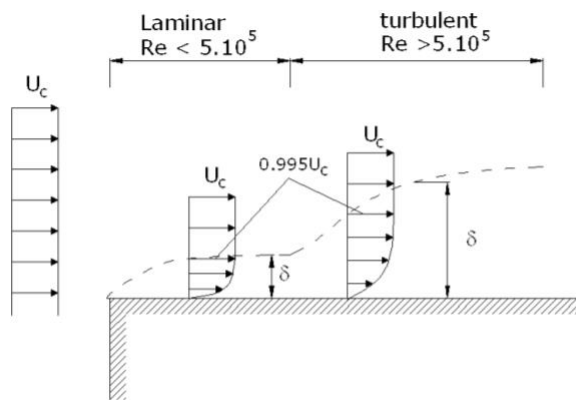


Figure 8- Boundary layer (Liu, 1998).

2.4.1. Current induced

The bed shear stress related with the current interaction, $\tau_{b,c}(N/m^2)$ depends on flow velocity $U_c(m/s)$ and bed roughness, represented by the friction factor f_c , as expressed in Eq. (3)

$$\tau_{b,c} = \frac{1}{2} \cdot \rho_w \cdot f_c \cdot U_c^2 \quad (3)$$

The friction factor f_c , is a dimensionless coefficient determined by the water depth d , and the bed roughness k_s in case of hydraulic rough flow or friction velocity u_* in case of hydraulic smooth flow. The friction factor can be assessed using Eq. (4) from Liu (1998).

$$f_c = \frac{2g}{C^2} = \frac{2g}{\left(\frac{\sqrt{g}}{k} \ln\left(\frac{d}{z_0 \cdot e}\right)\right)^2} = \begin{cases} \frac{0.06}{\left(\log\left(\frac{12d}{3.3 \cdot \frac{\nu}{u_*}}\right)\right)^2}, \text{For smooth flow: } \frac{u_* k_s}{\nu} \leq 5 \\ \frac{0.06}{\left(\log\left(\frac{12d}{k_s}\right)\right)^2}, \text{For rough flow: } \frac{u_* k_s}{\nu} \leq 70 \end{cases} \quad (4)$$

The symbol C is the Chézy coefficient (\sqrt{m}/S), k is the von Karman constant and equals to 0.04, ν stands for the kinematic viscosity of water, z_0 denotes the roughness length (in meters), and e is the Neper's number equal to 2.718.

As presented in (Liu, 1998), while in smooth flow, the bed roughness is so small that it does not affect the velocity distribution, since the roughness elements stay within the viscous sublayer. In rough flow, there is no viscous sublayer, so in this case the flow velocity does not depend on viscosity. There is also an intermediate transitional stage in which the velocity distribution relies on both the bed roughness and viscosity. The bottom roughness value is dependent on the presence of ripples, and as presented in De Vos (2008):

- In the absence of rippled ($k_s = 2.5d_{50}$);
- In the presence of ripples ($k_s = (0.5 - 1)H_r$);

with d_{50} , the median grain sediment and H_r , the ripple height.

The roughness length, Z_0 has different configurations according to the flow type. It can be assessed using Eq. (5) as presented in Chambel (2019).

$$Z_0 = \frac{k_s}{30} + \frac{\nu}{9u_*} = \begin{cases} \frac{\nu}{9u_*}, \text{For smooth flow: } \frac{u_* k_s}{\nu} \leq 5 \\ \frac{k_s}{30}, \text{For rough flow: } \frac{u_* k_s}{\nu} \leq 70 \end{cases} \quad (5)$$

In a steady current, the velocity distribution in a steady, uniform, turbulent boundary layers was found to be very accurately approximated by the logarithmic profile (De Vos, 2008). For a specific water depth

z , the mean current velocity $U(z)$, is a function of the friction velocity u_* , von Karman constant k , and roughness length Z_0 (as given in Eq(6)).

$$U(z) = \frac{u_*}{k} \ln \left(\frac{d}{z_0} \right) \quad (6)$$

Furthermore, the approximation of $U_c = 0.4d$ can be used in experimental works, since as presented in De Vos (2008) the combination of equations (5) and (6), leads to the conclusion that the average flow velocity, U_c , can be measured at approximately 40% of the water depth ($0.368d \approx 0.4d$), counting from the sand bed.

2.4.2. Wave induced

The bed shear stress caused only by waves ($\tau_{b,w}(N/m^2)$) is oscillatory and is obtained according to Eq. (7), in which f_w is the wave friction and U_m is the orbital velocity as described in Eq. (8).

$$\tau_{b,w} = \frac{1}{2} \cdot \rho_w \cdot f_w \cdot U_m^2 \quad (7)$$

In shallow conditions ($d/L < 0.5$), the waves generate an oscillatory horizontal velocity at the seabed with an amplitude of U_m . In the case of linear waves the U_m can be derived with linear wave theory as in Eq. (8) (De Vos, 2008), where H is the wave height, L the wave length and T the wave period:

$$U_m = \frac{\pi H}{T_w} \cdot \frac{1}{\sinh \left(\frac{2\pi d}{L} \right)} \quad (8)$$

Regarding the friction factor, there has been a number of formulas proposed by (Nielsen, 1992), (Fredsoe & Deigaard, 1992), (Soulsby, 1997) and (Dixen et al., 2008) as summarized in (Nielsen & Guard, 2010). Figure 9 provides the results of a study at a geometric scale 1/50 developed by (De Vos et al., 2011), highlighting the influence of the wave friction factor on the final bed shear stress induced by waves.

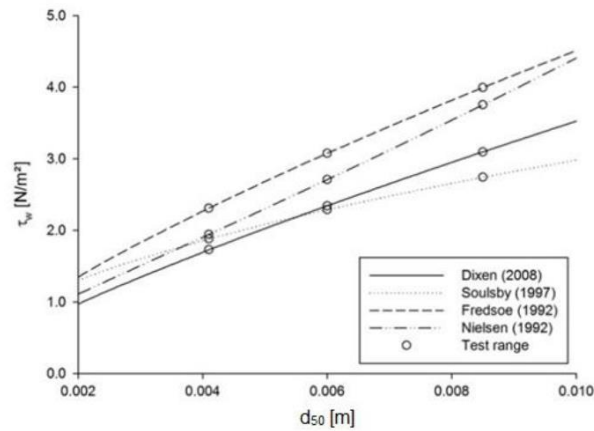


Figure 9-Wave induced bed shear stress related to grain size , according to different authors (De Vos et al., 2011).

However, for continuity reasons and following previous works of Fazeres-Ferradosa 2018 and Chambel 2019, the friction factor f_w formula used in this dissertation is described in (Soulsby, 1997), that can be presented in Eq. (9), depends on the mean diameter of the sea-bed d_{50} and uses the bed roughness length z_0 (Eq. (10)), instead of the bottom roughness k_s .

$$f_w = 1.39 \cdot \left(\frac{A}{z_0}\right)^{-0.52} \tag{9}$$

$$z_0 = \frac{d_{50}}{12} \tag{10}$$

2.4.3. Combined wave and current induced

In order to replicate as accurately as possible, the marine environment, it is important to understand how the bed shear stress develops in combination of both waves and currents. The combination effect does not follow the linear combination of the separate effect ($\tau_{b,c} + \tau_{b,w}$), according to multiple works of the literature (Soulsby, 1997) (De Vos et al., 2011), (Saruwatari et al., 2014).

In the present thesis, the theory used to describe the interaction of waves and currents in the bed shear stress represented in figure 10 is presented in (Soulsby, 1997) and only considers the effect of waves and currents acting in the same direction.

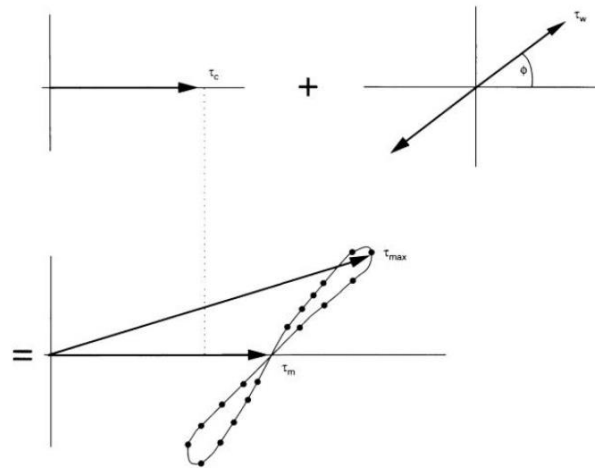


Figure 10- Non-linearity of bed shear stress in combined wave and current interaction (Soulsby, 1997).

The combined mean shear stress $\tau_m(N/m^2)$, and the maximum combined bed shear stress, $\tau_{max}(N/m^2)$ can be estimated using the following Eqs. (11) and (12). Where $\phi(^{\circ})$ is the angle between the current direction and wave direction.

$$\tau_m = \tau_{b,c} \cdot \left[1 + 1.2 \left(\frac{\tau_{b,w}}{\tau_{b,c} + \tau_{b,w}} \right)^{3.2} \right] \quad (11)$$

$$\tau_{max} = \left[(\tau_m + \tau_{b,w} \cos\phi)^2 + (\tau_{b,w} \sin\phi)^2 \right]^{1/2} \quad (12)$$

2.5. Threshold of motion

The threshold of motion is reached when the lifting and dragging forces created by the flow surpasses the gravitational force that is stabilizing the particle, thus leading to its motion. According to Shields (1936), the threshold of motion can be represented by the moment when the bed shear θ stress in its dimensionless form, exceeds the critical bed shear stress θ_{cr} , as indicated by Eq. (13).

$$\theta = \frac{\tau_b}{g(\rho_s - \rho_w)d_s} > \theta_{cr} = \frac{\tau_{cr}}{g(\rho_s - \rho_w)d_s} \quad (13)$$

First introduced by Shields (1936), the shields parameter θ is a dimensionless representation of shear stress expressed as in Eq. (2). Shields also proposed the notion of shields curve (Figure 11), which establishes the relation between the Shields parameter and the Reynolds number of the particle (Re^*), given in Eq. (14). The shields curve can predict with significant accuracy the moment when a certain dimension of sediment starts to move with a particular shear stress. For large dimensions, the curve tends to 0.056. Therefore, a good number for the design of scour protection is 0.035, as suggested by De Vos et al. (2011).

$$Re^* = \left(\frac{g(s - 1)}{v^2} \right)^{1/3} \quad (14)$$

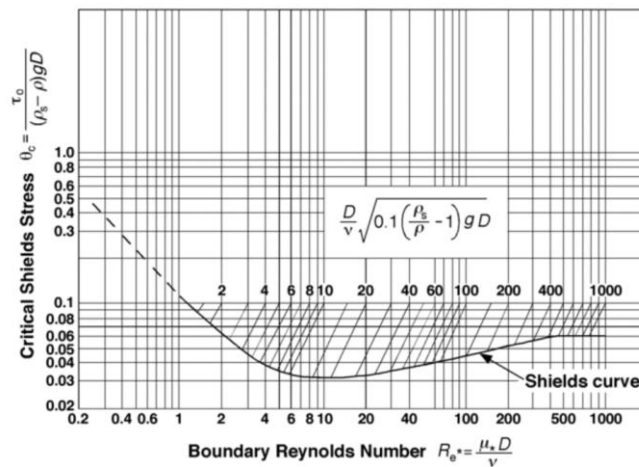


Figure 11- Shields diagram (adapted from (Shields, 1936)).

A major disadvantage of this representation is the implicit relationship between the two variables of the shield curve. A solution was proposed by (Soulsby, 1997), where the critical shear stress is represented in Eq. (15), where D_* , the dimensionless grain size in Eq. (16).

$$\theta_{cr} = \frac{0.3}{1 + 1.2D_*} + 0.055[1 - \exp(-0.020D_*)] \quad (15)$$

$$D_* = \left(\frac{g(s-1)}{v^2} \right)^{1/3} d_s \quad (16)$$

The Soulsby diagram plotted in the Shields diagram delivers a convenient approximation for the threshold of motion for sediments exposed to waves and/or currents (Figure 12)

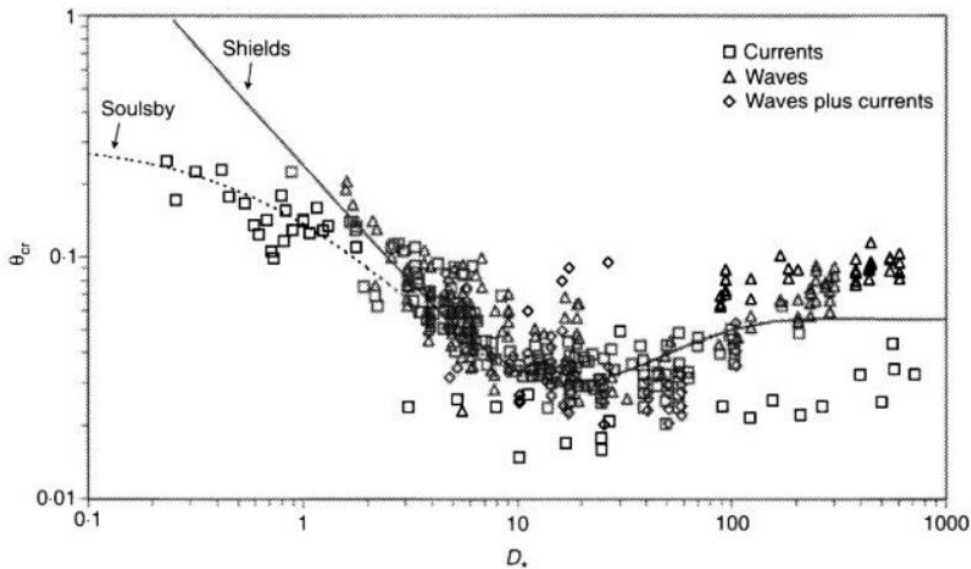


Figure 12- Shields diagram adapted by Soulsby (Soulsby, 1997).

2.6. Amplified bed shear stress

As discussed in the sub-chapter 2.1, the changes in flow pattern created by the construction of fixed bottom foundations induce an amplification of the bed shear stress that can be expressed by α , the amplification factor (Eq. (17)).

$$\alpha = \frac{\tau}{\tau_{\infty}} \quad (17)$$

The amplification factor is the ratio between the amplified shear stress τ , and the undisturbed shear stress τ_{∞} . This factor has been extensively studied for the monopile configurations, where in some areas

of the horseshoe vortex can have values of around eleven. More in depth studies can be found in Whitehouse (1998).

For more complex geometries, the amplification factor is best obtained in laboratory. Despite its scarcity, some studies have already been conducted. The Table 1 adapted from (Whitehouse, 1998) summarizes some of those studies.

Table 1- Typical shear stress amplification factor, from (Whitehouse, 1998)

Flow type/Structure type	α	Source
Steady flow Slender pile	4	Hjorth, (1975)
Pipeline	4	Fedsoe, (1993)
Squat pipe	2 to 5	Baker (1979); Eckman and Nowell, (1984)
Bridge caisson (Rectangular)	4 to 6	Hebsgaard et al. (1994)
Wave flow Circular Pile	2 to 3	Sumer et al, (1992b)
Wave-current flow Bridge caisson (rectangular)	4 to 6	Hebsgaard et al, (1994)

2.7. Clear water scour and live bed scour

The scour can occur in different flow regimes and depends on the balance between sediment transport and deposition (Melville & Chiew, 1999). Clear water scour conditions occurs when the bed shear stress is below the critical bed shear stress ($\theta < \theta_{cr}$). The clear water conditions scour is only induced by the increased velocity in the vicinity of the foundation due to the amplification factor, while the surrounding sea bed area remains at rest. The live-bed scour exists in critical bed-shear stress conditions ($\theta \geq \theta_{cr}$), there is a general sediment transport across the whole sea-bed (Harris et al., 2010).

Figure 13 highlights the difference in evolution of scour in clear water and live-bed scour conditions.

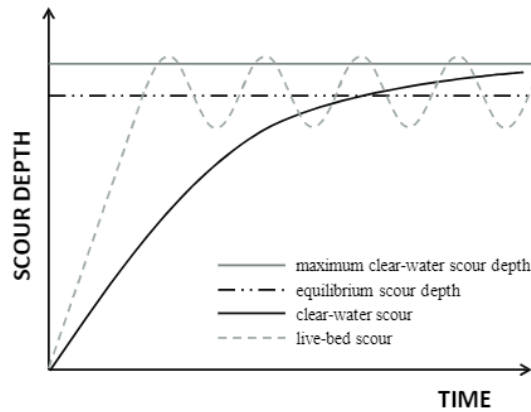


Figure 13 - Scour development in clear-water and live-bed scour conditions (Brandimarte et al., 2012).

2.8. Wave climate

As the current study is focused on the scour behaviour in the offshore marine environment, it is important to understand the wave climate and its characteristics.

2.8.1. Regular waves

A wave can be defined by its wave height H , wavelength L , and water depth d (Loosveldt & Vannieuwenhuysse, 2012). In the following figure 14 there is a visual simplification of these parameters, as well as the representation of the motion of the water particles in elliptical orbits. The wave crest is the highest point of the wave whereas the wave trough is the lowest wave point. The wavelength L corresponds to the distance between two consecutive wave crests, whilst wave height is the difference in elevation between wave crest and wave trough. The water depth d is the elevation of the sea water level (SWL) and the seabed.

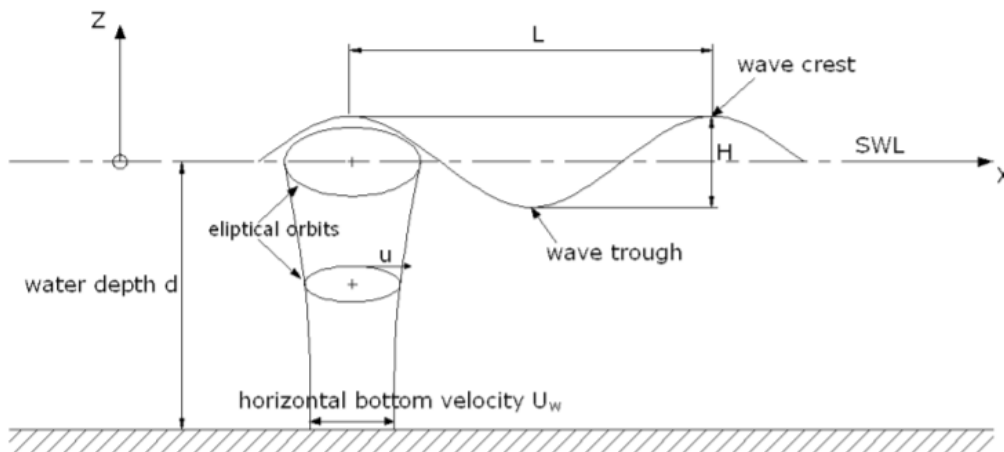


Figure 14 - Wave characteristics - regular linear wave (De Vos, 2008).

According to the most elemental wave theory developed in Airy (1845), the surface elevation at a given location can be approximated by the following cosine equation Eq. (18).

$$\eta(x, t) = \frac{H}{2} \cos(kx - \omega t - \phi) \quad (18)$$

In Eq. (18), x is the given horizontal position, k is the wave number ($2\pi/L$), w is the angular frequency ($2\pi/T$), and ϕ corresponds to the phase shift. The wavelength can be computed from its wave period T and water depth using the following relationship (Eq. (19):

$$L = \frac{gT^2}{2\pi} \tanh\left(\frac{2\pi d}{L}\right) \quad (19)$$

As described in Figure 14, from (De Vos, 2008), the water particles have vertical and horizontal component velocities, and when approaching the bottom, the vertical component tends to zero. For bed shear purposes, the horizontal component is relevant. Using the linear wave theory (Airy, 1845) the amplitude of the horizontal velocity u , can be determined by:

$$u = \frac{H}{2} \frac{gT}{L} \frac{\cosh\left(\frac{2\pi(z+d)}{L}\right)}{\cosh\left(\frac{2\pi d}{L}\right)} \quad (20)$$

In the seabed ($z=-d$) the orbital velocity (U_m) can be determined by Eq. (21).

$$U_m = \frac{H}{2} \frac{gT}{L} \frac{1}{\cosh\left(\frac{2\pi d}{L}\right)} = \frac{\pi H}{T} \frac{1}{\cosh\left(\frac{2\pi d}{L}\right)} \quad (21)$$

When the ration between wave amplitude and water depth starts to increase, i.e, the water depth decreases or the wave steepness increases, the former similarity of distance between SWL and wave crest and trough ceases to exist. Generally, the wave trough becomes deeper and wider (De Vos, 2008). Therefore, finite-amplitude wave theories such as stokes and fenton's fourier should be used (De Vos, 2008; Fazeres-Ferradosa, 2018). Further explanation of this theories can be found in Fenton (1999) and Us Army Corps of Engineers (2002).

2.8.2. Irregular waves

However, on the sea surface, waves are created differently, with different wave heights and periods. The irregularity of wave heights and periods creates irregular wave trains such as the wave train represented in Figure 15.

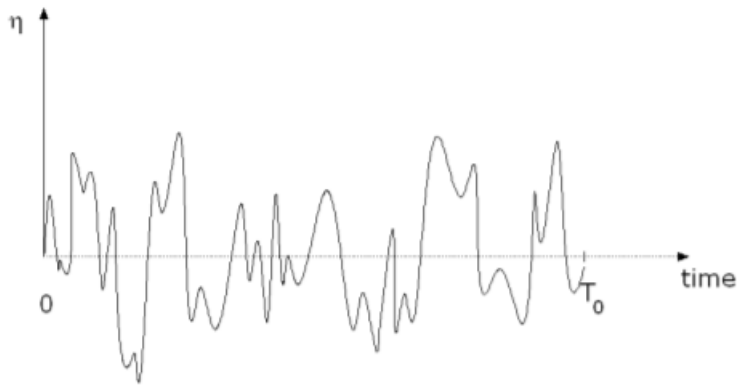


Figure 15 - Representation of a real irregular wave train (Loosveldt & Vannieuwenhuysse, 2012).

There are two ways to analyse the irregular wave trains, namely the wave-by-wave analysis and the spectral analysis (Chambel, 2019; De Vos, 2008; Fazeres-Ferradosa, 2018). The wave-by-wave analysis creates a criterium to separate the different individual waves. The figure 16 identifies an individual wave using the zero-down crossing method in which each wave is defined between two consecutive surface downward crossing of the zero line (Us Army Corps of Engineers, 2002).

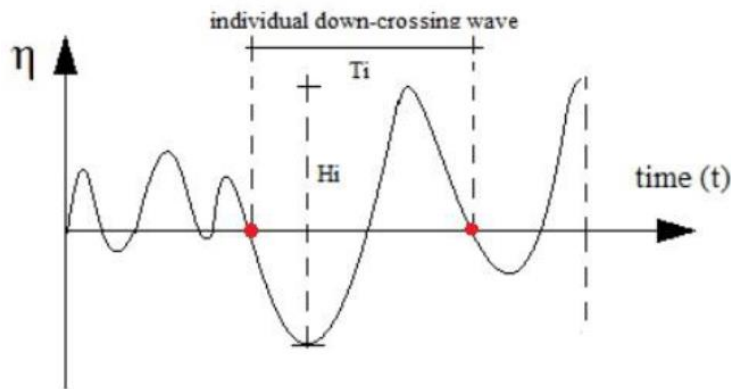


Figure 16 - Individual wave identified with zero-down crossing method (Chambel, 2019)

The zero-down crossing method analyse the mean wave heights (H_m) and mean zero-crossing period (T_z), and for design criteria is normally used the following values (Chambel, 2019), the significant wave height (H_s) is the average of the highest 1/3 of all waves ($\bar{H}_{1/3}$), the maximum wave height (H_{max}) is the largest wave height recorded, the wave height ($\bar{H}_{1/10}$), average of the highest 1/10 of all waves , the wave heigh ($\bar{H}_{1/100}$) the average of the 1/100 of all waves.

For a sufficient vast number of waves in a time series, there are different probability functions used to characterize the wave height. In the present study, it was adopted the Rayleigh distribution, as shown in Eq. (22), where H_{rms} , is the root mean square wave height.

$$P(H \geq H_d) = e^{\frac{-H_d}{H_{rms}}} \quad (22)$$

$$H_{rms} = \sqrt{\frac{1}{N} \sum_{i=1}^N H_i^2} \quad (23)$$

The Rayleigh distribution leads to several relations between H_{rms} , as shown in Eq. (24) to Eq. (28). and other wave characteristics. However, this distribution is only fairly accurate for short-term analysis. When studying the long term effects, it is usual to consider the Weibull distribution (Chambel, 2019; Fazeres-Ferradosa, 2018).

$$H_m = 0.886H_{rms} \quad (24)$$

$$H_s = 1.416H_{rms} \quad (25)$$

$$\bar{H}_{1\backslash 10} = 1.80H_{rms} \quad (26)$$

$$\bar{H}_{1\backslash 100} = 2.359H_{rms} \quad (27)$$

$$H_{max} = 2.63H_{rms} \quad (28)$$

For spectral analysis, an irregular sea state is defined as the superposition of several regular waves with different wave heights and wave periods. The spectral analysis expresses the water elevation in a frequency series instead of a time series (Fazeres-Ferradosa, 2018). By applying a Fourier transformation is possible to plot the wave energy or wave amplitude (a) for each wave frequency f_i (De Vos, 2008; Fazeres-Ferradosa, 2018). The energy spectral density $S(f)$, can be assessed using Eq. (29). In Eq. (29), Where the frequency band of the spectrum is $\Delta f = T_o^{-1}$, whilst T_o is the total duration of the wave train. Figure 17 illustrates the representation of the energy spectral density per each frequency.

$$S(f) = \frac{1}{2} \frac{a^2}{\Delta f} \quad (29)$$

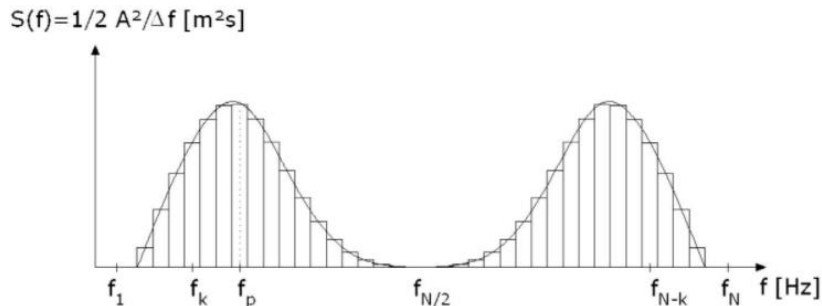


Figure 17 - Energy spectral density (De Vos, 2008).

The energy of the wave spectrum can be represented by the moment of spectrum density for a certain n moment, m_n , as expressed by Eq. (30).

$$m_n = \int_0^{+\infty} f^n S(f) df \quad (30)$$

The variable m_1 is the mean frequency of the spectrum and m_2 is the standard deviation of the equivalent gaussian spectrum in accordance with Vogel et al. (2001). Alongside m_1 and m_2 , the importance of m_0 is also notable because it is possible to obtain the following wave height characteristics (Eq. (31) to Eq. (34)).

$$H_{m_0} = 4.04\sqrt{m_0} \approx H_s \quad (31)$$

$$\bar{H}_{1\setminus 10} = 5.091\sqrt{m_0} \quad (32)$$

$$\bar{H}_{1\setminus 100} = 6.672\sqrt{m_0} \quad (33)$$

$$H_{max} = 1.86H_s \approx 7.514\sqrt{m_0} \quad (34)$$

For wave periods the most important are the following ones (Eq. (35). To Eq. (37)).

$$T_{m_{-1,0}} = T_e = \frac{m_{-1}}{m_0} \quad (35)$$

$$T_{m_{0,2}} = \sqrt{\frac{m_0}{m_2}} \quad (36)$$

$$T_{m_{0,1}} = T_m = \frac{m_0}{m_1} \quad (37)$$

According to Whitehouse (1998), the orbital bottom velocity U_m is dependent on the orbital velocity spectrum σ_u , and can be computed by the following equations (Eq. (38) to Eq. (40)).

$$U_m = \sqrt{2}\sigma_u \quad (38)$$

$$\sigma_u = \int_0^{+\infty} S_u(f) df \quad (39)$$

$$S_u(f) = \left[\frac{2\pi}{T(f) \cdot \sinh\left(\frac{2\pi d}{L(f)}\right)} \right]^2 S(f) \quad (40)$$

The power spectrum of the bottom velocity is represented by $S_u(f)$, the amplitude spectrum is given by $S(f)$, the wave period by $T(f)$ and the wave length by $L(f)$.

There are two substantial spectrum theories, namely the Pierson-Moskowitz (PM) spectrum and the JONSWAP spectrum.

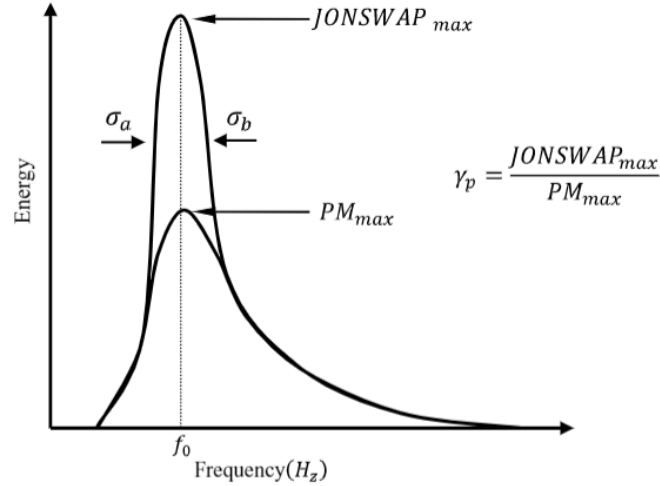


Figure 18 -Pierson-Moskowitz and JONSWAP (Abu Husain et al., 2013)

The JONSWAP includes an enhancement from the Pierson-Moskowitz and according to LeBlond et al. (1982), the enhancement peak can be estimated by the following formula (Eq. (41)).

$$\gamma = \left[\frac{S(f_p)}{\frac{5}{16f_p} H_{m0}^2 e^{-5\sqrt{4}}} \right]^{3/2} \quad (41)$$

For the North Sea conditions this parameter has a value of $\gamma = 3.3$ and the peak period can be related to the moment spectral periods by Eq. (42) to Eq. (44).

$$T_p = 1.107T_{m-1,0} \quad (42)$$

$$T_p = 1.386T_{m0,2} \quad (43)$$

$$T_p = 1.1986T_{m0,1} \quad (44)$$

2.8.3. Breaking point

Another important limitation is the breaking point of waves, which is the point where the propagation of the wave becomes unstable and occurs an abrupt dissipation of energy. This phenomenon occurs when the waves are too steep for deep water, or its heights is too high compared to the water depth for transitional and shallow waters (Chambel, 2019). Numerous studies were conducted to find a good

approximation of the breaking point. Table 2 attempts to summarize the various proposed breaking point estimations.

Table 2 - Breaking point estimations.

Breaking Point	Author
$\frac{H_b}{L} = 0.142$	Michell (1983)
$\frac{H_b}{h_s} = 0.60$	Thornton and Guza (1983)
$\frac{H_b}{d} = 0.78$	US Army of Corps (2012)

2.9. Scour depth

The scour depth is one of the most critical design parameters for offshore foundations. The scour depth corresponds to the maximum eroded depth. It tends to develop asymptotically until its equilibrium, the maximum vertical distance from the surrounding undisturbed bed (Sumer et al., 2001)

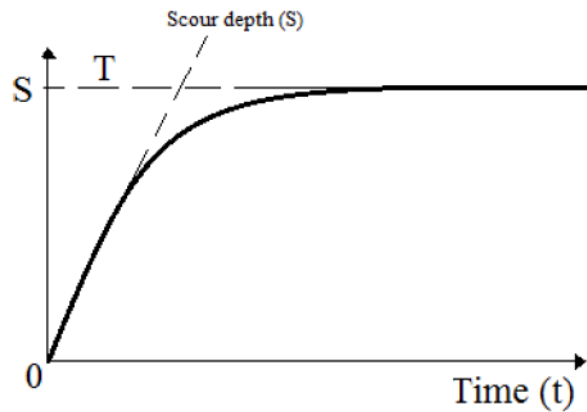


Figure 19 - Scour development as function of time ((Fazeres-Ferradosa, 2018) adapted from (Sumer et al., 2001).

The scour depth varies with time $S(t)$, and the most widely accepted methods were proposed by Melville and Chiew (1999) and Sumer, N, et al. (1992). These methods expressed by equations 45 and 46, in which U is the average velocity, U_{cr} is the critical velocity, T is the time until 63% of S_e , the equilibrium scour (S_e). The variable, t denotes for the time, while t_e stands for the time necessary to reach S_e .

$$S(t) = S_e(1 - \exp(-t/T)) \quad (45)$$

$$\frac{S(t)}{S_e} = \exp\left[-0.33 \left|\frac{U_{cr}}{U} \ln\left(\frac{t}{t_e}\right)\right|^{1.6}\right] \quad (46)$$

Furthermore, t_e , in days, can be assessed by using the expressions pf Eq. (47) and Eq. (48), where d is water depth and D_p is the pile diameter.

$$t_e(days) = \begin{cases} 48.26 \frac{D_p}{U} \left(\frac{U}{U_{cr}} - 0.4 \right), & \frac{d}{D_p} > 6 \\ 48.26 \frac{D_p}{U} \left(\frac{U}{U_{cr}} - 0.4 \right) \left(\frac{d}{D_p} \right)^{0.25}, & \frac{d}{D_p} \leq 6 \end{cases} \quad (47)$$

$$t_e(days) = \begin{cases} 48.26 \frac{D_p}{U} \left(\frac{U}{U_{cr}} - 0.4 \right), & \frac{d}{D_p} > 6 \\ 48.26 \frac{D_p}{U} \left(\frac{U}{U_{cr}} - 0.4 \right) \left(\frac{d}{D_p} \right)^{0.25}, & \frac{d}{D_p} \leq 6 \end{cases} \quad (48)$$

2.9.1 Scour depth for waves

The scour depth at the foot of the monopile is heavily dependent on the pile diameter, as well as on the Keulegan-Carpenter number ($KC = \frac{U_m T}{D}$). According to Sumer, N, et al. (1992), for values of $KC \geq 6$, the scour depth can be predicted using the Eq. (49). Where for cylindrical monopiles A, B and C assume the values of 1.3, 0.03, and 6, respectively (Fazerer-Ferradosa, 2018).

$$\frac{S_e}{D_p} = A[1 - \exp(-B[KC - C])] \quad (49)$$

2.9.2 Scour depth for currents

As for the scour depth prediction for the current effect isolated, (Breusers & Raudkivi, 1991) proposed the Ep. (50) for clear water regime and Ep.(51) for live bed regime.

$$\frac{S_e}{D_p} = 2.3K_s K_\sigma K_\alpha K_{si} K_d \quad (50)$$

$$\frac{S_e}{D_p} = 2.3K_s K_\alpha K_{si} K_d \quad (51)$$

The symbol K_s is the shape factor ($K_s = 1$, for monopiles), K_σ is the grain size distribution factor, K_α is the pier alignment factor ($K_s = 1$, for monopiles), K_{si} is the pier size factor, and K_d is the flow depth factor. More information and simplifications for estimations of K_{si} and K_d values can be found in De Vos (2008). Other methods are used by different author. Sumer and Fredsøe (2002) uses Ep. (52) for live-bed regime where the researcher assumed the value of 0.7 for σ_s (the standard deviation of the scour depth).

$$\frac{S_e}{D_p} = 1.3 + \sigma_s \quad (52)$$

In line with (Whitehouse, 1998), the scour depth is dependent on the shields parameter, expressed by Eq. (53).

$$\frac{S_e}{D_p} = 1.3 \left[2 \sqrt{\frac{\theta}{\theta_{cr}}} - 1 \right] \quad (53)$$

2.9.3. Scour depth for combined waves and currents

The combination of waves and currents effects is a complex phenomenon and does not translate into a linear sum of its individual effects.

The scour depth is lower than for the steady current condition (De Vos, 2008). The velocity ratio U_{cw} (Eq. (54)) is used to assess the weight of each component, corresponding to the ratio between the current velocity, and the sum of the current and wave velocities.

$$U_{cw} = \frac{U_c}{U_c + U_w} \quad (54)$$

In the case for waves and currents combined conditions, the scour depth prediction will fall between the Eq. (47) and Eq. (48) for lower values of U_{cw} and the Eq. (53) for higher values of U_{cw} .

2.7.4. Scour Hole

For non-cohesive soils, the scour hole tends to be shaped like an asymmetrical cone as the one presented in its vertical profile (Figure 20) which is characterized by upstream and downstream slopes, α_{up} and α_{down} , respectively, and its total scour extent W .

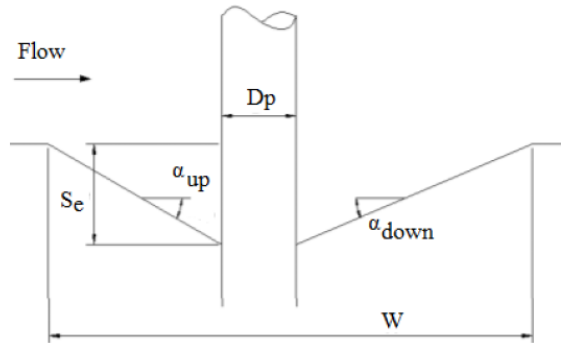


Figure 20 - Scour hole representation (Fazeres-Ferradosa, 2018).

According to De Vos (2008), the scour extent W is given by Eq. (55), where α_{up} is equal to the internal friction angle of the sediments ϕ_i , and the downstream angle tends to be approximately half of the upstream.

$$W = D_p + S_e [\cot(\phi_{up}) + \cot(\phi_{down})] \quad (55)$$

The perpendicular view follows a similar configuration of Figure 20, with both scour slopes equal to ϕ_i , which leads to Eq. (56) (Fazeres-Ferradosa, 2018).

$$W = D_p + 2S_e [\cot(\phi_i)] \quad (56)$$

2.10. Scour in Gravity Based Foundations (GBF)

One of the most common foundations used in the offshore renewable energy sector is the gravity-based foundation (GBF). These structures rely on their own weight for stability in the seabed with lateral support given by pin piles or skirts (Whitehouse et al., 2004), with various shapes as shown in Figure 21.

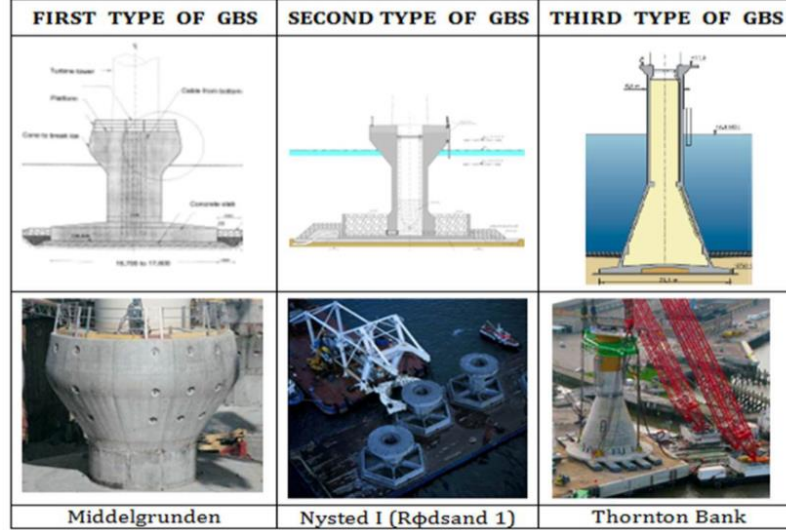


Figure 21 - Different GBF types (Esteban et al., 2015).

The scour processes for these types of foundation are similar to the ones explained earlier for the monopile configuration. The flow acceleration and turbulence generation around the structure induces sediment transport, creating scour holes and sedimentation zones in the vicinity of the foundation.

2.10.1. Scour depth prediction under current

Studies regarding scour processes are much scarcer for gravity-based foundations than for monopiles foundations. One of the few scour predicting methods for GBF was presented by Hoffmans and Verheij (1997), as a modified Khalfin (1983) formula, given in Eq. 57. The pile diameter was replaced by a characteristic diameter D_c , which is the average of the length and the breadth of the GBF. The water depth to the diameter ration (d/D_c) was replaced by the GBF height h_c to diameter ratio (h_c/D). Finally, the depth-average flow velocity is multiplied by $\frac{\alpha_c}{2}$, where the α_c is a constant that represents the additional turbulence in the flow generated by the corner ($\alpha_c = 2$, for circular GBF and $\alpha_c = 2.3$, for rectangular GBF) (Whitehouse et al., 2011).

$$\frac{S}{D_c} = 8.96 \left(2 \frac{0.5\alpha_c U}{U_{cr}} - 1 \right) \left(\frac{h_c}{D} \right)^{1.43} \left(\frac{(0.5\alpha_c U)^2}{gh} \right)^N \quad (57)$$

With $\frac{U}{U_{cr}} = 1$ for $U \geq U_{cr}$ and $N = 0.83 \left(\frac{h_c}{D_c} \right)^{0.34}$.

Note that the experimental data used by Khalfin was for currents only and based on experiments with grain size in the range of 0.12 to 3.0 mm, pile diameter varying from 0.05 to 1.0 m, water depth between 0.05 and 0.98 m, and flow velocity within the range of 0.15 and 0.66 m/s.

Further explanation and detailed review of other scour formulas can be found in (Tavouktsoglou, 2018).

2.10.2. Scour depth prediction under waves

In accordance with Tavouktsoglou (2018), the scour due to wave forcing was examined by Khalfin(1988). Their studies have concluded that the main influencing parameters on scour were the orbital velocity, the relative wavelength and the Ursell number ($Ur = \frac{HL^2}{h^3}$).

Later, Khalfin in 1988, proposed a scour prediction formula for cones and cylinders under incident waves from a data set of 55 scour tests, as shown in Eq. (58).

$$\frac{S}{D} = 0.013 \left(\frac{U_w}{U_c} \right)^{0.4} \left(\frac{D}{L} \right)^{-0.43} Ur^{0.39} \quad (58)$$

2.10.3. Scour depth prediction under waves and currents combined

Experimental results on scour around GBF are extremely scarce, and for that reason scour predicting methods for combined waves and currents for GBF are also limited.

A method for predicting the scour equilibrium depth (S_e), on GBF under combined waves and currents was proposed by Bos et al. (2002). This method is a product of a number of different influencing factors and is given in Eq. 46.

$$\frac{S}{h} = \prod_{i=1}^6 f_i \quad (59)$$

Here $f_1 = 0.044$ is the wave coefficient, f_2 in Eq. (60) is the effect of waves and currents combined, $f_3 = \frac{U_c}{U_{cr}}$ is the relative sediment mobility coefficient, f_4 in Eq. (61) is the structural height effect, f_5 is equal to the shape factor (K_s), and f_6 in Eq. (62), representing the effect of the relative flow depth.

$$f_2 = \frac{A \tanh(3.5(U_{cw} - B) + 1.9 - A)}{A \tanh(-3.5B) + 1.9 - A} \quad (60)$$

$$f_4 = \tanh \left[3.5 U_{cw} \left(\frac{h_c}{h} - 1.4 \right) \right] + 1 \quad (61)$$

$$f_6 = 1.5 \tanh \left(\frac{D_{base}}{h} \right) \quad (62)$$

In Eq. (60), $A = 0.95/(1 + 0.005KC)$, and $B = 0.8/(1 + 0.005KC^2)$.

2.10.4. Transition shapes

Gravity base structures have transition shapes from the top of the structure to the base of the foundation. The differences in the transition shapes have an influence on the flow and the scour patterns. Scour tests carried out by Whitehouse et al. (2004) included a flat-topped structure, as well as a conical shaped transition. The overall scour for the conical shape was deeper than for the flat-topped shape as demonstrated in the obtained results (Figure 22). The flat top of the second shape tends to block some part of the downwards flow responsible for the scour.

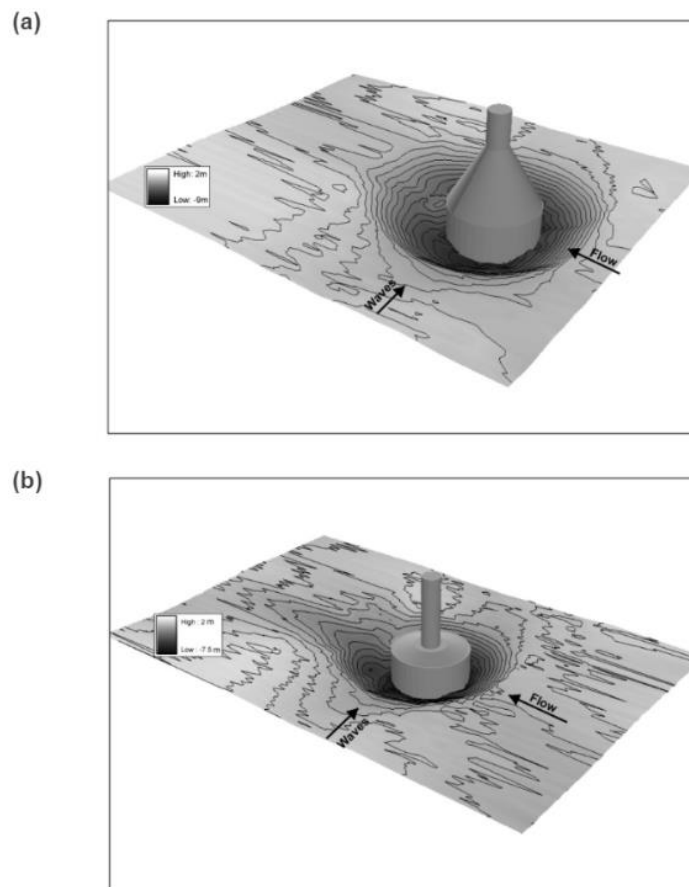


Figure 22 - Scour depth for GBS with different transition shapes (Whitehouse et al., 2011); a)conical transition b)flat-topped transition

2.10.5. Shortcomings in scour prediction around GBF

According to Tavouktsoglou (2018), the gravity base foundation only recently has become a viable and appealing option for offshore wind farms, and for that reason the significant research on the time evolution of scour in such structures has not been conducted yet.

In contrast with the monopile structure, the GBF configuration has much more complex and distinct types of shapes that make the research in these types of structure far less developed. The existing method of scour prediction lack in accounting the different possible geometries and in linking key hydraulic processes.

2.11. Sediment Characteristics

One of the most influential parameters of scour is the seabed soil characteristics. Usually, the seabed is composed by cohesive soils including clays or non-cohesive sediments such as sands.

The present research focuses on scour mechanisms and sediment transport of non-cohesive sediments. The most critical characteristics of sand are:

- density;
- size;
- shape;
- weight; and
- gradation.

The mass density ρ_s has major influence in the stability of the soils since it determines the gravitational force of the particles as seen in subchapter 2.3 threshold of motion and corresponds to the ration between the mass per unit volume (Kg/m^3).

The sediment gradation is a measure of the spread of the distribution of the sand particle sizes and is traditionally defined by the geometric standard deviation, as expressed in Eq. (63).

$$\sigma_g = \frac{d_{84}}{d_{50}} \approx \sqrt{\frac{d_{84}}{d_{16}}} \quad (63)$$

In Eq. (63), the parameters represented in the form of d_x , refers to the sediment size for which x% is finer by weight.

2.12. Hybrid Marine Renewable Energy (MRE) investments

With optimization goals, the Marine Renewable Energy (MRE) industry is aiming at investing in the hybridization of marine renewable technologies, with more than one harvesting technology, e.g., offshore wind turbines combined with wave energy converters (WECs) (Fazeres-Ferradosa et al., 2021). However, the presence of these WEC devices near the structure imposes another degree of complexity in scour analysis. The scour may be enhanced due to the cyclical motion of these devices. In the other hand, the body of the WEC may cause the dissipation of the wave energy decreasing the orbital velocity, and thus, have a reduced effect in bed shear stress that leads to scour. Either way scour near the foundation remains a potential cause of instability.

Little research about the effects of these hybrid structures in the scour was made, making the existing design methods available often over-conservative.

A wave energy converter is a device capable of harvesting the ocean waves energy and converting said energy into electrical energy. This objective can be achieved using a variety of different functioning principles. The following list, adapted from MOREnergy lab (2022) is a small review of some of the existing WEC devices.

- Oscillating water column

This device has an air chamber, and when the air inside that chamber is compressed by the rising water level due to waves, the air goes through the turbine on top, thus creating electric energy (Figure 23).



Figure 23 - Oscillating water column (MOREnergy lab, 2022).

- Oscillating wave surge converter

An example of this type of wave energy converter is the wave roller (Chehaze et al., 2016). This device, usually fixed on the seabed, is a reliable converter of wave energy into electric energy from the relative motion of the oscillating part (Figure 24).

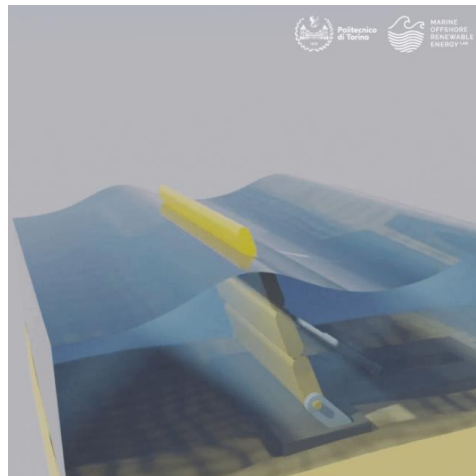


Figure 24 - Oscillating wave surge converter (MOREnergy lab, 2022).

- Overtopping device

This type of device utilizes its long structure to fill a water reservoir located in a higher position relative to the water surface that goes through low-head turbines (Figure 25).

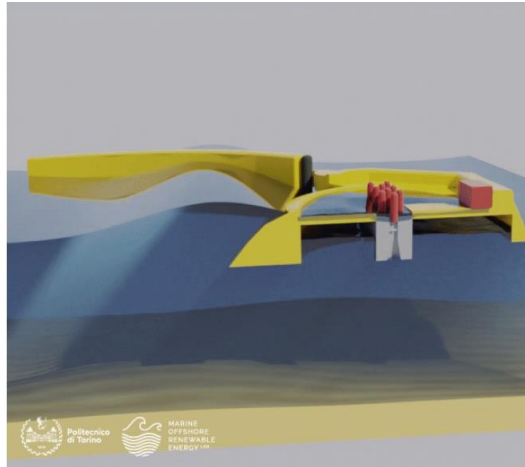


Figure 25 - Overtopping device (MOREnergy lab, 2022).

The present research will focus on the effects in scour of the application of an oscillating wave energy converter or oscillating wave surge converter in the upstream of a monopile foundation and a gravity base foundation.

Further descriptions of other types of WECs, e.g. near-shore point absorber, rotating mass generator, surface attenuator and more, can be found in MOREnergy lab (2022).

2.13. Scour tests review

To better analyse and interpret the results of the present research it is important to compare them with previous works and tests performed by other authors. The offshore wind turbine foundation scour has been extensively studied for the monopile configuration, and recently some gravity base foundation scour studies have been developed.

This subchapter of the present work is an attempt to summarize some of the aforementioned studies with different extreme sea conditions and various seabed compositions.

2.13.1 Scour tests for monopile foundation

The study conducted by Sumer, Fredsøe, et al. (1992) gives an extensive data-set of experimental results for scour under wave action for various conditions, and concludes that the major parameter influencing the equilibrium scour depth on live bed scour conditions is the Koulegan-Carpenter (KC) number, as well as indicates that the equilibrium scour depth lies in the interval of $0.1-1.0D$.

For currents, some important contributions provided by Melville and Raudkivi (1977), Raudkivi and Ettema (1977), Melville and Sutherland (1988) have shown that the scour depth to diameter ratio, S/D , (1) increases with h/D , (2) increases with shields parameter θ , with a slight dip in the transition from clear-water and live-bed regime, (3) decreases with increasing sediment gradation, (4) increases with increasing D/d , (5) increases with Froude number. Depending on the previous parameter, the scour depth, S , tends to fall in the range of $1-2.5D$.

From the research conducted by Sumer and Fredsøe (2001), it is possible to conclude that the major parameter influencing these results is the U_{cw} . When U_{cw} tends to 0, the expected scour depth is approximated to the waves case and when U_{cw} tends to 1 ($U_{cw} \geq 0.7$) the expected scour is approximately like the current case.

Table 3 summarizes the test conditions and scour results from previous scour tests conducted by Sumer, Fredsøe, et al. (1992), Sumer and Fredsøe (2001), and Qi and Gao (2014).

Table 3 - Review on existing Scour tests results.

Author	(Sumer, Fredsøe, et al., 1992)			(Sumer & Fredsøe, 2001)			(Qi & Gao, 2014)
Test Series	1	2	3	1	2	3	1
$d_{50}(mm)$	0.18-0.58	0.18	0.36	0.16	0.16	0.16	0.38
D(mm)	10-50	100-200	50-110	30-90	30-90	30-90	80-200
$f(s^{-1})$	0.32-0.84	0.22-0.53	~	0.3	0.3	~	0.05-0.71
$U_c(cm/s)$	~	~	47.1	8.3-45.9	~	44.9-45.9	10.7-34
$U_m(cm/s)$	11.2-37.8	23.1-53.3	~	15.7-24.2	15.7-24.2	~	15-49.7
KC	4.9-51.0	4.4-24.0	1.285-5.625	4-26	4-26	~	0.44-3.03
S/D	0-1.1	0-0.31	0.92-1.56	0.11-1.67	0.06-0.83	1.21-2.0	0-1.26

Research on layered seabed configurations was performed in (Porter et al., 2012), and (Porter et al., 2013). In these studies, two different sand grain sizes were considered, and tests were made for four soil types (coarse sand, fine sand, fine sand with underlying coarser sand and coarse sand with underlying fine sand). The following conclusions were delivered from the results of these studies:

- scour depth in the upper fine sand layer was similar to the uniform fine sand;
- scour in the underlying coarser sand layer was enhanced from the uniform bed of coarse sand;
- there is a limit to the scour enhancement that depends on the upper fine sand layer depth;
- For larger upper fine sand layers, scour depth is limited by the upper layer depth and no scour occurs in the underlying coarser layer; and
- In the lower coarse sand layer, the scour enhancement was found to occur in the entire range of flow conditions.

2.13.2 Scour tests for GBF

Due to the high complexity and diversity of these foundations, it is much harder to find acceptable relations and conclusions. However, a more extensive analysis of the scour depth was conducted by Whitehouse et al. (2011).

Field observations performed by Dahlberg (1983) reported the scour at Frigg TP1 GBS in the North Sea, where the soil consisted in fine sand with a size range of 0.1-0.2 mm. Observations in 104 m of water of this square foundation with dimensions of 72 m square and 44 m high, revealed scour holes of 2 meters around both corners. Field measurement in shallower waters from the North Sea (30 m to 40 m) of rectangular GBF shape (75m by 80m by 16m high in 42.5 m of water) revealed scour depth between 2.5m and 3.5m in 0.15 mm fine sand (Bos et al., 2002).

An experimental scour research carried out by Whitehouse et al. (2004), of a 20 m diameter circular skirted caisson, in a wave current flume showed that the use of skirted foundations provide some protection against scour. However, it also may promote continuing development of scour. Another conclusion from the Whitehouse et al. (2004) studies was that the scour depth under the forcing of currents around a cylindrical base GBF is around $0.18D_{base}$, while under wave action for conical and cylindrical structures it is approximately $0.04D_{base}$, which is 4 times smaller than for currents

More recently, Tavouktsoglou (2018) did an extensive research on scour for different GBF configuration and conditions. The extent of this study included a small-scale experiment with 6 different geometries, truncated, 3 conical base and a uniform cylinder as illustrated in Figure 26, and a large-scale experiment with 4 geometries as shown in Figure 27.

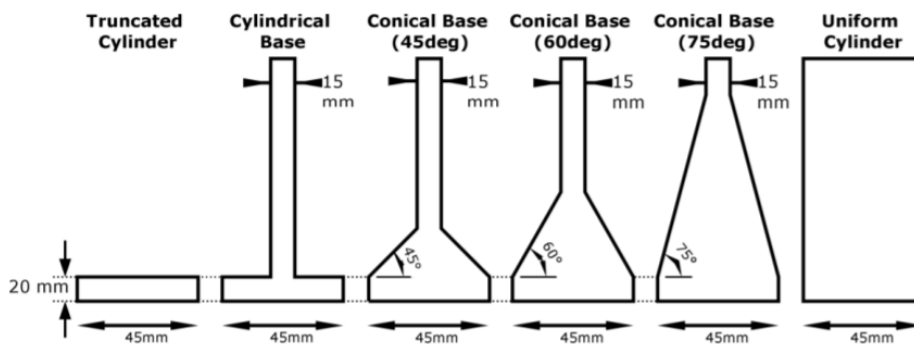


Figure 26 - Small scale foundation geometries (Tavouktsoglou, 2018).

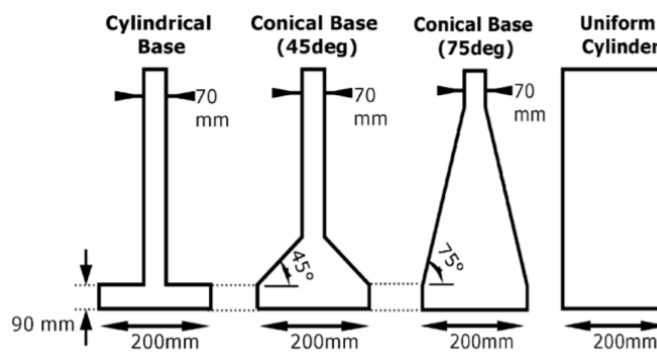


Figure 27 – Large scale foundation geometries (Tavouktsoglou, 2018).

The following table (Table 4) presents a summary of results from the studies carried out by Tavouktsoglou (2018)

Table 4 - Summary of results from (Tavouktsoglou, 2018).

Structure Type	U_c (m/s)	h(m)	D or D_{base}	d_{50} (mm)	S/D_{Base}
Truncated	0.143-0.264	0.100-0.165	45 mm	0.2-0,6	0.1-1.02
Cylindrical Base	0.143-0.264	0.100-0.165	45 mm	0.2-0,6	0.59-1.39
45° Conical Base	0.143-0.264	0.100-0.165	45 mm	0.2-0,6	0.87-1.49
60° Conical Base	0.143-0.264	0.100-0.165	45 mm	0.2-0,6	0.95-1.53
75° Conical Base	0.143-0.264	0.100-0.165	45 mm	0.2-0,6	1.12-1.64
Uniform Cylinder	0.143-0.264	0.100-0.165	45 mm	0.2-0,6	1.43-2
Cylindrical Base	0.245-0.540	0.35-0.55	200	0.2	0.32-0.72
45° Conical Base	0.245-0.540	0.35-0.55	200	0.2	0.41-0.78
75° Conical Base	0.245-0.540	0.35-0.55	200	0.2	0.51-0.84

2.14. Scale and model effects

Usually, researchers support their studies with physical, numerical, and composite modelling. The current research will be supported by a physical model. Physical modelling consists in a reduction of scale, using a scale factor λ given in Eq. (64), of the prototype conditions to be possible to replicate large prototype models in the limited space of laboratories. A similitude criterion must be used to correctly reproduce the prototype conditions. Similarity is achieved when the model conditions are geometrical, kinematical and dynamically similar to the prototype conditions (Frostick et al., 2011).

$$\lambda = \frac{X_M}{X_P} \quad (64)$$

According to De Vos (2008), the main advantage of physical models compared to numerical ones is that in former there is no need to simplify governing physical processes and non-linear terms. Furthermore, physical models represent a cheaper option from field observations, and can be performed with isolated loading conditions. However, this scaling causes some scale and model effects discrepancies (Frostick et al., 2011).

If the force ratios between model and prototype are significantly different, scale effects will arise, resulting in deviations on the physical model conditions which subsequently lead to oversimplifications (Frostick et al., 2011), e.g., different pile roughness between model and prototype, different boundary layers (Fazeres-Ferradosa, 2018).

If due to physical limitations of the model set-up in laboratory, non-existing or unreal prototypes boundaries are introduced, model effects will occur (Frostick et al., 2011), e.g., wave reflection, side wall effects, bottom topography etc. (Fazeres-Ferradosa, 2018).

Effects like wave reflection and blockage must be studied and controlled (Chambel, 2019). Regarding the wave reflection, this type of phenomenon should be investigated and minimized with model changes such as the creation of a dissipation beach whether necessary. As for the blockage effects, Whitehouse (1998) recommends a ratio below 1/6 between perpendicular-to-flow area to flume width.

Regarding the seabed sediment scaling, as the diameter decreases the non-cohesive sediments acquire cohesive properties, which leads to significant scale effects (Chambel, 2019). It is important to use non-cohesive sediments in the model even if not properly scaled. For that reason, the model sediments, ripples and bed roughness will not be correctly scaled with the prototype conditions (Fazeres-Ferradosa, 2018).

In most cases, the simultaneously similarity of geometric, kinematic, and dynamic variables is not possible, thus it is necessary to neglect some similarities, being the dynamic similitude the most suitable. The similarity between two geometrical and kinematic systems derives from Newton's 2nd law according to Frostick et al. (2011), as expressed in Eq. (65).

$$m \frac{dU}{dt} = \sum_n \bar{F}_n \Rightarrow \bar{F}_i + \bar{F}_{il} = \bar{F}_g + \bar{F}_\mu + \bar{F}_e + \bar{F}_p + \bar{F}_\sigma \Leftrightarrow 1 \quad (65)$$

$$= \frac{(\bar{F}_g)}{(\bar{F}_i)} + \frac{(\bar{F}_\mu)}{(\bar{F}_i)} + \frac{(\bar{F}_e)}{(\bar{F}_i)} + \frac{(\bar{F}_p)}{(\bar{F}_i)} + \frac{(\bar{F}_g)}{(\bar{F}_i)} + \frac{(\bar{F}_\sigma)}{(\bar{F}_i)} - \frac{(\bar{F}_{il})}{(\bar{F}_i)}$$

Here, \bar{F}_n is the external force, \bar{F}_i is the inertia force, \bar{F}_{il} refers to the local inertia force, \bar{F}_g is the gravitational force, \bar{F}_μ stands for the friction force, \bar{F}_e denotes the elastic compression force, \bar{F}_p is the pressure force, and \bar{F}_σ corresponds the surface tension force.

The most common similitude laws result from equating the scale factor of inertia with other scale factors, e.g., the Froude similarity ($Fr_{prototype} = Fr_{model}$) and Reynolds similarity ($Re_{prototype} = Re_{model}$) shown in Ep. (66) and Eq. (67), in line with Frostick et al. (2011). Other similitude laws are used in other types of physical models, e.g., Weber similitude in overtopping or wave breaking, Euler similitude in cavitation phenomena.

$$Fr = \sqrt{\frac{F_i}{F_g}} = \frac{U^2}{gL} \quad (66)$$

$$Re = \frac{F_i}{F_\mu} = \frac{\rho UL}{\mu} \quad (67)$$

To achieve a correct scaling in the laboratory the Froude number and the Reynolds number should be preserved, conserving the gravity and viscous effects respectively (Chambel, 2019). However, it is not possible to scale both simultaneously. For scour models, it is crucial to preserve the hydrodynamic conditions, and for that reason, the Froude similitude should be adopted in favour of the Reynolds similitude.

Table 5 gives a summary of some of the most important scale factors used in the current research. Note that λ_ϑ represents the ratio between the kinematic viscosity of the model and the prototype.

Table 5 - Some of the most important scale factors.

Scale factor	Froude similitude	Reynolds similitude
Geometric	$\lambda = \lambda_L$	$\lambda = \lambda_L$
Area	$\lambda_A = \lambda_L^2$	$\lambda_A = \lambda_L^2$
Velocity	$\lambda_u = \sqrt{\lambda_L}$	$\lambda_u = \frac{\lambda_\vartheta}{\lambda_L}$
Time	$\lambda_T = \sqrt{\lambda_L}$	$\lambda_T = \frac{\lambda_L^2}{\lambda_\vartheta}$
Volume	$\lambda_V = \lambda_L^3$	$\lambda_V = \lambda_L^3$

3

PHYSICAL MODEL SET-UP

The present research aims to expand the scour tests on complex soils for different types of foundation, and to create a preliminary study on the hybridization of an oscillation wave surge converter with the foundation of offshore structures such as offshore wind farms. This experimental study includes the combination of two different foundation physical models, the monopile configuration and a GBF configuration, two distinct soil types, uniform fine sand, and layered sand with upper coarser sand, under combined waves and current hydrodynamic conditions. This study will also be expanded with tests for the same conditions explained before in the presence of an oscillating wave surge converter to evaluate the negative or positive effects in scour of the presence of said device.

The experimental works performed are the main objective of this dissertation, and for that reason the correct scaling and quality of installation of the different models are extremely important.

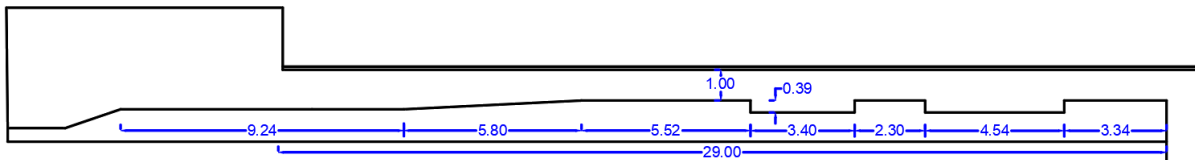
This chapter describes the laboratory set-up and all the auxiliary equipment utilized to install and calibrate the models as well as the test conditions and adaptation works performed before the experimental study.

3.1. Laboratory Set-Up

3.1.1 Flume at Faculty of Engineering of the University of Porto (FEUP)

The scour analysis research was conducted at FEUP in the Hydraulics Laboratory, at the water resources and environment division (SHRHA). The hydraulics laboratory is equipped with a wave and current flume capable of replicating offshore conditions with the following layout shown in Figure 28.

Flume layout Side View



Flume layout Top View

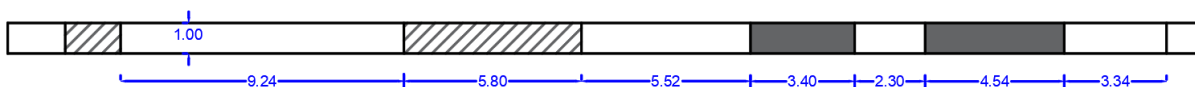


Figure 28 - Layout scheme of FEUP flume (dimensions in meters).

The wave and current flume (Figure 29) is around 29 meters long, 1 meter wide, and 1 meter deep. The flume has a maximum depth of 1.39 m at two sediment boxes. These boxes have a length of 3.4 m and 4.54 m. This is a large flume that operates in a closed circuit, in which the water is pumped by 4 pumps in parallel from two reservoirs located in the lower level. The pumped water is redirected to a constant head reservoir with dimensions of 12.3 m by 3.3 m and 1.3 m depth, 3.02 m above the flume floor (Figure 30). The flume is fed by two intake pipelines equipped with regulation valves. Both pipelines have a flowmeter that shows the discharge flow in order to regulate the flume flow. An approach ramp between the intake and the two sediment boxes was built with 5.8 m long and 1/20 slope to overcome the levelled floors and avoid abrupt changes in bathymetry (Chambel, 2019). To regulate the water depth, the flume is equipped with a mechanical gate at the downstream end.



Figure 29 – Flume general views.



Figure 30 - Constant head reservoir.

In the space between the flume intake and the approach ramp a wavemaker commissioned by HR Wallingford (UK) was installed. This equipment is a piston type flume wavemaker, with a single paddle that moves horizontally. The paddle, of dimensions of 1 m wide and 1 m high, can reproduce a single wave or regular and irregular series of waves. The equipment has an active absorption module of wave reflections incorporated, the *Dynamic Wave Absorption System*, which was implemented to reduce the effects of the reflection by the model walls and downstream gate. According to Rosa-Santos (2010), the reflected waves would create an overlap with the generating waves that would lead to forming smaller

or bigger waves than intended originally. When the reflection is too high, the safety trigger activates and shuts down the wave paddle. The wavemaker is composed of structural, electrical (Figure 31) and software components. A list of the main components is summarized in the Table 6.

Table 6 - List of main wavemaker components (Adapted from (Chambel, 2019)).

Structural components	Electrical components	Software
Beam covers; Paddle and respective wishbone bracing; 2 paddle retainer brackets; Foam absorption beach; 4 safety covers; Front and rear beam support; 2 flume mounting brackets;	Electrical drive actuator; Low inertia AC servo Motor; MDCP; Light beacon; Wave generator computer; Remote paddle safety unit;	HR Merlin; HR DAQ Suite



Figure 31 - Structural (left) and electrical (right) components.

The Figure 32 shows the top/front view and cross-sections of the wavemaker with the main structural and electrical components. The low inertia motor on the top of the equipment moves the paddle horizontally. The light beacon, on top of the Motor Drive Control Panel (MDCP), has 4 different lights and a bell which gives information about the possible wavemaker states.

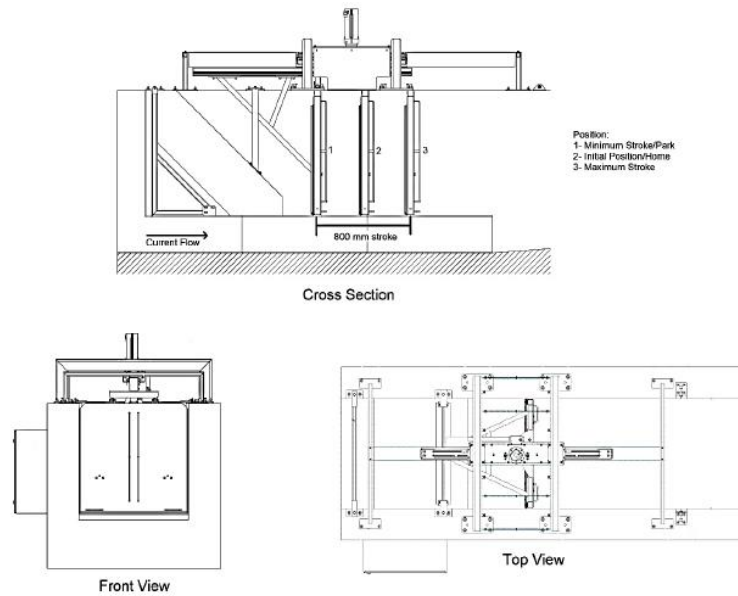


Figure 32 - Wavemaker main components scheme (Adapted from (Chambel, 2019)).

The wave generator computer (Figure 33) has the software HR Merlin. HR Merlin is a wave generator software which is necessary to control the wavemaker and simulate a certain sea state. For the present study, the Joint North Sea Wave Project (JONSWAP) spectrum was used since it simulates the typical North Sea, which is a common location for offshore renewable energy structures such as windfarms. However, there is a wide variety of irregular sea states wave spectra available to reproduce in HR Merlin such as:

- Pierson-Moskowitz;
- International Towing Tank Congress (ITTC);
- Darbyshire Costal;
- Darbyshire Ocean;
- Neumann;
- Top-Hat; and
- Bretschneider.

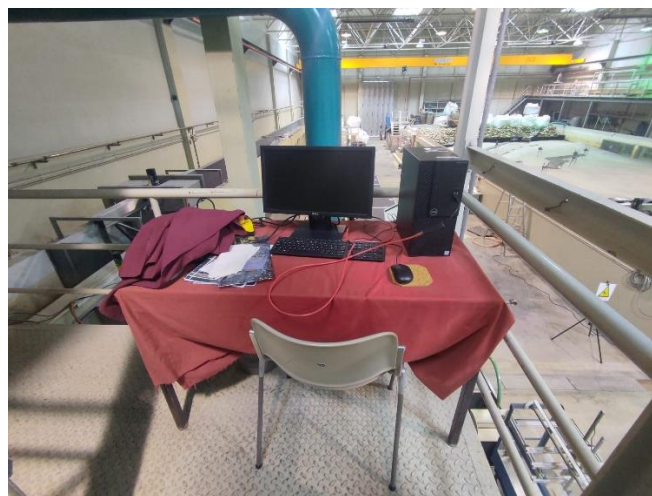


Figure 33 - Wave generator computer.

3.2. Foundations and WEC models

3.2.1 Foundation models

For the experimental study of this dissertation, two foundation physical models were used to replicate common marine infrastructures of support for offshore renewable energy investments.

The selected monopile diameter was $D_p = 5.5$ m. To simulate the geometry of the monopile foundation, a plastic pile with an 0.11 m diameter (Figure 34) was available from previous scour studies performed at SHRHA. This pile model consists of 3 detachable parts and a square plate at the base to add stability to the model and to facilitate its use. Following the Froude similitude, the model corresponds to geometric model scale of $\lambda = 1/50$.



Figure 34 - Monopile model.

A gravity-based foundation model was not available at SHRHA. In order to recreate the GBF, a new model was developed with a geometric model scale of $\lambda = 1/50$. A 60° conical shape with a cylindrical skirt was chosen for the foundation geometry with dimensions represented in Figure 35.

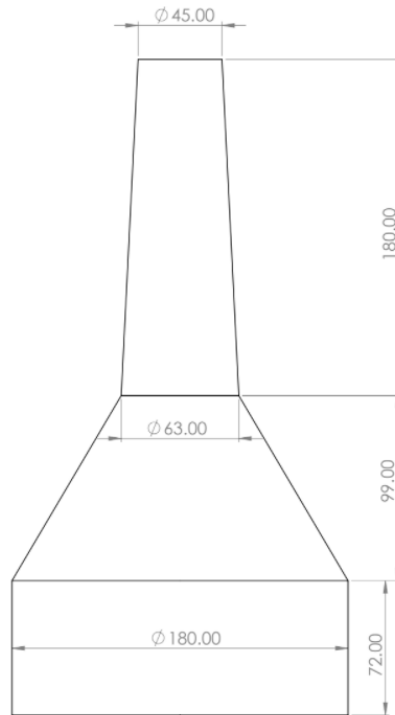


Figure 35 - GBF model dimensions (dimensions in mm).

In order to build this model, a *WASP* 3D printer was used to assemble the mold for the concrete pour. The final model consisted of 4 detachable mold parts, which were printed and later concreted. The molds were printed in such a way that the respective parts incorporate the final model as shown in Figure 36.



Figure 36 – Isolated parts (left) and final model assembled (right).

However, the mold was printed using Polylactic acid (PLA) which is biodegradable and non-resistant to water. And even though the exterior was isolated to prevent the degradation of the PLA, after the model was submerged and tested, the printed material disintegrated (Figure 37).

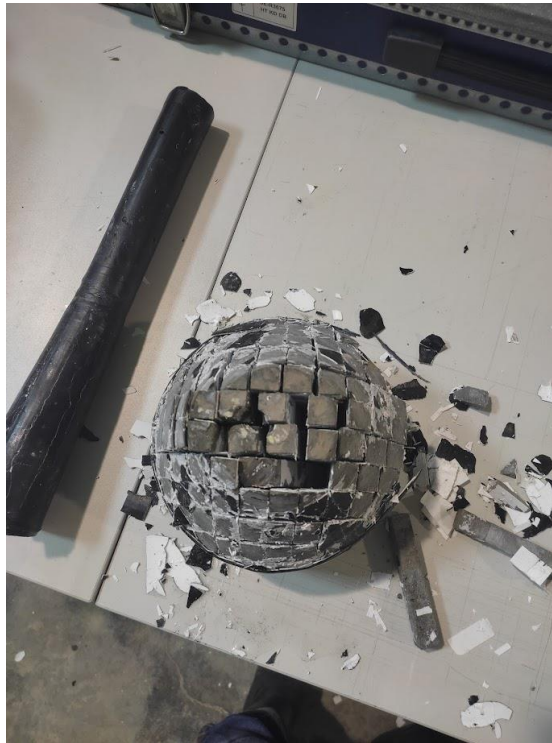


Figure 37 - First GBF model disintegrated.

A second attempt to build the GBF model was made, this time with a removable hollow mold. Then the mold was concreted using a metal rod to keep the two molds in place (Figure 38).



Figure 38 - Outside mold (left); and final concrete GBF model (right).

Note that a normal base diameter used for gravity-based foundations in the offshore wind sector could reach values seven times larger than the monopile diameter (Esteban et al., 2019). However, due to the limitations imposed by the 3D printer machine dimensions and the flow blockage limits of 1/6 of perpendicular-to-flow model area to flow section indicated by Whitehouse (1998), the GBF model dimensions used fall short from the normal relation between monopile dimension and GBF dimension.

3.2.2 WEC model

In order to study the possible positive or negative effects of the deployment of WEC devices in the proximity of offshore windfarm foundations, an oscillating wave surge converter model was made. The WEC model was constituted by 2 parts, a 0.40x0.20 m acrylic base and a 0.15x0.10 m plastic paddle with one degree of rotation mobility by the axis attached to the acrylic base. Furthermore, both sides of the plastic paddle had a small metal spring attached using fishing line as shown in Figure 39. In addition, it should be noted that rigidity of the the metal springs was not scaled.

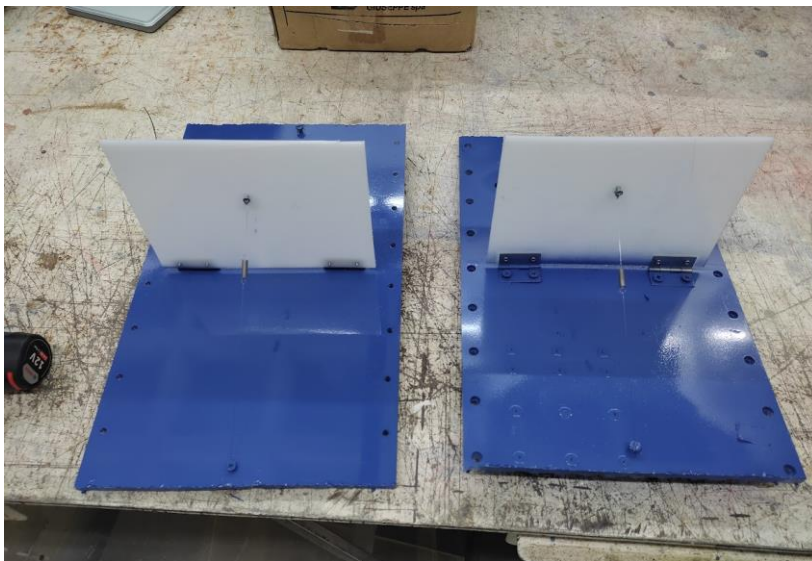


Figure 39 - WEC models.

For this experimental study, the oscillating wave surge converter model was selected instead of other types of wave energy converters for the following reasons:

- similar oscillating wave surge converter models were being studied simultaneously at hydraulics laboratory;
- fixed bottom device; and
- considerable influence on flow velocity profiles.

The scour mechanisms occur due to soil-fluid-structure interactions, and since the oscillating wave surge converter is a fixed bottom device, scour testing using these types of devices has an increased interest. Another important factor that increases the interest in scour testing for these types of devices is the fact that the oscillating wave surge converter paddle is expected to have a large influence on the flow since it constitutes a physical disturbance to the flow profile incident in the base of the foundation.

3.3. Soil models

One of the main objectives of this study was to identify the scour behaviour of soils with different characteristics. For this study, two distinct sands were used, one classified as fine sand and the other as coarse sand.

Using these types of sand, tests were conducted for two configurations, a uniform fine sand and a layered sand with upper coarser sand. Due to limitations on time and total volume of the coarser sand, it was not possible to perform tests for uniform coarser sand or layered sand with upper fine sand.

3.3.1 Uniform fine sand

The first tests were performed on a uniform fine sand and therefore with non-cohesive properties. The most important soil characteristics is herein described.

The available fine sand material was SP 55 silica sand, from *SIBELCO Portuguesa Lda*. According to Silva (2010), this sand has a mean diameter of $d_s=0.273$ mm and a density of $\rho_s=2650$ kg/m³. A sieving and sediment analysis was performed in line with the Portuguese Norm NP EN 933-1. The sediment analysis is given in Table 7.

Table 7 - Sediment analysis of SP 55 fine sand (Adapted from (Silva, 2010)).

Sieve Opening (mm)	Retained (%)	Cumulative Retained (%)	Cumulative passing (%)
1.0	0.0	0.0	100.0
0.710	0.0	0.0	100.0
0.500	0.0	0.0	100.0
0.355	4.67	4.67	95.33
0.250	58.20	62.87	37.13
0.180	29.66	92.53	7.47
0.125	7.12	99.65	0.35
0.090	0.34	99.99	0.01
0.063	0.01	100.0	0.0
<0.063	0.0	100.0	0.0

From the sediment analysis and their results, it is possible to draw the grading curve shown in Figure 40.

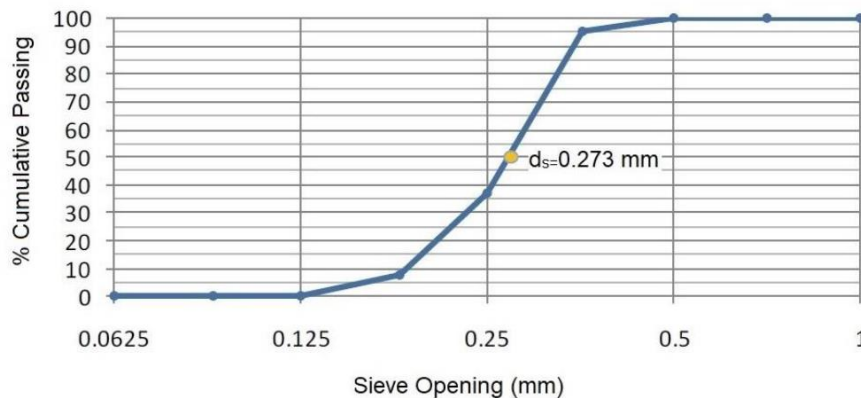


Figure 40 - SP 55 fine sand grading curve ((Chambel, 2019) adapted from (Silva, 2010)).

3.3.2 Layered sand with upper coarse sand

The second soil configuration tested was the layered sand with upper coarse sand. For the deeper layer the same SP 55 sand was used. For the upper layer, the sand was provided by the Construction Materials Testing Laboratory (LEMC) from FEUP. This upper coarser sand has a mean diameter, d_{50} , of 0.4 mm, a density, ρ_s , of 2694 kg/m³.

In the following table (Table 8) are the results of the sediment analysis performed in LEMC using sieves with different sizes.

Table 8 - Sediment analysis of the coarse sand performed by LEMC.

Sieve Opening (mm)	Retained (%)	Cumulative Retained (%)	Cumulative passing (%)
8.0	0.0	0.0	100.0
4.0	0.0	0.0	100.0
2.0	2.1	2.1	97.9
1.0	15.9	17.9	82.1
0.500	23.4	41.4	58.6
0.250	22.5	63.9	36.1
0.125	18.1	82.0	18.0
0.063	12.4	94.4	5.6
P	0.9	95.3	4.7

From the sediment analysis results, is possible to draw the grading curve provided in Figure 41.

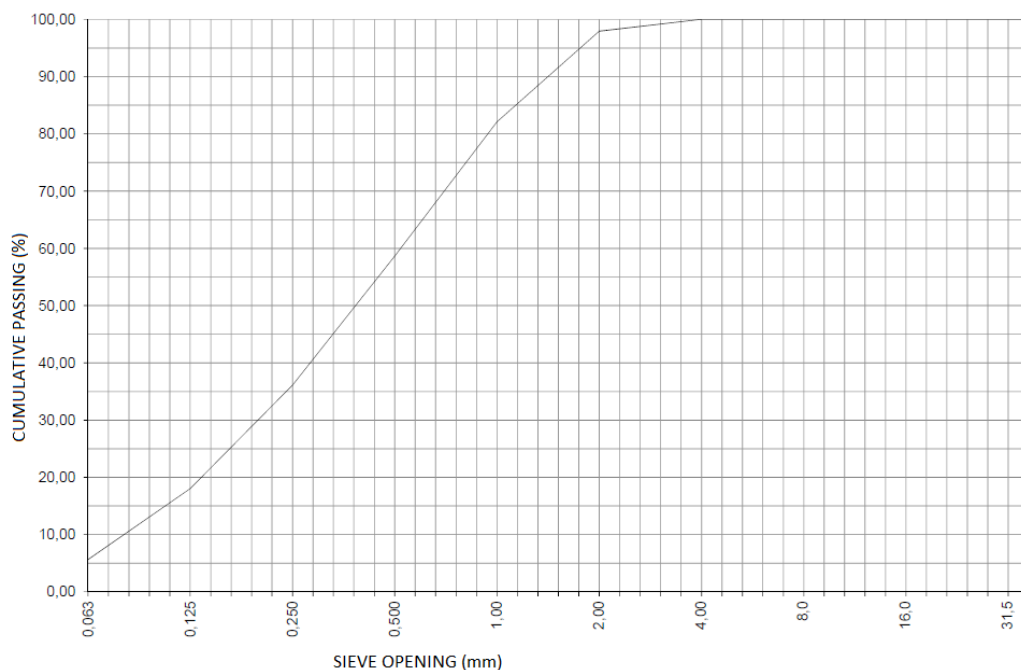


Figure 41 - Coarse sand grading curve.

3.4. Target hydrodynamic conditions

Tests were performed to simulate the sea state by combining waves and currents. For this study, it was chosen to simulate the North Sea conditions, as aforementioned this sea is a common location for renewable energy structures such as windfarms, having the majority of the existing offshore wind farms, as well as the majority of future new investments in offshore wind sector (WindEurope, 2022b).

The current speed target condition was considered, aiming to create a near live-bed regime. An 18 meter water depth was chosen as it is a common value in North Sea windfarms. In order to calculate the critical depth average speed of the prototype conditions (Table 9), the method introduced in Soulsby (1997) was

used. The resulting dimensionless Shields parameter of $D^*=5.55$ leads to a critical depth average speed, U_{cr} , of 0.27 m/s.

Table 9 – Target prototype conditions

Median grain size (d_s)	Water depth (d)	Density of particles (ρ_s)	Density of fluid (ρ)
0.273 mm	18 m	2650 kg/m ³	1027 kg/m ³

The model conditions (Table 10) were obtained by scaling the water depth with the Froude similitude to $\lambda = 1:50$ (see subchapter 2.12). The sediment characteristics were not scaled.

Table 10 - Target model conditions

Median grain size (d_s)	Water depth (d)	Depth average speed (U_c)
0.273 mm	0.36 m	0.27 m/s

The waves and current hydrodynamics used in this study (Table 11) were carried out for an irregular sea state from the JONSWAP wave spectrum with a typical North Sea peak enhancement factor of $\gamma = 3.3$.

Table 11 - Target prototype flow conditions

Water depth (d)	Significant wave height (H_s)	Peak Period (T_p)	Depth average speed (U_c)	Maximum wave orbital velocity (U_m)
18 m	6 m	12 s	0.277 m/s	1.20 m/s

These conditions were chosen considering the typical North Sea conditions and keeping in mind the achieved conditions in a similar study made by Chambel (2019), which was made in the same wave and current flume. The maximum wave orbital velocity U_m value was obtained using the method developed in Wiberg and Sherwood (2008).

It should be noted that these target conditions were not met. Further explanation and description of the calibration process can be found in subchapter 4.2.

3.5. Scale and model effects considerations

Several scale and model effects are expected and should be considered. Model effects such as flow blockage, wave reflection and wave dispersion after passing the first foundation could have a significant impact on the results. Scale effects due to the non-scaling of the sediment are also expected.

Regarding the flow blockage, both models verify the rule of thumb from Whitehouse (1998) that states that for models with projected area smaller than 1/6 of the total area of the flow the flow, blockage can be neglected.

Reflection was expected to be high in the flume used in this experimental work, and for that reason a reflection analysis and possible construction of a dissipation beach was needed. A further explanation and description of the method used to perform this reflection analysis can be found in subchapter 4.1.2.

In the present research, two consecutive sediment boxes with foundation model were used in sequence. For that reason, the upstream model will cause effects on the flow in the downstream model. However, the distance between the models was around 5.7 m, which corresponds to 57D of the monopile. Studies about the flow variability caused by a monopile made in Miles et al. (2017) revealed the following:

- for current-only tests, the mean flow was reduced immediately downstream of the pile, however flow velocity returned to within 5% of background levels at 8.3D downstream; and
- For tests with waves the oscillatory velocities reduced immediately down-wave of the pile and returned quickly to background levels by 1.65 to 3.5D downstream of the pile.

As the GBF model is located 57D of the monopile model, the flow velocity and oscillatory wave velocity are expected to be the same.

Note that this WEC model is a simplification of a complex oscillating wave surge converter device. Several aspects of this model were not scaled, such as the foundation shape, wave paddle curvature, and metal spring rigidity. For that reason, scale effects were expected in the oscillatory movement of the oscillating wave surge converter paddle.

4

Experimental Study

This chapter aims to describe the experimental study, the various intermediate steps, the measurement techniques and the equipment used. However, in order to correctly perform the experimental phase of this study, it is important to calibrate and verify the correct conditions. For that reason, this chapter also describes all the laboratory procedures executed concerning the definition and calibration of the experimental conditions.

Furthermore, this chapter includes a deeper analysis of the experimental results. This analysis comprises the comparison of the results for different test configurations (with or without the presence of the WEC model), and the relation between scour depth and different soil characteristics.

4.1 Flow conditions calibration

4.1.1 Velocity Profiles

In order to correctly perform the various physical model tests of this dissertation it was necessary to calibrate the flow conditions. The wave and current flume at FEUP, as referred in subchapter 3.1, has two intake pipelines equipped with regulation valves, however only one of those valves has a functioning flowmeter. For that reason, the following calibration method was used:

- confirm flow velocities using only the intake pipeline with the functioning flowmeter;
- estimate the flume losses; and
- confirm flow velocities of the experimental conditions, using both intake pipelines.

To confirm the flow velocity, an Acoustic Doppler Velocimetry (ADV) from Nortek, was used. This equipment can measure the flow velocity by applying the Doppler effect, as well as the distance to the bottom of the channel and temperature. To fix the equipment into the channel, a wooden and metal support structure was created as shown in Figure 42.



Figure 42 - ADV and support structure.

Firstly, three velocity profiles were taken using the ADV to confirm the flow velocities using only the intake pipeline connected to the functioning flowmeter. An intake flow of 27.6 L/s was chosen regulating the mechanical gate at the end of the flume until a flow depth of 0.36 m is reached (Figure 43).



Figure 43 - Flowmeter (Left); Adjustable Mechanical gate (Right).

To create the velocity profiles, the flow velocity was measured in 10% intervals of the total water depth ($d = 0.36$ m). The ADV was placed 2 meters upstream of the first sand box. The value used in the velocity profiles is the average of 10 velocity values with standard deviation below 0.05 m/s and a SNR(dB) higher than 15 taken for each 10% interval. However, this equipment only operates when submerged and measures the velocity of the point 0.05 m below its extremity. For that reason, it was not possible to measure the 0.9D interval being $d = 0.31$ m ($\sim 0.86D$) the last interval measured.

To collect data, the ADV is connected to the data acquisition system *VectrinoPlus*. The collected data from the initial three velocity profiles was compiled in Table 12. The velocity profiles can be better analyzed by plotting each water depth with the corresponding flow velocity (Figure 44 to Figure 46).

Table 12 - Average velocity values collected from VectrinoPlus in cm/s.

Depth	0.1D	0.2D	0.3D	0.4D	0.5D	0.6D	0.7D	0.8D	0.86D
1st Profile	5.75	6.26	6.64	6.80	6.70	7.10	7.28	7.07	7.43
2nd Profile	5.33	5.82	6.24	6.74	6.75	7.08	7.35	7.53	6.68
3rd Profile	5.11	6.47	6.30	6.79	6.88	7.14	7.17	7.22	7.23

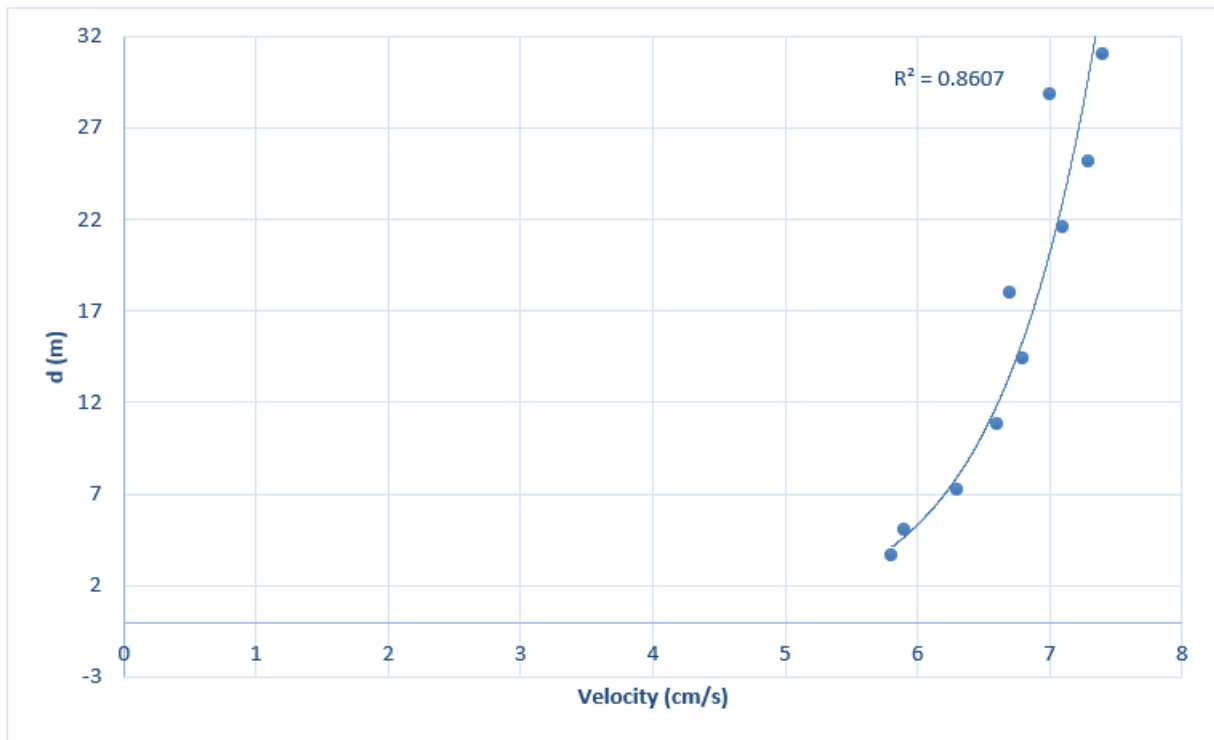


Figure 44 – 1st velocity profile.

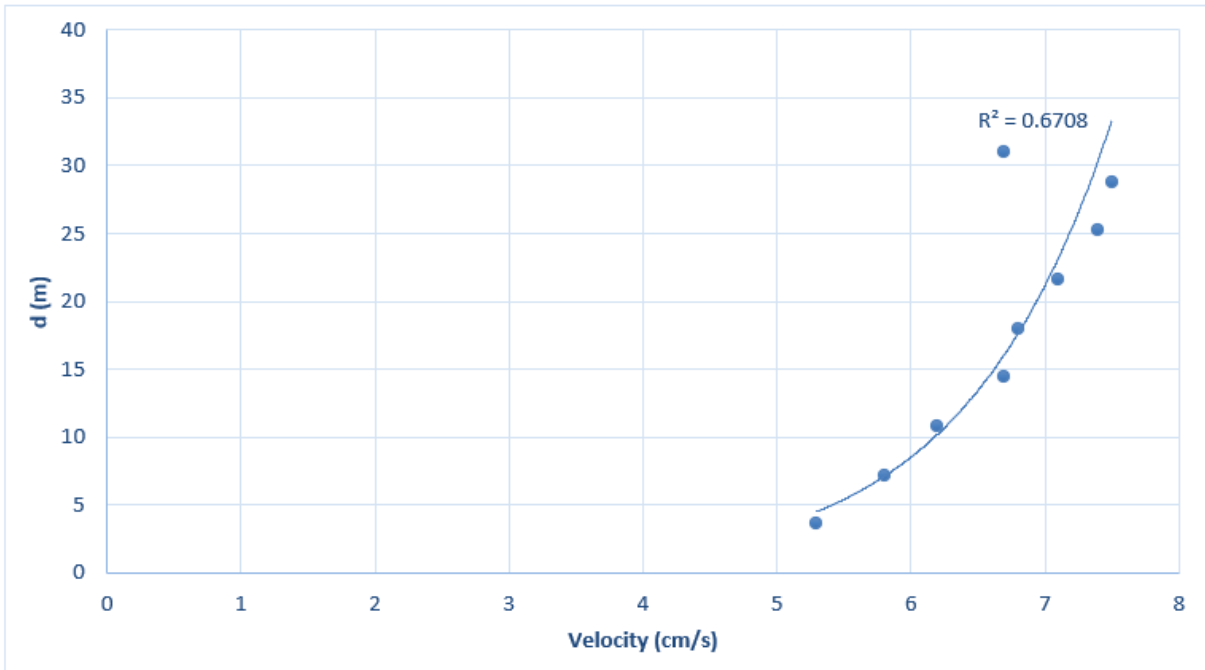


Figure 45 – 2nd velocity profile.

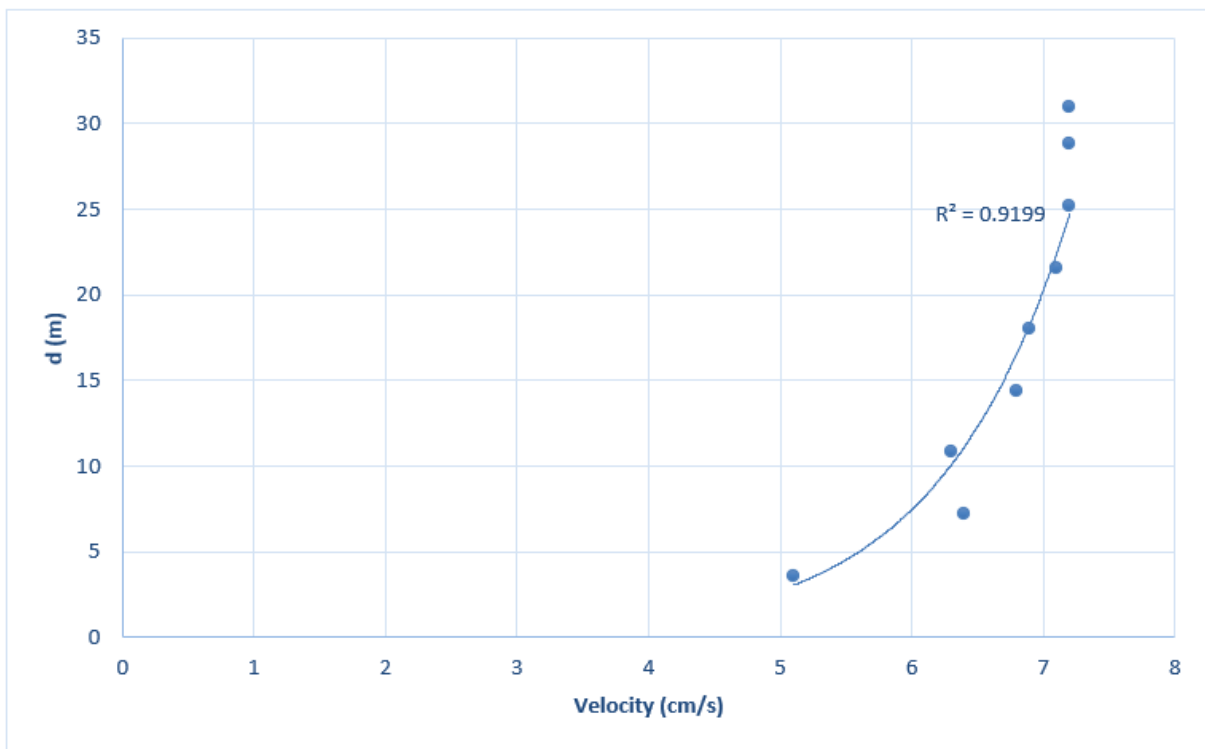


Figure 46 – 3rd velocity profile.

As previously discussed, the current velocity profiles tend to follow the exponential function. By analyzing the trendlines of the 3 initial velocity profiles, it can be observed that the exponential trendline does not fit the 2nd Velocity Profile ($R^2 = 0.6708$). This low value of correlation can be explained by a high degree of variability in the collected data for water depths in the interval of $[0.6D-0.86D]$. Some

potential explanations for this uncertainty include the possibility of an ADV malfunction, or a possible temporary increase in flow turbulence due to external elements and proximity to the surface.

During the initial preparation for the experimental tests, it was observed significant water loss in the flume. The flume losses can be estimated using the continuity equation. As can be seen in Figure 43, the flowmeter indicates a flow of 27.6 L/s, and using the continuity equation, a mean velocity of 7.66 cm/s was expected. However, the average of the 3 observed mean velocity values, corresponding to the 0.4D values in Table 12, was 6.78cm/s which is a value expected if the flowmeter indicated a flow of 24.4 L/s. It can be concluded that for a water level of 0.36m the flume presents flow losses of around 3.2 L/s.

The flume presented a high degree of wave reflection which would lead to distortion and misrepresentations of the test conditions and ultimately cause the abrupt stoppage of the wave paddle by activating the safety trigger. To reduce the reflection effects in the physical model, a dissipation system was installed at the end of the flume near the mechanical gate. This dissipation system created a limitation on the maximum flow velocity for a water depth of d of 0.36 m. An in-depth description and wave reflection analysis can be found in the subchapter 4.1.3.2. The maximum flow velocity for a water depth of 0.36 m was reached when both intake pipelines were completely open.

In accordance with the Soulsby (1997) method, for the critical threshold for the depth average current speed, a velocity of $U_c = 0.27$ m/s was the ideal value to reach the target flow conditions of a near live bed condition. Lastly, a final velocity profile was assessed for the hydrodynamic conditions used for the experimental tests. Both intake pipelines were open to their full capacity, and a water depth d of 0.36 m was maintained. The average velocity collected from *VectrinoPlus* for each 10% interval is compiled in Table 13.

The 4^o velocity profile shown in figure 47, confirms a good relation to the fitted exponential curve with a $R^2=0.8104$. Ideally, three velocity profiles should be taken for a more precise assessment of the flow conditions. However, due to time limitations only one velocity profile was taken for the final experimental conditions.

Table 13 - Average velocity collected from VectrinoPlus in cm/s (4th Profile).

Depth	0.1D	0.2D	0.3D	0.4D	0.5D	0.6D	0.7D	0.8D	0.86D
4th Profile	15.061	16.624	17.6	17.225	17.821	17.32	17.919	18.365	18.171

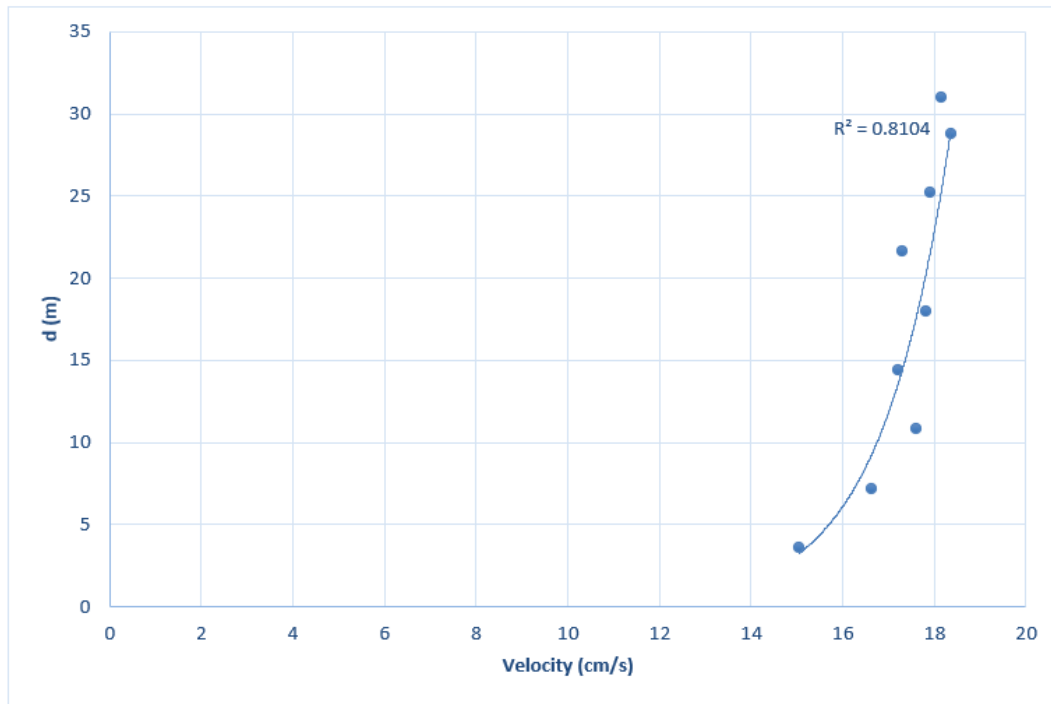


Figure 47 – 4th velocity profile.

Generally, flow velocity measurements should be performed upstream of the study area for each test. And ideally an ADV device should be placed at the upstream side of the first sand box and another one upstream of the second sand box. However, due to logistics limitations caused by ADV malfunctions, flow velocity measurements were not performed during the tests.

4.1.2 Wave dissipation system

As discussed, the wave and current flume at FEUP hydraulic laboratory presents high degree of wave reflection. The wave reflection would lead to distortions and misrepresentations of the test conditions and ultimately the activation of the safety trigger of the wave paddle. When the wave paddle was installed, a short sample tests were performed with random wave heights, periods, and water depths. As the generated waves reached the downstream gate, they were heavily reflected (Chambel, 2019). In order to perform longer and undistorted tests, a dissipation system was designed.

The solution encountered for the design of the dissipation system, was the deployment of anti-reflection boxes recreated from the works of Fraga (2017). The structure consists in 2 consecutive metallic anti-reflection boxes of 15 mm thick stainless steel with dimensions of 1.03 m long, 0.80 m wide and 0.70 m high. Inside the boxes, distended metal sheets were placed. According to Fraga (2017), the metal sheets should be placed with decreasing spacing and openings from each other from upstream to downstream. In the upstream box, the 5 distended metal sheets were placed using plastic bracelets, while in the downstream box, 7 distended metal sheets were used, as shown in Figure 48. The metal sheets were placed with an arbitrary decreasing spacing and opening from upstream to downstream. However, a correct recreation of the works of Fraga (2017), requires a node and antinode wave analysis, depending on the wave length, for a correct placing of the metal sheets.



Figure 48 - Upstream box (left); and downstream box (right).

The boxes were placed inside the flume in the downstream of both sediment boxes, at 2 m from the mechanical gate. Since the flume is 1 m wide while the dissipation boxes only had 0.80 m of width, the system had to be fixed to prevent their displacement during the tests by using non-intrusive wooden blocks, on each side of the box to complete the missing width (Figure 49). Furthermore, a gravel profile was then created. A plastic sheet and wooden plaques were placed in the downstream face of the dissipation system to prevent the gravel from escaping through the available spaces. The gravel profile created inside the anti-reflection boxes (Figure 50) has an initial 1 meter section with a 8% slope and a second flat section.



Figure 49 - Dissipation system fixed to the flume.

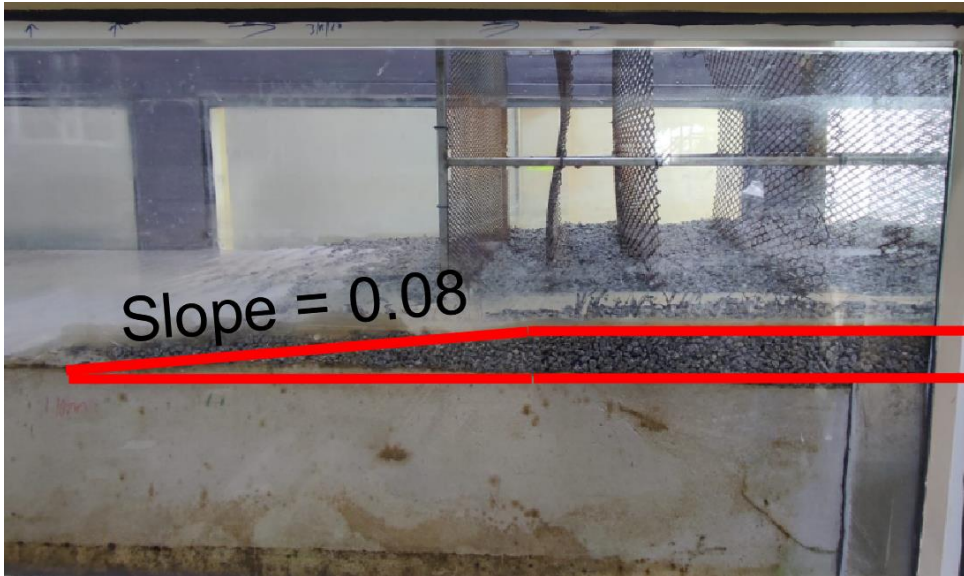


Figure 50 - Gravel profile.

4.1.3 Wave analysis tool

With the dissipation system already in place, a wave reflection analysis was conducted in order to reach the closest conditions to the target conditions demonstrated in subchapter 3.4. The wave reflection analysis tool calculates the incident and reflected wave spectral energy, and the reflection coefficient at frequencies inside the valid frequency range using the measurements of water surface elevations of 4 wave probes. It also computes the bulk reflection coefficient, which is the average of the reflection coefficients with the ratio of the total reflected and incident energies.

To be able to analyze the model reflection, the reflection analysis tool frequency range should cover the range of $0.5f_p$ to $2f_p$ of the target conditions (see Table 14). By introducing the water depth and adjusting the wave probes distances in the wave analysis tool until the smoothest denominator graph, a valid frequency range was reached as given in Figure 51.

Table 14 - Target frequency ranges.

Target T_p , model	Target f_p	$0.5f_p$	$2f_p$
1.70 s	0.588 s^{-1}	0.294 s^{-1}	1.176 s^{-1}

As can be seen in the Table 14, the range of $0.5f_p$ to $2f_p$ was fully covered by the minimum and maximum frequency values, as demonstrated in Figure 51. The wave probe spacing in Figure 51 represents the ideal distance between each probe and the position of the wave probe 1.

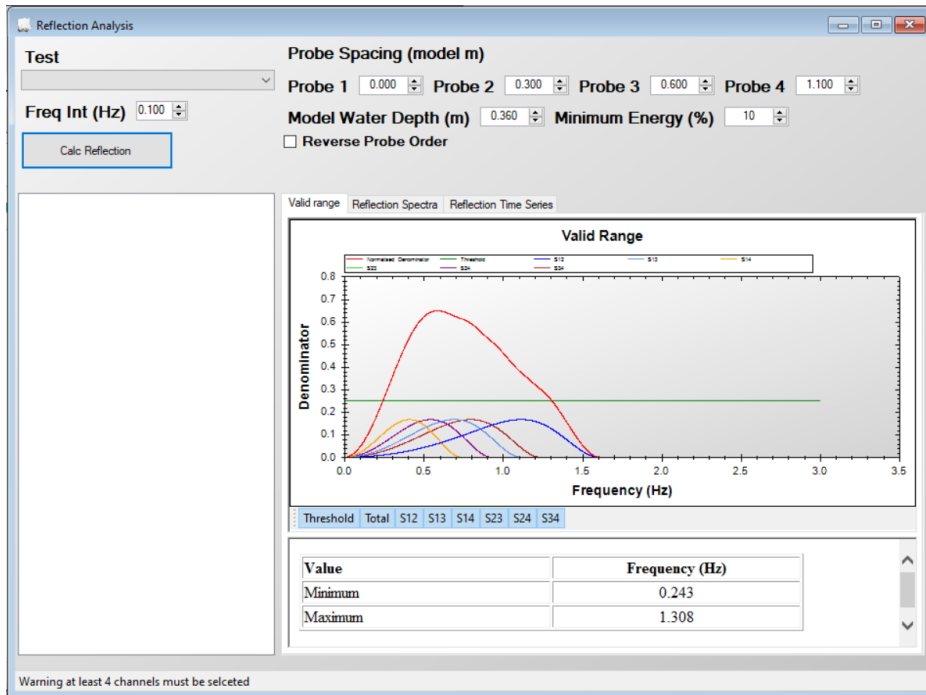


Figure 51 - Wave analysis tool

4.1.3.1 Wave probe calibration

The wave probes were then placed with correct spacing supported by the flume walls using tripods as shown in Figure 52. The wave probes were connected to the acquisition board of the data acquisition system HR DAQ. The data acquisition system received, converted, and allowed the collection of all measurements sent by the probes. In order to cover the range of expected water surface elevation the wave probes were calibrated each day or whenever the water level changed.

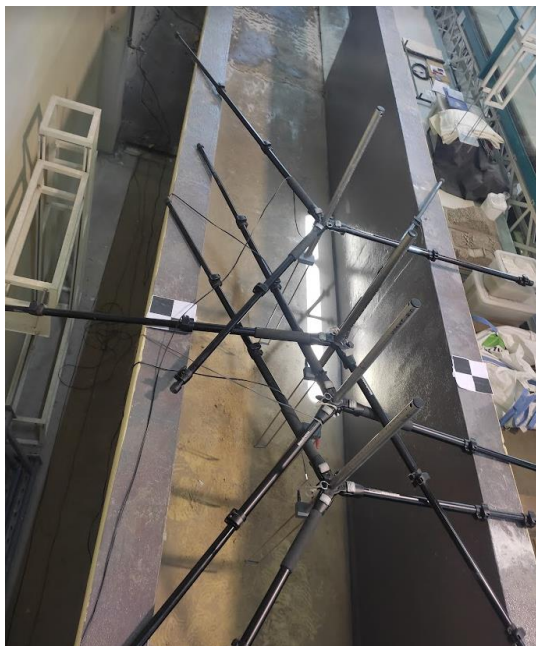


Figure 52 - Reflection analysis probe spacing.

Firstly, the flume was filled with the desirable water depth and the wave probe calibration started with a creation of a new calibration series in HR DAQ (Figure 54). Then, 3 water levels associated with each probe were defined by adjusting the immersion of each probe to capture the full voltage that the system can capture.

The first level (level 0) is the reference level, corresponding to the mean water level. To calibrate the level 0, the wave probe was placed in the center of the potential “wetted” difference of the probe range. Secondly, the level -, correspondent to the minimum water surface that the wave probe can capture, was calibrated by raising the wave probe until the minimum level of potential “wetted” difference of the probe range. Finally, the level +, correspondent to the largest wave height that can be captured by the probe, was calibrated by lowering the wave rod until the maximum level of the potential “wetted” difference of the probe range. The potential “wetted” difference of the wave probe had a length of 0.24 m. The level 0 was defined with the value 0, the level - with value -0.12 m, since it corresponds to water surface levels below the mean water level, and the level + with value +0.12 m, since it corresponds to water surface levels higher than the mean water level. After the introduction of this calibration in HR DAQ, a linear regression was created for each probe to assign a water surface level with each different voltage, as shown in Figure 53.

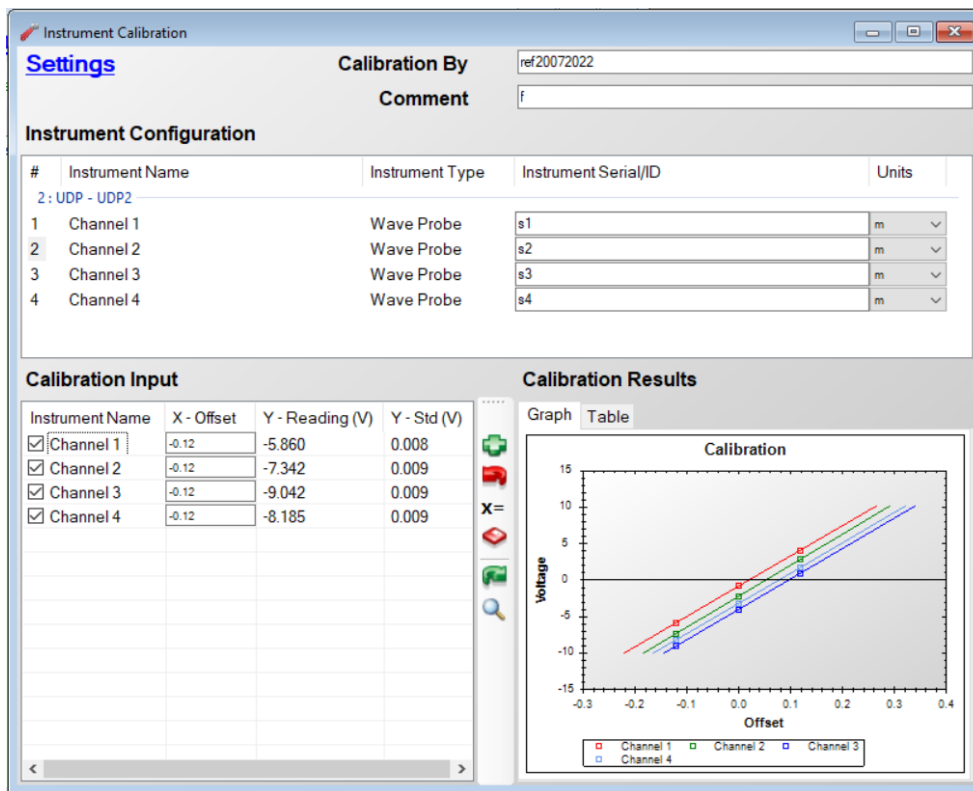


Figure 53 - Wave calibration series (HR DAQ).

4.1.3.2 Reflection analysis

Once the wave probe calibration was done, the reflection analysis was performed before the introduction of the foundation models. An initial 6 preliminary wave tests for the target conditions were conducted. As it can be seen in Table 15, the significant wave heights were too low for the current target conditions. In order to reach higher wave heights, the gain factor should be increased. However, the wave paddle safety trigger was activated for gain factors higher than 1.10, stopping the wave paddle and not allowing the full 1000 waves to be created.

Table 15 - Initial wave tests features.

Test number	Hs(m)	Tp,model(s)	Duration(s)	N° waves	Gain factor	Wavemaker failure	Average Hm0 (m)
1	0.11	1.7	1700	1000	1.00	no	0.530
2	0.11	1.7	220	129	1.20	yes	-
3	0.11	1.7	420	247	1.15	yes	-
4	0.11	1.7	1700	1000	1.10	no	0.570
5	0.11	1.7	1140	671	1.10	yes	-
6	0.11	1.7	1620	953	1.05	yes	-

According to Frostick et al. (2011), the reflection coefficient is recommended to be below 15%, and if possible under 10%. The reflection analysis revealed that the reflection coefficient of the test number 4 was near the 15% benchmark for durations corresponding to a wave number of 1000 waves (Table 16). The reflection analysis was made with a spectral threshold of 1%, eliminating the 1% extreme frequencies, and for the two recommended frequency bands of $\frac{1}{15}f_p$ and $\frac{1}{20}f_p$. These results were then confirmed and compared with total wave height reflection coefficient (Table 16). The wave height reflection coefficient was computed using the help of a programmed Excel sheet, where the input is the table of (Frequency, Incident Spectra, Reflected Spectra, Reflection Coefficient) from the reflection analysis tool.

Table 16 - Reflection coefficients of test 4 ($T_{p,model} = 1.7$ s).

Test number	Bulk spectral reflection coefficient		Reflection coefficient (Hi/Hr)	
	$\frac{1}{15}f_p=0.04$	$\frac{1}{20}f_p=0.03$	$\frac{1}{15}f_p=0.04$	$\frac{1}{20}f_p=0.03$
4	16.3%	16.6%	16.5%	16.8%

Nevertheless, to increase the significant wave height, a second set of wave conditions was tested. This time, the wave period decreased to 10s ($T_{p,model} = 1.41$ s). A new wave probe spacing was needed, since the wave period and frequency exceeded the initial maximum frequency range in figure 51. The reflection analysis was remade for the new peak frequency range of $0.5f_p$ to $2f_p$ presented in Table 17. The wave probes were then reorganized according to Figure 54.

Table 17 - 2^o target frequency range.

Target $T_{p,model}$	Target f_p	$0.5f_p$	$2f_p$
1.41s	$0.709 s^{-1}$	$0.354 s^{-1}$	$1.418 s^{-1}$

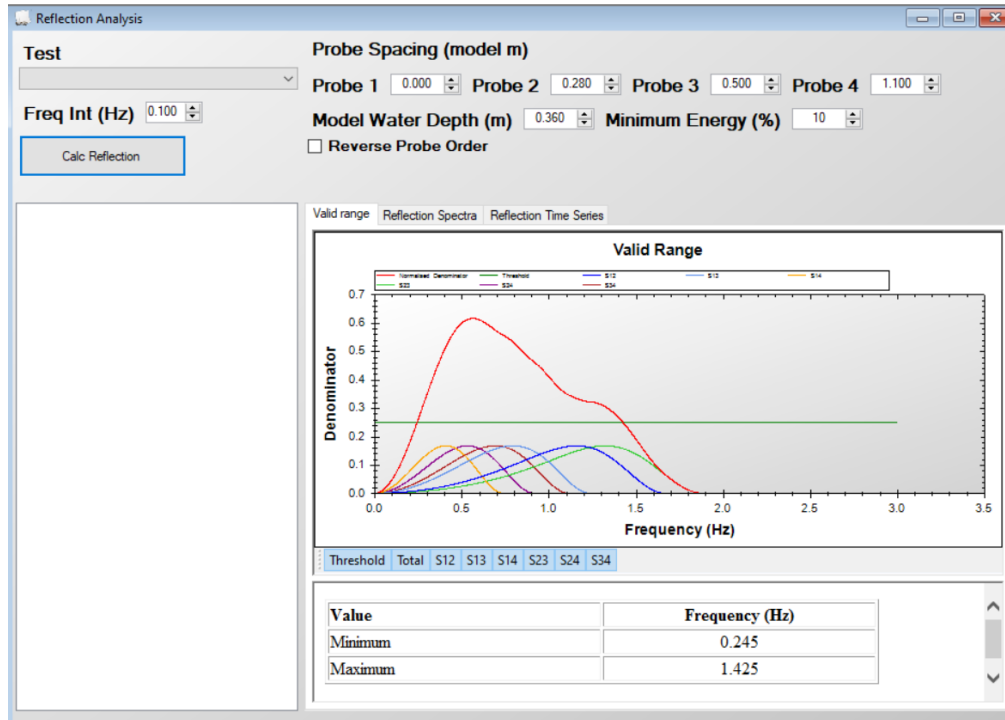


Figure 54 - New wave probe spacing.

For the new wave period, the following 3 wave tests were conducted and respective features are given in Table 18. The test 7 was made for a $H_{s,model} = 0.10$ m and a gain factor of 1.5, however the average $Hm0$ was considerable low. Finally, the tests 8 and 9 were made for $H_{s,model} = 0.11$ m and gain factors of 1.425 and 1.4, respectively.

Table 18 - Wave tests for $T_{p,model} = 1.41$ s.

Test number	$H_s(m)$	$T_{p,model}(s)$	Duration(s)	N ^o waves	Gain factor	Wavemaker failure	Average $Hm0$ (m)
7	0.10	1.41	1410	1000	1.5	no	0.89
8	0.11	1.41	1150	816	1.425	yes	-
9	0.11	1.41	1410	1000	1.4	No	0.95

A similar wave reflection analysis performed for test 4 was conducted for test 9 (see Table 19), with the bulk spectral reflection coefficient from the wave reflection analysis tool and the total wave energy reflection coefficient from the programmed Excel sheet.

Table 19 - Reflection coefficient values for test 9 ($T_{p,model} = 1.41$ s).

Test number	Bulk spectral reflection coefficient		Reflection coefficient (Hi/Hr)	
	$\frac{1}{15} f_p=0.047$	$\frac{1}{20} f_p=0.035$	$\frac{1}{15} f_p=0.047$	$\frac{1}{20} f_p=0.035$
9	19.2%	19.5%	19.3%	19.7%

Although the wave conditions tested in test 4 had significantly smaller reflection coefficients, in the current study higher values of significant wave height were prioritized over the smaller reflection coefficient. While comparing the two variables of the 2 wave conditions, the wave conditions of test 9 had a 17% increase in reflection coefficient and an increase of 67% of considerable wave heights.

As referred to before, the optimal reflection coefficient should not be higher than 15%, and preferably lower than 10% (Frostick et al., 2011). Ideally, further adaptations should be performed to the wave and current flume in order to decrease the reflection experienced. A possible flume adaptation is the use of floating cork bottle caps in combination with the existing dissipation system described in subchapter 4.1.2. Unfortunately, due to time limitations for the experimental stage of this dissertation, it was decided to perform the experimental work for the test number 9 wave conditions. The high reflection should be taken into consideration while analyzing the results of the experimental tests. More in-depth research on the flume reflection should be performed before planning future works.

4.2 New target conditions

After the calibration of the wave and current conditions, a new set of achievable hydrodynamic conditions were chosen. The final target conditions used for the physical model are presented in Table 20. Note that some significant shortcomings in both depth average current speed and reflection coefficient values could not be fixed due to the time limitations.

Table 20 - New target conditions.

	D(m)	Hs(m)	Tp(s)	Uc(m/s)	Um(m/s)	Gain factor
Prototype conditions	18	5.5	10	0.471	0.977	1.4
Model conditions	0.36	0.11	1.41	0.172	0.138	1.4

Due to the inability of scaling the sediment size, the depth average current speed was not the result of a direct Froude scaling. It was instead a direct calculation of the critical depth average current speed for the scaled water depth $d = 0.36$ m. However due to physical limitations detailed in subchapter 4.1.1 the maximum U_c reached in the model fell short of the 0.277 m/s calculated.

4.3 Laboratory tests

In this subchapter, can be found an extensive description of all the steps in the physical model assembly in chronological order. There is also provided a brief explanation about the use of digital terrain model with the help of a laser scan device. For each test performed the following steps were conducted:

- smoothing of the surface of both sand boxes;
- perform the initial 3 laser scans;
- positioning 3 wave probes within the flume;
- slow filling of the flume until reaching the desired water depth;
- perform the wave probe calibration;
- conduct 3 wave trains of 1000 waves each;
- slow emptying of the flume until the sand boxes surface are completely dry;
- remove the wave probes; and
- perform the final 3 laser scans.

4.3.1 Test plan

The test plan consists of an initial scour test for both foundation models, followed by 3 scour tests with the introduction of the WEC model, positioned upstream of the foundation in consecutively larger distances $d = [0.15 \text{ m}; 0.25 \text{ m}; 0.35 \text{ m}]$, as shown in Figure 55 and Figure 56. Furthermore, a second set of tests were performed with the same disposition; however, this time a 1.5 cm layer of coarser sand was added on top of the fine sand layer exemplified in Figure 57 and Figure 58. The corresponding test plan can be found in Table 21. Each test comprised both sand boxes with the same conditions, the monopile tests were performed in the first sand box, whilst the GBF tests were considered in the second box. The GBF model was placed 4 cm below the soil surface and the WEC model was placed in order to align the top of its foundation with the soil surface.

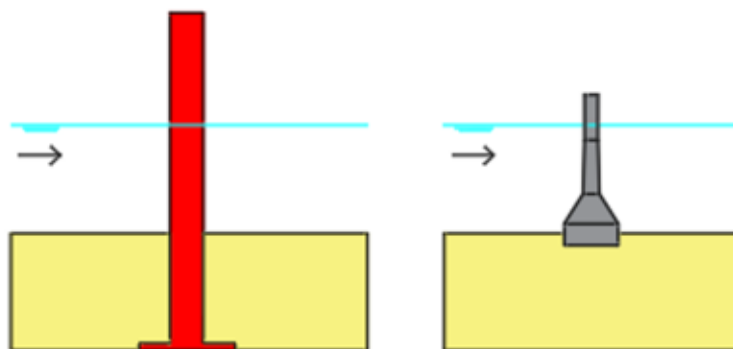


Figure 55 - Foundation only scour test disposition in fine sand.

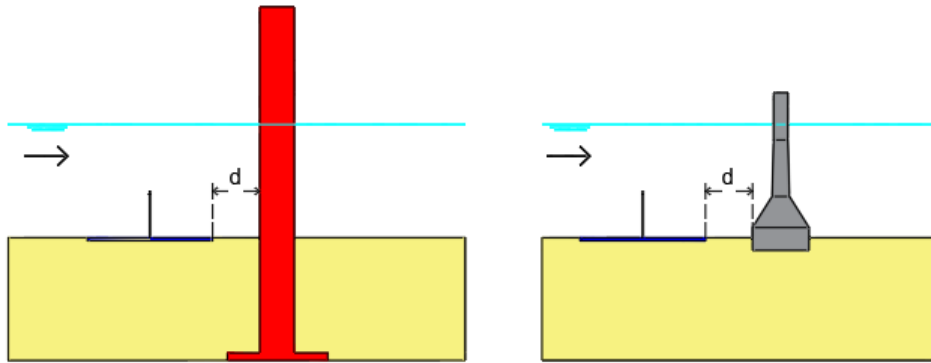


Figure 56 - Hybrid foundation scour tests disposition in fine sand.

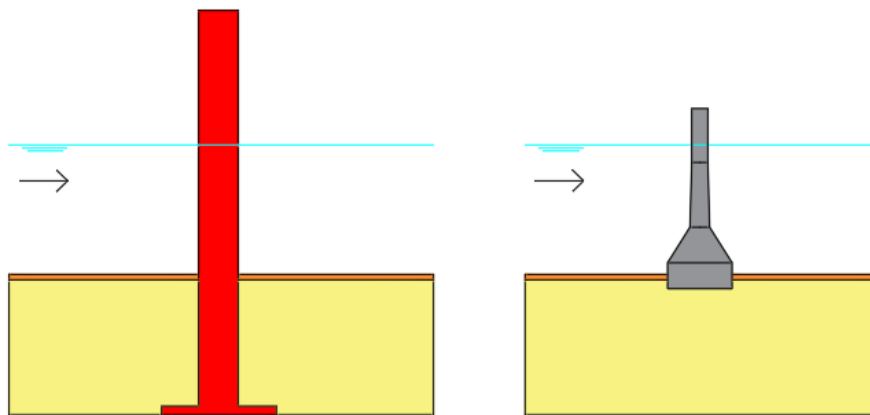


Figure 57 - Foundation only scour test disposition for layered soil.

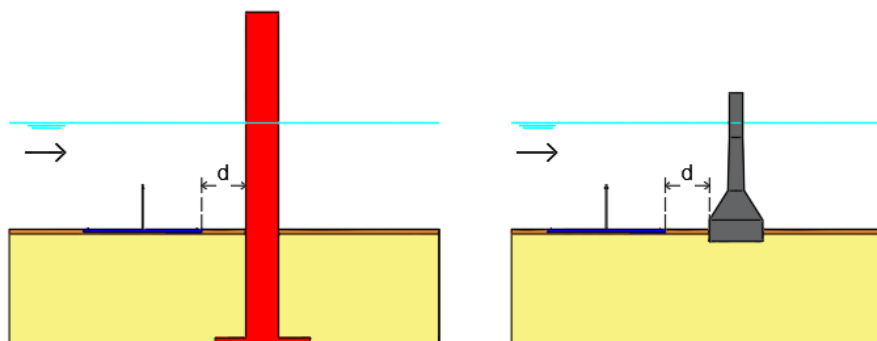


Figure 58 - Hybrid foundation scour tests disposition for layered soil.

Table 21 - Full test plan.

Test name	Test number	Foundation type	WEC distance	Soil type
Waves 1	1.1	Monopile	-	Fine sand
	1.2	GBF	-	Fine sand
WEC 1	2.1	Monopile	0.15 m	Fine sand
	2.2	GBF	0.15 m	Fine sand
WEC 2	3.1	Monopile	0.25 m	Fine sand
	3.2	GBF	0.25 m	Fine sand
WEC 3	4.1	Monopile	0.35 m	Fine sand
	4.2	GBF	0.35 m	Fine sand
Waves 2	5.1	Monopile	-	Layered sand
	5.2	GBF	-	Layered sand
WEC 4	6.1	Monopile	0.15 m	Layered sand
	6.2	GBF	0.15 m	Layered sand
WEC 5	7.1	Monopile	0.25 m	Layered sand
	7.2	GBF	0.25 m	Layered sand
WEC 6	8.1	Monopile	0.35 m	Layered sand
	8.2	GBF	0.35 m	Layered sand

4.3.2 Laser scans

For each test, 2 sets of 3 laser scans were performed, the first set before each test and the second after each test in order to compare the two bathymetries and assess the scour holes and scour development. The laser scans were performed by using the FARO laser scanner device (Figure 59), later processed and transformed into point clouds by the SCENE software. This process is extensively described in Taveira-Pinto (2021). First of all, a strategic planning and important consideration for possible adaptations to the laboratory setup was considered.



Figure 59 - FARO laser scanner.

Since it is not possible to create a full high-resolution scan with only one scan, for each set of laser scanning, 3 laser scans were performed from 3 different device placements. The first placement was in the upstream of the first sand box, whilst second placement was in the downstream of the first sand box and in the upstream of the second sand box. The third scanner placement was in the downstream section of the flume, between the dissipation system and the mechanical gate (Figure 60). This laser scanner placement was chosen to cover at least one scan upstream and one scan downstream of each sand box.

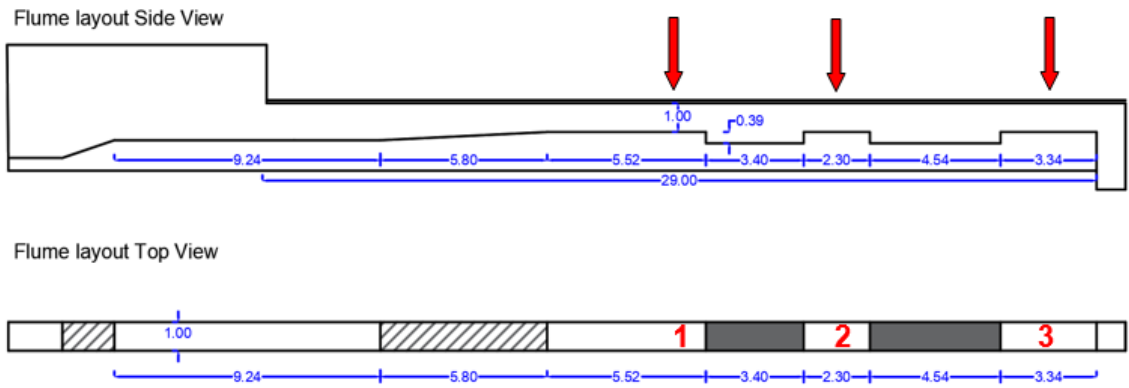


Figure 60 - Laser scan placement.

However, to merge the 6 initial and final laser scans and create a joint point cloud in the SCENE software, it is necessary to place artificial reference targets. In this setup, 13 checkerboards were considered: 3 vertical and 10 horizontal (Figure 62 to Figure 64). From the 3 vertical checkerboards, one was placed in the wavemaker machine while the other two were positioned in the upstream part of the flume near the mechanical gate. The 10 horizontal checkerboards were placed over the flume wall in 5 sets of 2, 2 in the approximation ramp, 2 in the upstream of the monopile foundation model, 2 in the downstream of the monopile foundation model, 2 in the upstream of the GBF model and 2 in the downstream of the GBF model. A checkerboard is a small figure of 2 black squares (Figure 61).



Figure 61 - Artificial reference (checkerboard).

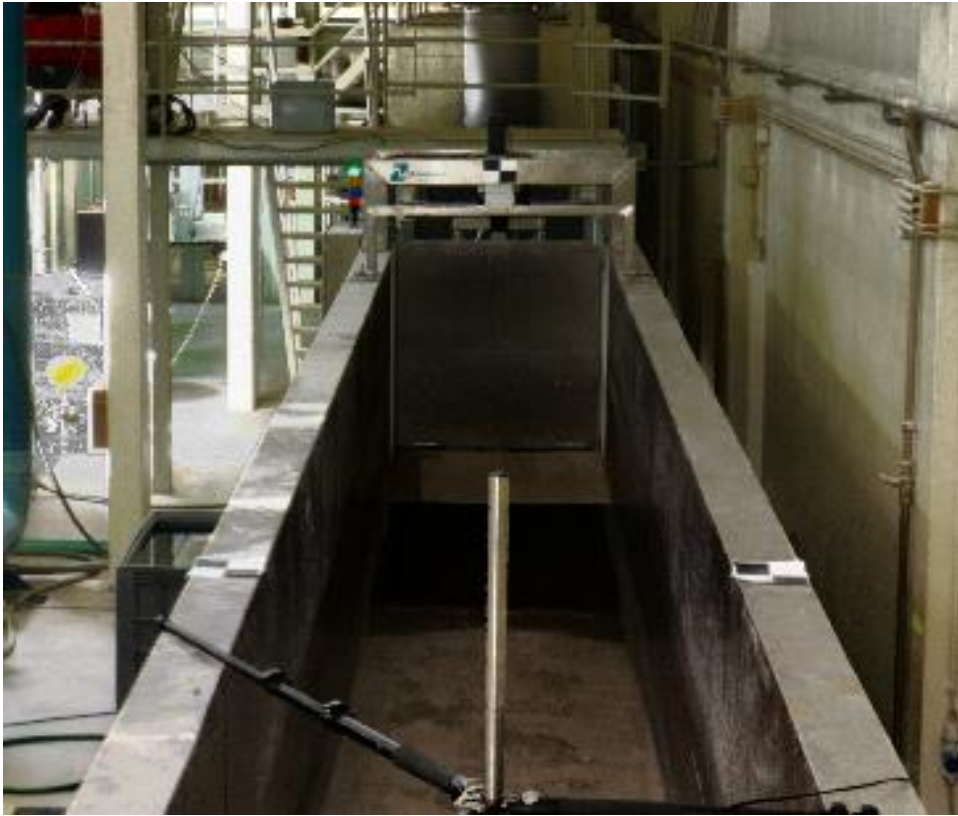


Figure 62 - Checkerboard placement 1.

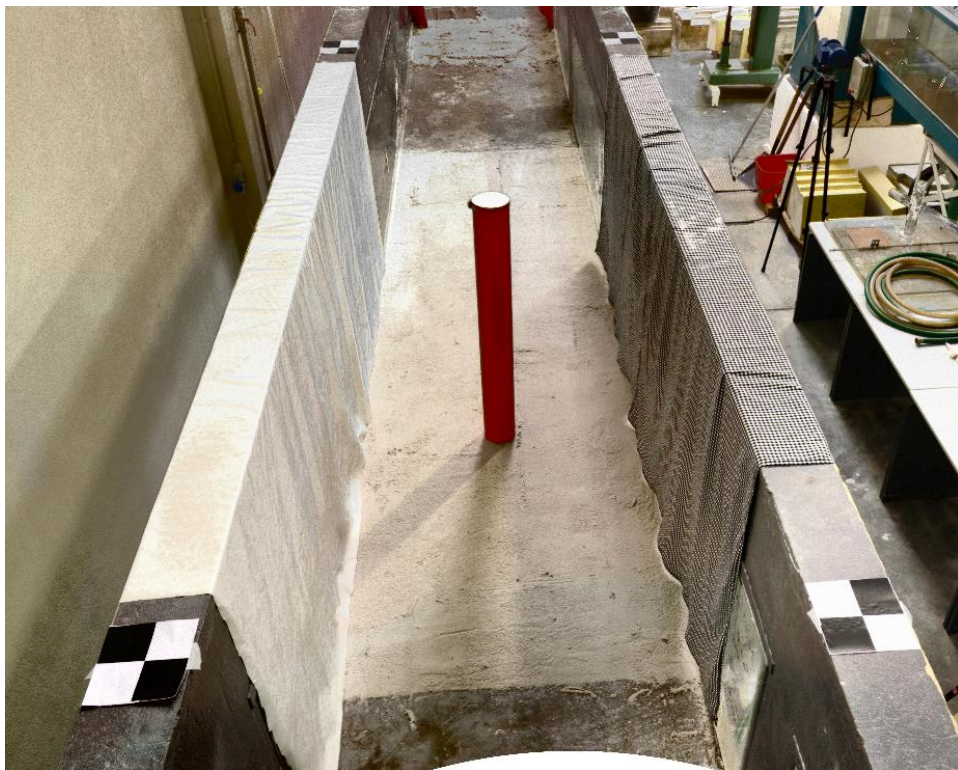


Figure 63 - Checkerboard placement 2.



Figure 64 -Checkerboard placement 3.

Furthermore, the FARO laser scan device does not present good performance in the presence of reflective surfaces. For that reason, it was necessary to cover the flume windows adjacent to the study areas with blankets, as shown in Figure 63 and Figure 64. Additionally, the transparent acrylic monopile model and the transparent acrylic base of the WEC model were completely painted. Note that the blankets near the study area of the GBF model covered the ideal place for the checkerboards, and for that reason the checkerboards had to be placed over the blankets. An initial preview was performed prior to each laser scan in order to ensure the visibility of all the checkerboards.

4.3.3 Faro SCENE software

Faro SCENE software is where the scans are processed, additionally this software can couple multiple scans from the same area. At the end of each test and after both sets of laser scans were finalized, the six scans were imported to the SCENE software where it was possible to process, merge the scans and ultimately create a Point Cloud (Figure 65). However, the SCENE software creates a Point Cloud for the entirety of the scan, therefore, the Point Cloud files created were too big to be analyzed. In an effort to decrease the file sizes, individual clipping boxes of the study area were isolated for each test (Figure 66). A more comprehensive explanation of the SCENE software can be found in Taveira-Pinto (2021).

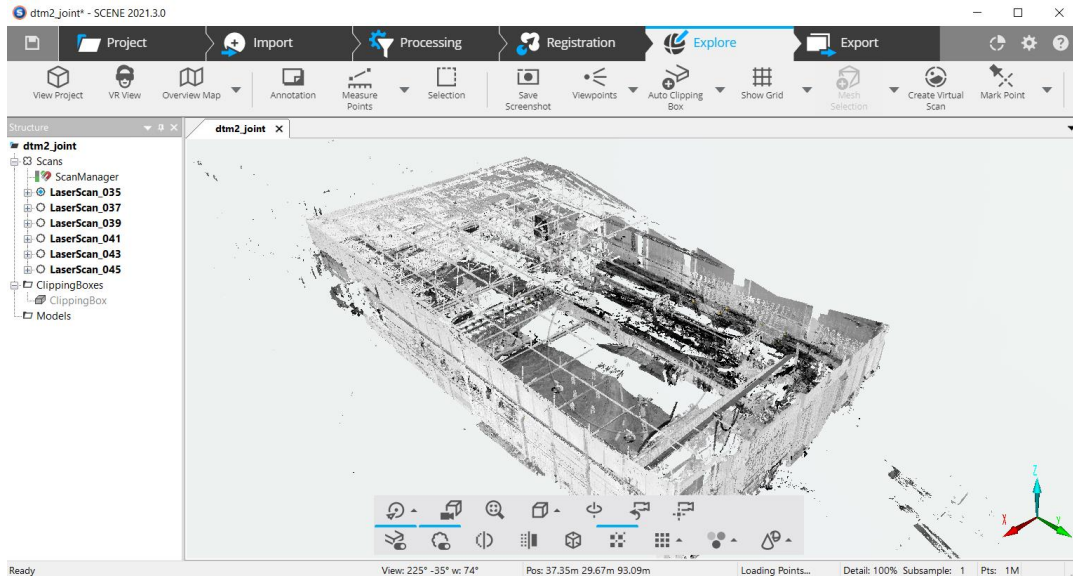


Figure 65 - Point cloud in the SCENE software.

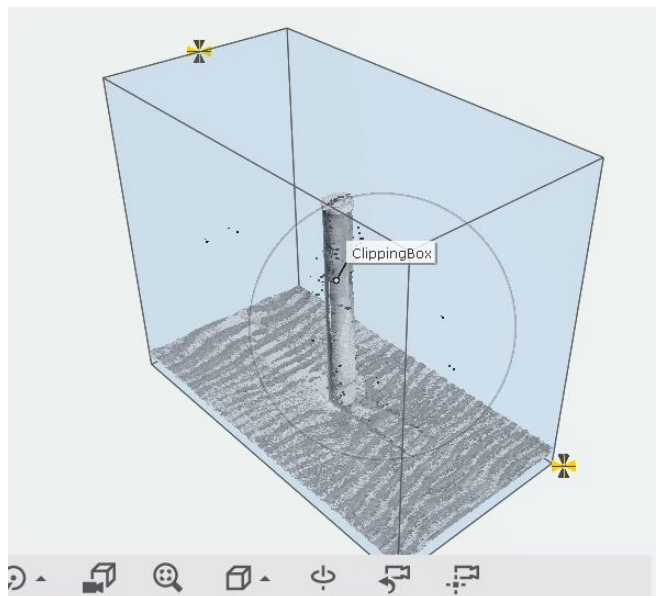


Figure 66 - Individual clipping boxes (SCENE software).

4.3.4 Point Cloud analysis

In order to analyze the point clouds created in the SCENE software, the clipping boxes created were exported and later imported into the CloudCompare software. CloudCompare is a 3D point cloud processing software capable of comparing two 3D point clouds.

The individual clipping boxes were then exported to LAS or ASCII XYZ files and later imported to CloudCompare in order to analyze the obtained scour hole. By using the cloud-to-cloud distances with the initial scan, it was possible to compare the initial and final bathymetries (Figure 67). The cloud-to-cloud distances tool allowed to split the distances in the XYZ axis.

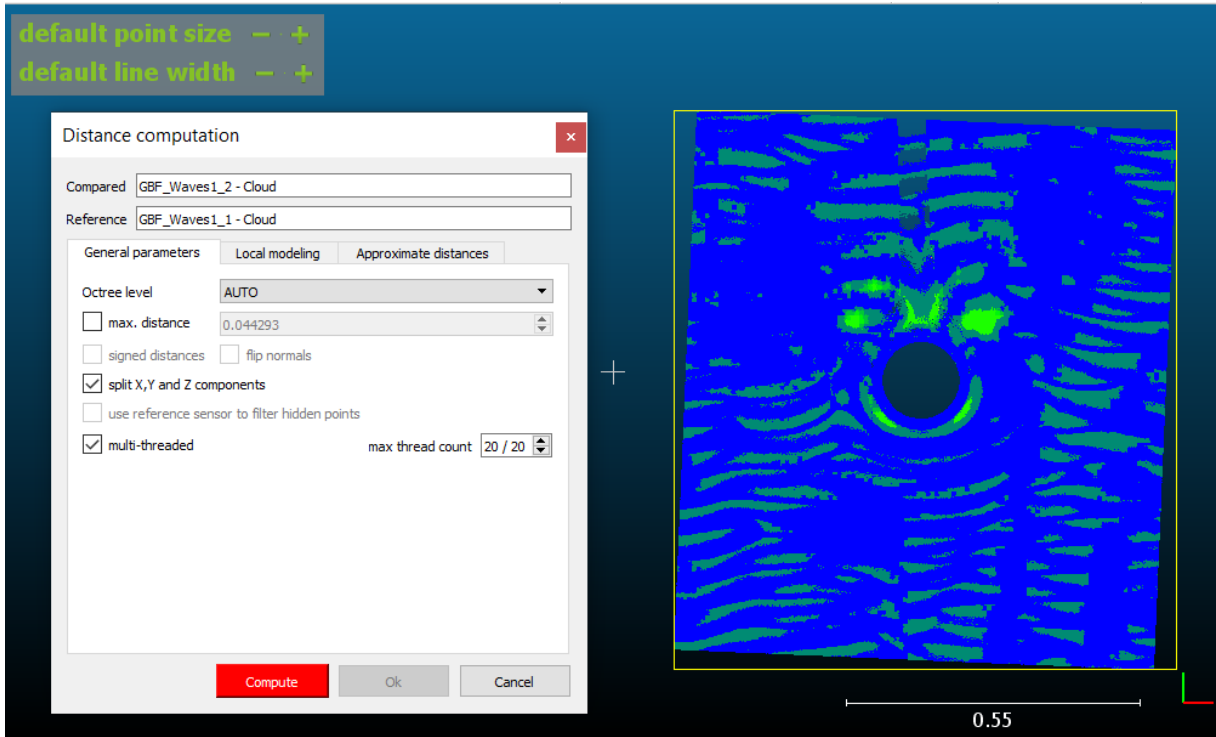


Figure 67 - Cloud to cloud distances tool from CloudCompare software.

After the cloud-to-cloud distances were computed, the distance cloud was analyzed and adjusted to facilitate the visualization of scour patterns and zones of deposition (Figure 68). The color scale saturation range was then adjusted in order to identify the deposition zones with color red and the scour zones with the color blue (Figure 69).

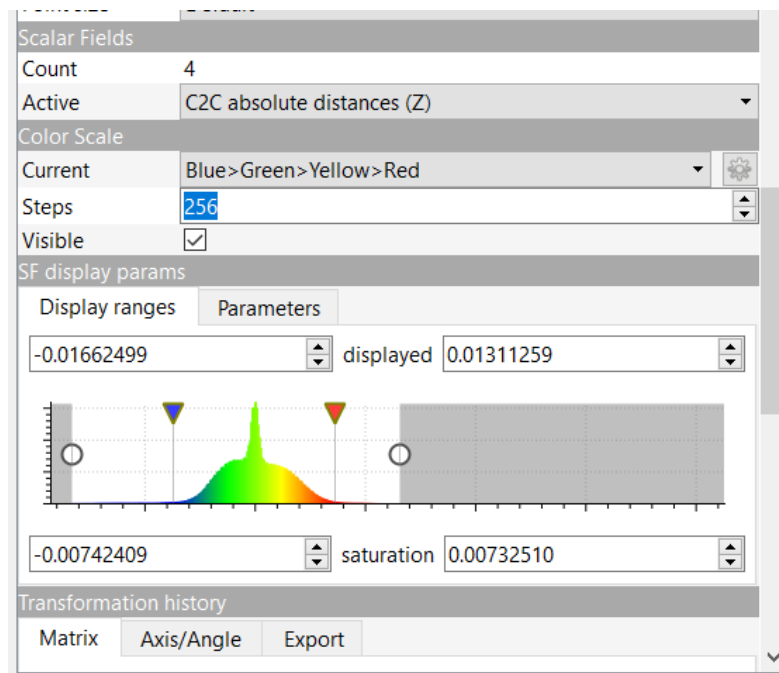


Figure 68 - CloudCompare color scale interface.

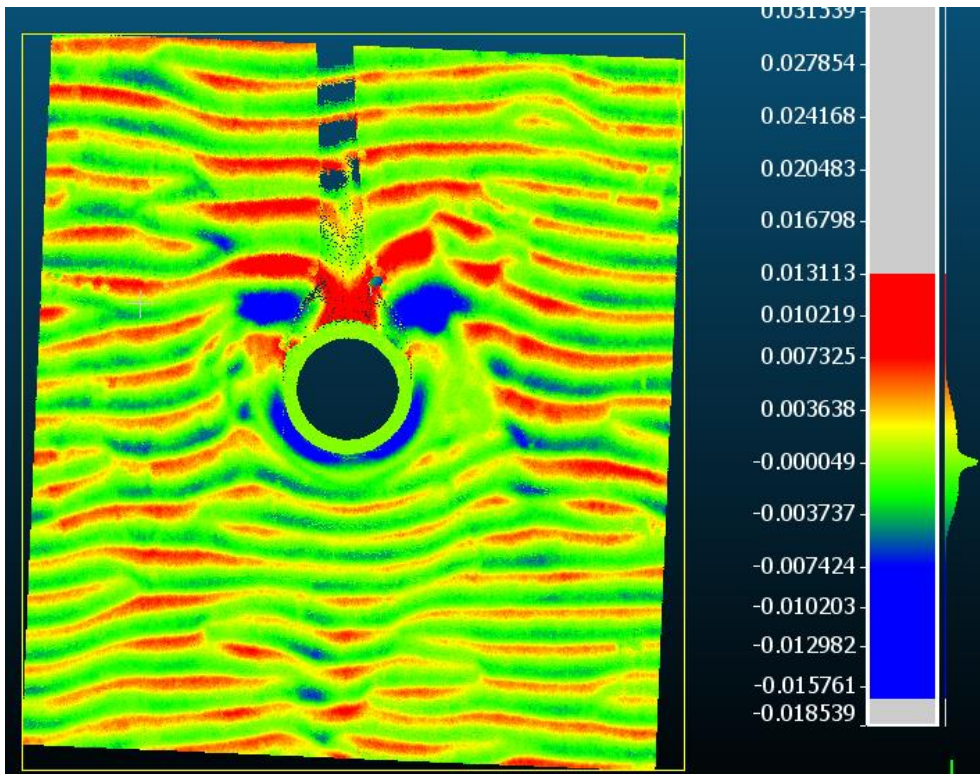


Figure 69 - Distance cloud from CloudCompare software.

As can be seen in Figure 69, the CloudCompare results reveal some holes in the distance cloud generated. These holes can be explained by some inadequacies in the original point cloud created from the laser scans. Floating point over both edges of the foundation models and shadows can be found in Figure 70 from the original SCENE point cloud.

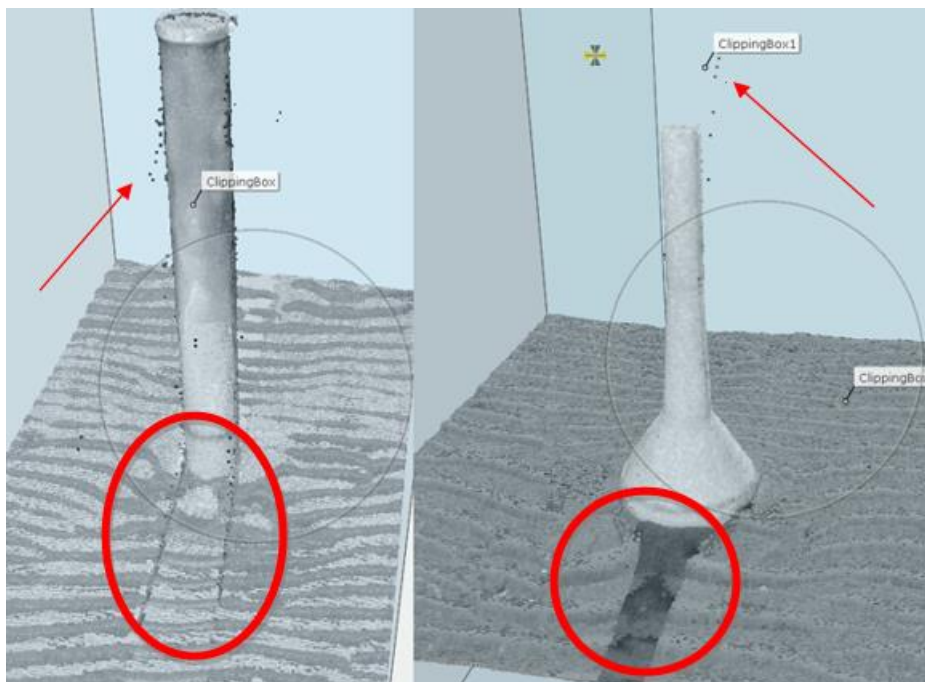


Figure 70 - Laser scan inadequacies.

The appearance of floating points can be explained by the positioning of the laser scan device. As referred in subchapter 4.3.2, due to the flume longitudinal disposition the laser scan strategy included 3 scanning positionings in the same axis, and as can be noted the floating points appear near of the parallel surfaces to the laser scan. In future works, to minimize these holes, an additional two laser scans in a different axis are recommended. One possible laser scan strategy for these 2 additional laser scan positioning is the placement of the laser scan device outside of the flume between the two sand boxes as shown in Figure 71.

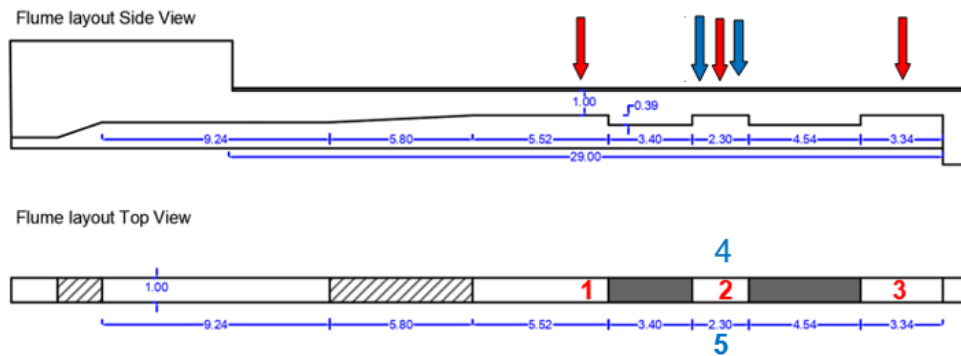


Figure 71 - New proposed laser scan placements.

4.3.5 Wave data acquisition

It is important to collect the wave data for each test, in order to confirm the target conditions. Possible deviations should be taken into account when analysing the test results. For that reason, before each test, three wave probes were positioned in a strategic way to individualize the wave data for each sand box. The wave calibration method is described in subchapter 4.1.3.1.

The first probe was positioned after the approach ramp and upstream of both sand boxes in an undisturbed zone to serve as a reference point for the other two wave probes. The second wave probe was positioned 0.50 m upstream of the first test area and the third wave probe was positioned 0.20 m upstream of the second test area as shown in Figure 72.



Figure 72 - Wave probe placement.

As described before in subchapter 4.1.3.1, the wave probes were connected to the acquisition board of the data acquisition system HR DAQ. The data acquisition system received, converted, and collected all the measurements sent by the probes. A data acquisition series was created for each test (Figure 73).

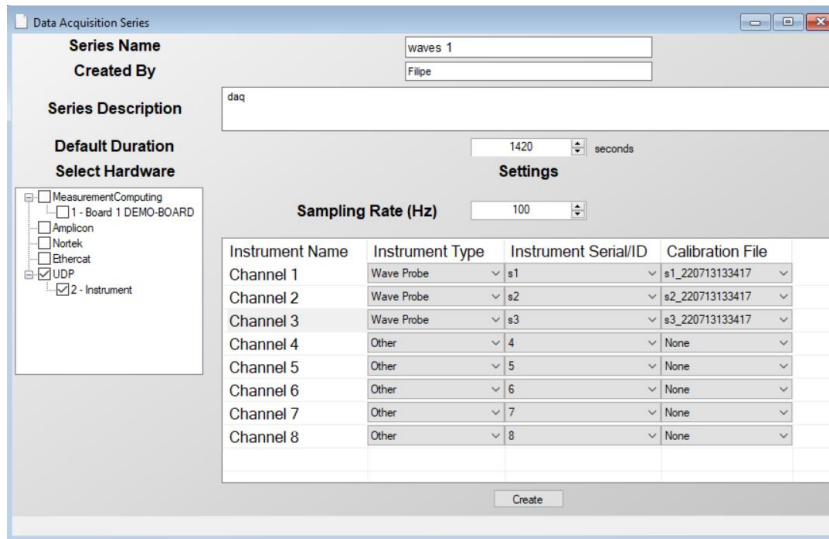


Figure 73 - Data acquisition series (HR DAQ).

As the peak period of the wave train was $T_p = 1.41$ s (Model period), the 1000 wave train had a duration of 1410 s. However, as the data acquisition test and wave maker series were initiated separately, a 10 second margin was given. After the wave data acquisition, the data collected was processed through the post-processing tool of HR DAQ.

The post-processing tool compiles the data collected. The output of this tool presents the information of the time series, global statistics, the zero-crossing analysis, and the spectral density analysis. In the current study, only the spectral density information was used and analysed.

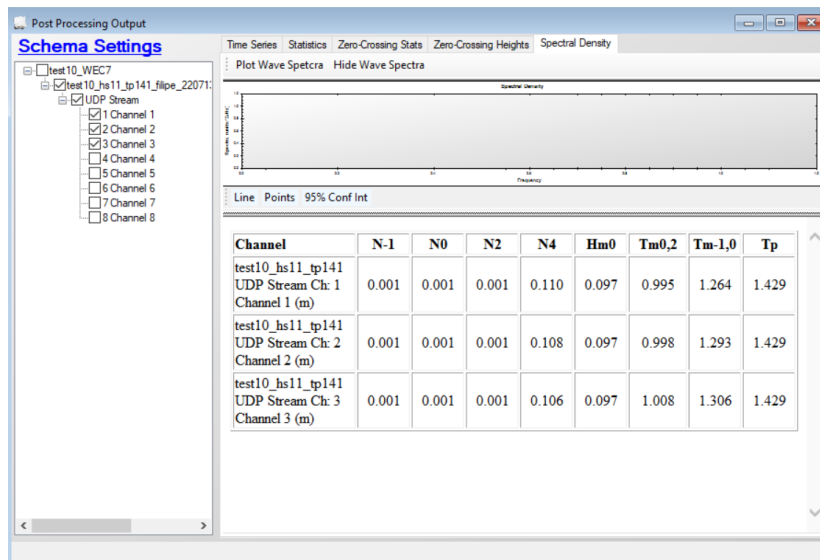


Figure 74 - Post-processing tool (HR DAQ).

4.3.6 Wavemaker software (HR Merlin)

The wavemaker was connected to the wave generator computer, which has the HR Merlin software. As referred before, in subchapter 3.1.1, HR Merlin is a wave generator software that controls the wavemaker and is capable of simulate a wide variety of irregular sea states. The current laboratory tests were performed using the JONSWAP time series.

The first step was introducing the project dimensions and wave spectra conditions as displayed in Figure 75. As for the project dimensions, the model dimensions were introduced with a water depth of 0.36 m and a tank depth of 1 m. In the wave spectra conditions, the JONSWAP (Hs) option was adopted in pair with the “Gamma” value of 3.3.

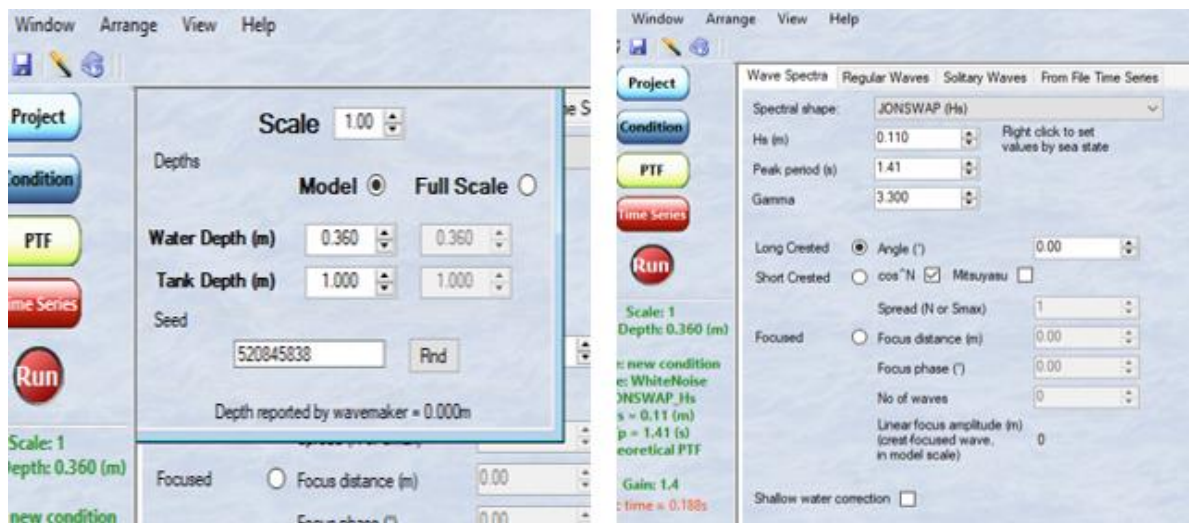


Figure 75 - HR Merlin test conditions: Project dimensions (left); wave spectra conditions (right).

Once the model dimensions and wave spectra parameters are introduced, it is necessary to choose the duration and gain factor of the test in order to create the Paddle time series (Figure 76). As shown in the subchapter 4.1.3.2, the ideal optimal gain factor for the conditions chosen was 1.4.

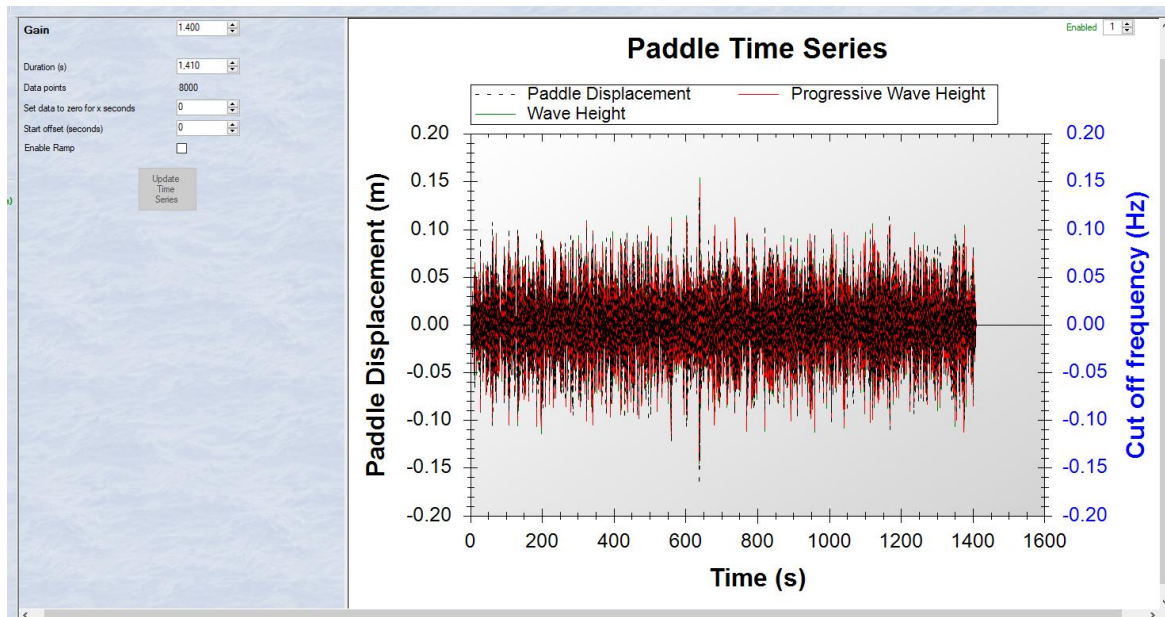


Figure 76 - Paddle time series (HR Merlin).

4.4 Results, Analysis, and discussion

The current subchapter performs an extensive exposition, analysis and further discussion about the results obtained in the set of tests performed. The data analyzed includes the wave data collected from the wave data acquisition, described in 4.3.5 and 4.3.6, and the scour data collected using the Laser Scanning process, detailed in 4.3.2, 4.3.3 and 4.3.4.

4.4.1 Wave data measured

As detailed in subchapter 4.3, the strategic placement of the wave probes allows to individualize the wave data collected in the two study areas, and an additional wave probe positioned in the upstream and undisturbed area. The wave data collected is compiled in Table 22.

For each test three wave trains were performed, meaning that for each test three wave data acquisition files were made. The $Hm0$ and Tp values, summarized in Table 22, are the average of the three wave data acquisition files. The Um values derive from the direct application of the method developed by Wiberg and Sherwood (2008) with the use of the coding software MATLAB.

Table 22 - Wave data collected.

Test Name	Hm (m)			Tp (s)			Um (m/s)		
	Wave Probe 1	Wave Probe 2	Wave Probe 3	Wave Probe 1	Wave Probe 2	Wave Probe 3	Wave Probe 1	Wave Probe 2	Wave Probe 3
Waves1	0.098	0.102	0.095	1.389	1.433	1.404	0.122	0.130	0.119
WEC1	0.095	0.095	0.096	1.389	1.449	1.316	0.118	0.122	0.124
WEC2	0.095	0.096	0.094	1.389	1.404	1.316	0.118	0.12	0.111
WEC3	0.093	0.094	0.093	1.389	1.452	1.316	0.115	0.121	0.111
Waves2	0.092	0.090	0.092	1.340	1.429	1.316	0.111	0.114	0.109
WEC4	0.096	0.097	0.096	1.389	1.464	1.316	0.119	0.125	0.114
WEC5	0.088	0.088	0.088	1.416	1.409	1.354	0.111	0.11	0.107
WEC6	0.097	0.098	0.098	1.402	1.471	1.458	0.121	0.127	0.126

As can be seen in Figure 77, the $Hm0$ variation line chart reveal that the wave height target was not reached. As previously analysed the reflection analysis, such difference was already expected due to the high values of reflection experienced in the flume. A possible explanation for this discrepancy between

the target wave height and measured H_{m0} , is that the wave height measured by the wave probes is the result of the difference between the incident wave height, H_{si} and the reflected wave height, H_{sr} .

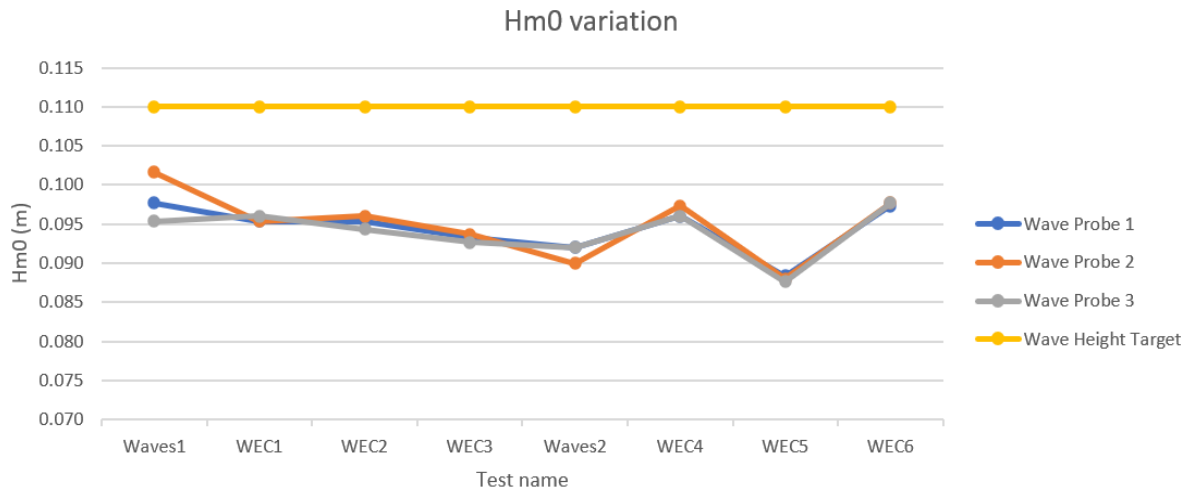


Figure 77 - Hm0 variation line chart.

There is a noticeable low point in the H_{m0} line chart for the “WEC5” test in Figure 77. These low values of wave height can be explained by a pump failure during the duration of the test. One of the two functioning pumps of the closed water circuit described in subchapter 3.1 was switched off for several minutes during the test. With one pump switched on, the total water pumped was not enough to maintain the constant head reservoir. With the decrease in the water level of the reservoir, the intake flow of the flume also decreased, and ultimately the flume water level diminished as well. This malfunction started at the end of the first wave train and extended until the second wave train as you can be assessed in Table 23.

Table 23 - H_{m0} collected (WEC5).

WEC5	Wave Probe 1	Wave Probe 2	Wave Probe 3
1° wave train	0.088	0.087	0.086
2° wave train	0.084	0.085	0.084
3° wave train	0.093	0.092	0.093

The data collected shows that the peak period measured consistently reached acceptable values, as the maximum difference from the target peak period less than 7%. As can be observed in Figure 78, the wave probe 2 registered slightly higher peak period values than the wave probe 3 across all the tests performed.

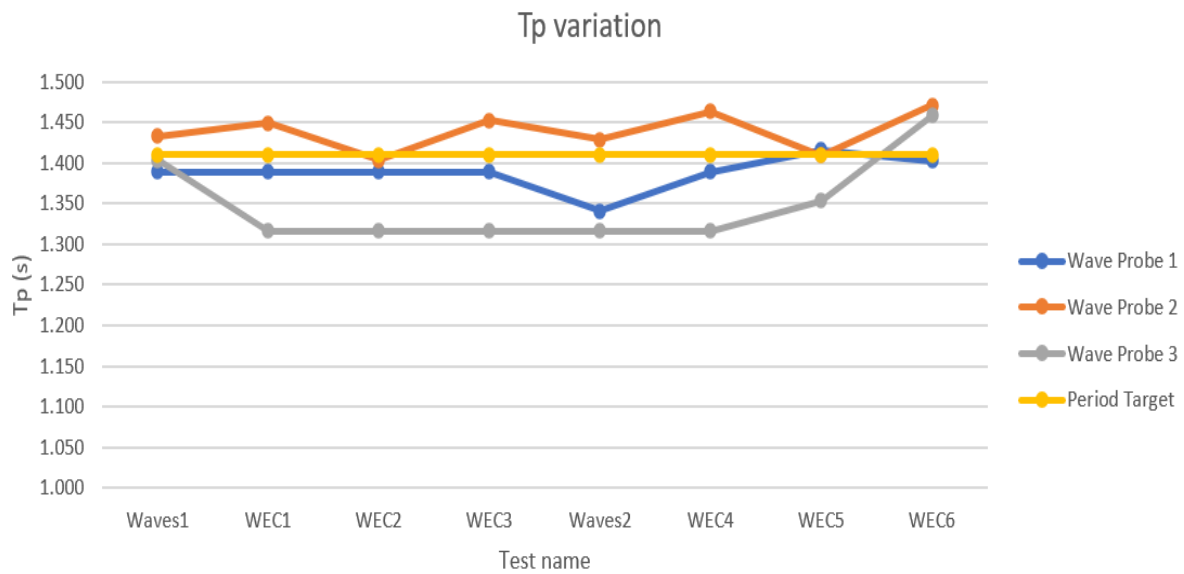


Figure 78 - Tp variation line chart.

As far the wave orbital speed variation from test to test, although less pronounced it experienced similar variances as the $Hm0$ variation. Again, the “WEC5” test encountered lower orbital speed values as shown in Figure 79.

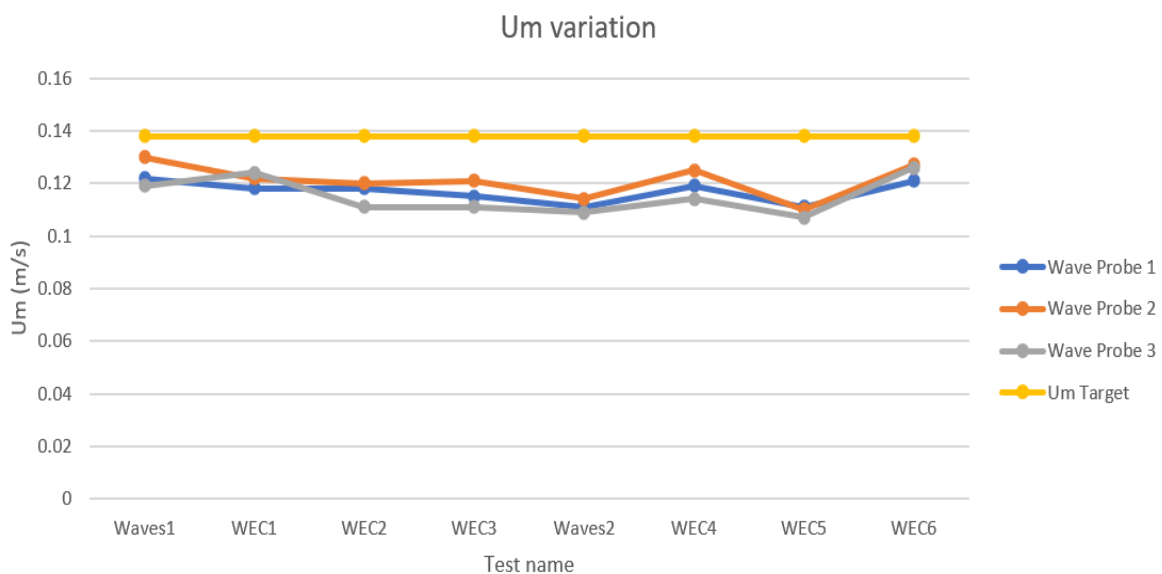


Figure 79 - Um variation line chart.

Another important value to understand and compare the scour tests is the velocity ratio, U_{cw} . Assuming a constant current velocity of 17.2 cm/s as estimated in subchapter 4.1.1, Table 24 shows the estimated U_{cw} value for each test. Note that because of the pump malfunction in test “WEC5”, the water level in the flume decreased momentarily during the test, and for that reason, the current velocity of 17.2 cm/s was an overestimation.

Table 24 - Orbital wave speed.

Test Name	Wave Probe 1	Wave Probe 2	Wave Probe 3
Waves 1	0.585 m/s	0.570 m/s	0.591 m/s
WEC 1	0.593 m/s	0.585 m/s	0.581 m/s
WEC 2	0.593 m/s	0.589 m/s	0.608 m/s
WEC 3	0.599 m/s	0.587 m/s	0.608 m/s
Waves 2	0.608 m/s	0.601 m/s	0.612 m/s
WEC 4	0.591 m/s	0.579 m/s	0.601 m/s
WEC 5	0.608 m/s	0.610 m/s	0.616 m/s
WEC 6	0.587 m/s	0.575 m/s	0.577 m/s

4.4.2. Foundation scour depth analysis

In the current subchapter, it can be found an in-depth analysis of the scour depths encountered in the soil. As mentioned before, the scour results were obtained by using the method described in subchapters 4.3.2, 4.3.3 and 4.3.4. In parallel to the scour values, deposition heights were also analyzed. The test conditions and maximum scour depth, S , experienced near the foundation can be found in Table 25. The scour maps of all the tests can be found in the appendix.

Table 25 - Table of scour results near the foundations.

Test number	Foundation	WEC Distance	D (cm)	Uc (m/s)	Um (cm/s)	Ucw	S (cm)	S/D
1.1	Monopile	-	11	0.172	0.130	0.570	3.3	0.30
1.2	GBF	-	18	0.172	0.119	0.591	1.6	0.09
2.1	Monopile	15 cm	11	0.172	0.122	0.585	1.3	0.12
2.2	GBF	15 cm	18	0.172	0.124	0.581	1	0.06
3.1	Monopile	25 cm	11	0.172	0.120	0.589	1.5	0.14
3.2	GBF	25 cm	18	0.172	0.111	0.608	1.1	0.06
4.1	Monopile	35 cm	11	0.172	0.121	0.587	1.3	0.12
4.2	GBF	35 cm	18	0.172	0.111	0.608	1.1	0.06
5.1	Monopile	-	11	0.172	0.114	0.601	5	0.45
5.2	GBF	-	18	0.172	0.109	0.612	1.8	0.10
6.1	Monopile	15 cm	11	0.172	0.125	0.579	1.8	0.16
6.2	GBF	15 cm	18	0.172	0.114	0.601	0.8	0.04
7.1	Monopile	25 cm	11	0.172	0.110	0.610	1.3	0.12
7.2	GBF	25 cm	18	0.172	0.107	0.616	0.3	0.02
8.1	Monopile	35 cm	11	0.172	0.127	0.575	1.7	0.15
8.2	GBF	35 cm	18	0.172	0.126	0.577	0.4	0.02

As can be analyzed in Figure 80 and Figure 81, when compared with the GBF, the monopile suffered consistently higher values of scour throughout the set of 8 tests. Some possible explanations for this occurrence can be attributed to the fact that the second sand box, where the GBF model was placed, was closer to the dissipation system that causes flow alterations. Despite the fact that the base diameter of the GBF is larger than the diameter of the monopile, another possible explanation for higher values of

scour in the monopile tests is the difference in total area of influence of the monopile (39 cm²) and the GBF (286 cm²).

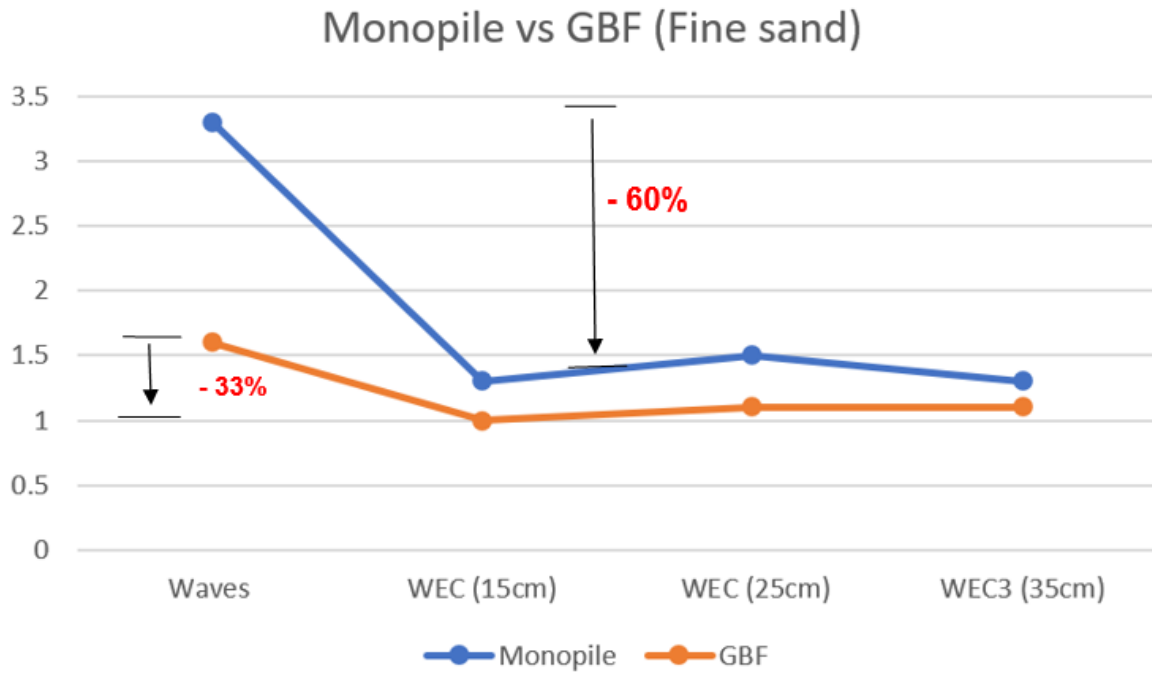


Figure 80 - Scour variation in fine sand tests.

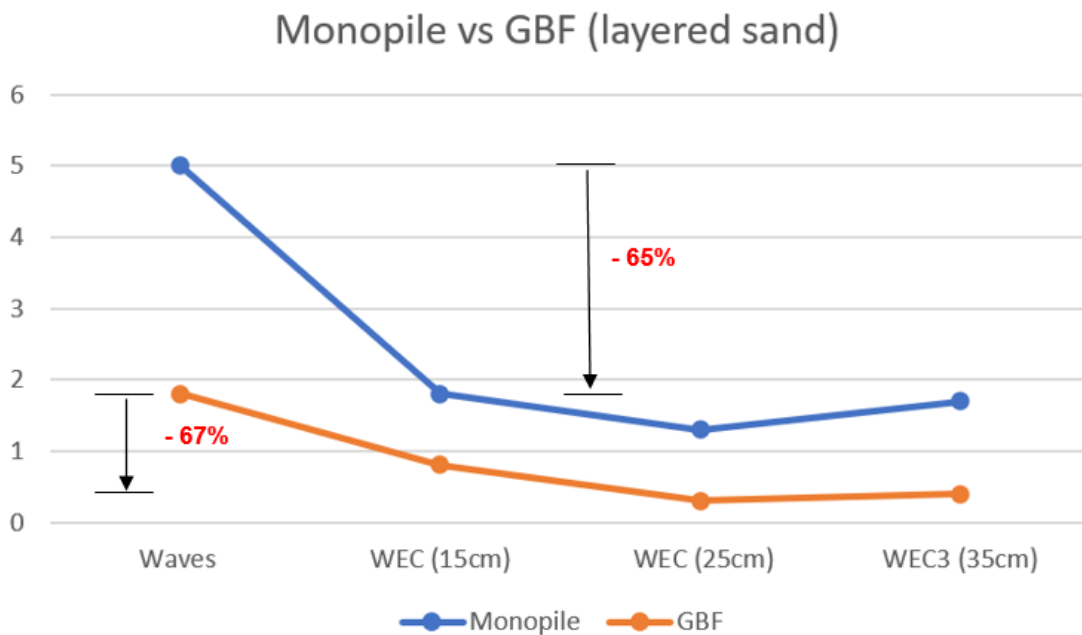


Figure 81 - Scour variation in layered sand tests.

The general influence of the WEC presence upstream of the foundation can be analyzed in Figure 80 and Figure 81. In the fine sand tests, the WEC presence caused an average 60% decrease in scour depths in the monopile and an average 33% decrease in scour depths in the GBF. While in the layered sand tests it caused an average 65% decrease in scour depths in the monopile and an average 67% decrease

in scour depths in the GBF. Note that for the layered sand tests the scour depths of the “WEC5” was not accounted for the calculation of the average decrease in scour depth since, as explained in subchapter 4.4.1, the pump malfunction registered caused an abnormal low value of scour.

By analyzing the scour results for test with a WEC device positioned in different distances from the foundation, it was not found any apparent relation between distance and scour depth. In order to find a acceptable relation between distance and scour depth, further tests should be performed with a larger range of distances and smaller increments in distance.

By isolating the monopile scour results in Figure 82 and excluding the “WEC5” results, unexpectedly due to an higher value of sediment dimension, it was possible to assess the overall higher values of scour for the layered sand configuration. An explanation for this occurrence is explored later in the following subchapter 4.4.3.

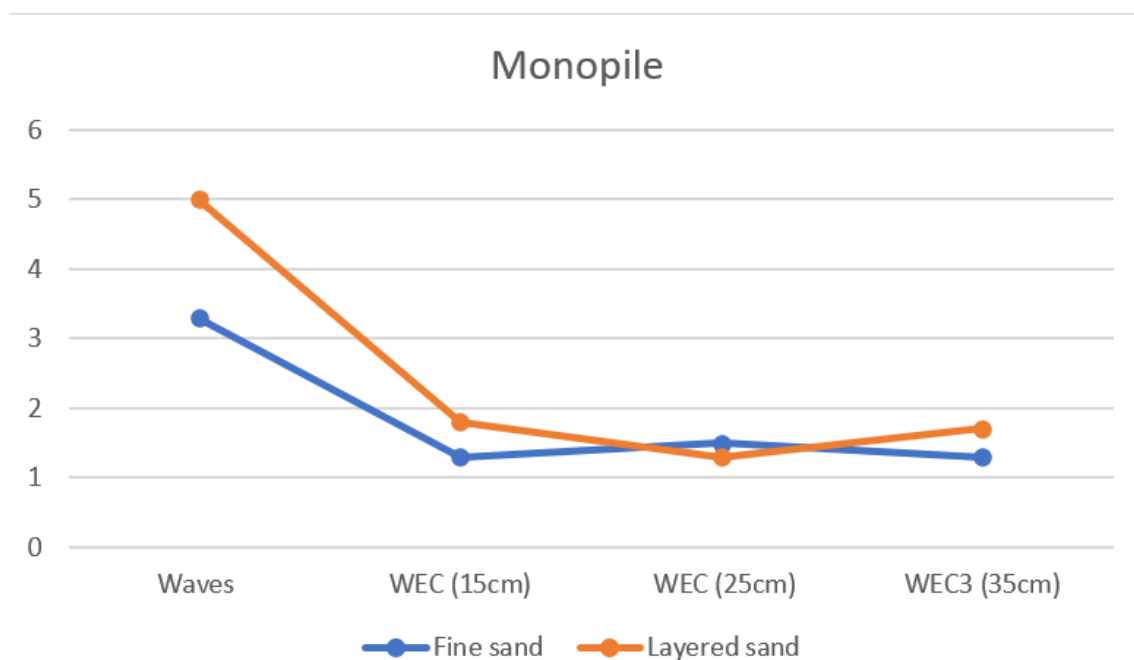


Figure 82 - Monopile Scour depths.

As for the isolated GBF scour results, without the presence of the WEC, the layered sand test also showed higher values of scour depth. However, in the presence of the WEC upstream of the GBF, the GBF suffered significantly lower values of scour depth even when excluding the “WEC5” scour value (Figure 83). The scour depth for the “WEC6” test was relatively low when compared with the scour depth for the “WEC4” test. During the “WEC6” test, a higher concentration of residues was noticeable (Figure 84). One possible explanation for the lower scour depths in “WEC6” is the armoring effect of the deposition of aforementioned residues. For that reason, in addition to the unreliability of the results of “WEC5” test, also the “WEC 6” results should be analyzed with a certain degree of unreliability.



Figure 83 - GBF scour depths.

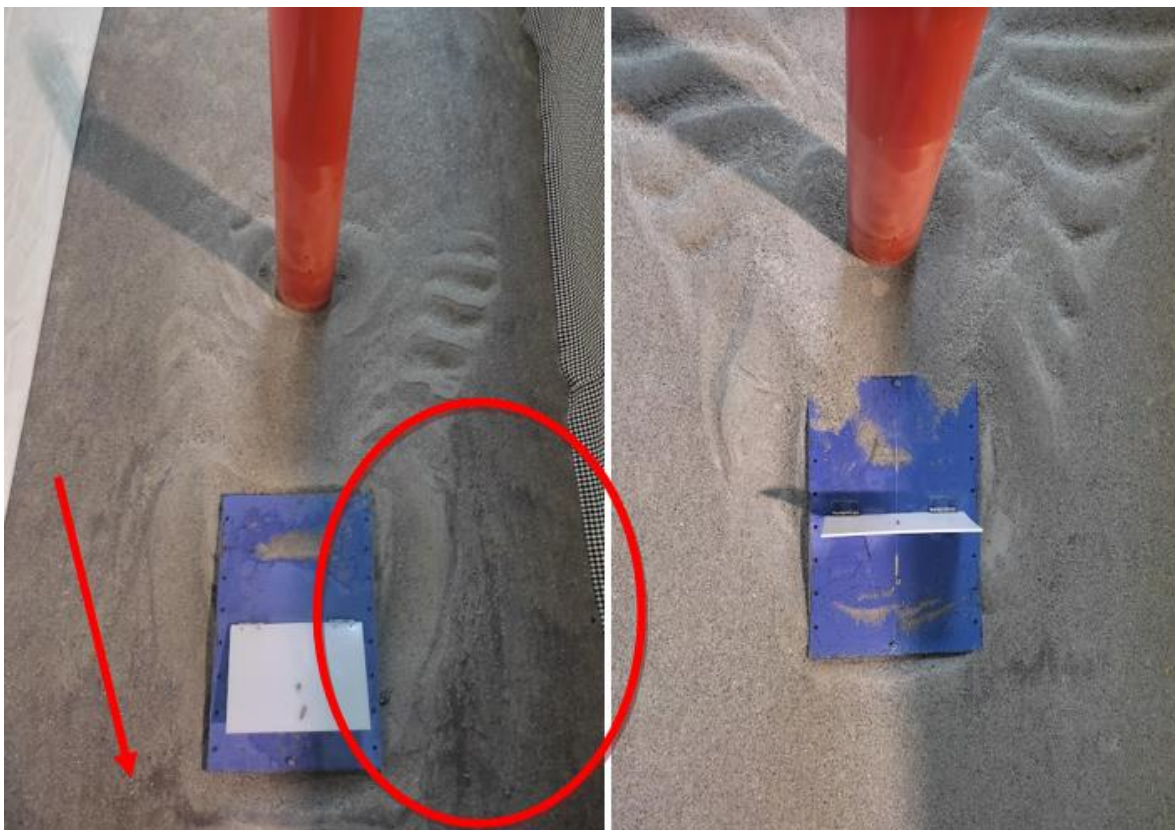


Figure 84 - Residue deposition in "WEC 6" (left); and "WEC 4" (right).

4.4.3. WEC scour depth analysis

In the current subchapter, a brief analysis of the scour depth and deposition heights experienced around the WEC model can be found. The results of scour depth near the WEC for each test are provided in Table 26, in which W is the width of the WEC paddle.

Table 26 - WEC scour depth table.

Test number	Foundation	WEC Distance (cm)	Width, W (cm)	Uc (m/s)	Um (cm/s)	Ucw	S_{wec} (cm)	S_{wec}/W
1.1	Monopile	-	15	0.172	0.130	0.570	-	-
1.2	GBF	-	15	0.172	0.119	0.591	-	-
2.1	Monopile	15	15	0.172	0.122	0.585	2.2	0.15
2.2	GBF	15	15	0.172	0.124	0.581	2.2	0.15
3.1	Monopile	25	15	0.172	0.120	0.589	2.8	0.19
3.2	GBF	25	15	0.172	0.111	0.608	2.2	0.15
4.1	Monopile	35	15	0.172	0.121	0.587	2.2	0.15
4.2	GBF	35	15	0.172	0.111	0.608	2.3	0.15
5.1	Monopile	-	15	0.172	0.114	0.601	-	-
5.2	GBF	-	15	0.172	0.109	0.612	-	-
6.1	Monopile	15	15	0.172	0.125	0.579	3.2	0.21
6.2	GBF	15	15	0.172	0.114	0.601	2.3	0.15
7.1	Monopile	25	15	0.172	0.110	0.610	1.9	0.13
7.2	GBF	25	15	0.172	0.107	0.616	1.8	0.12
8.1	Monopile	35	15	0.172	0.127	0.575	2.2	0.15
8.2	GBF	35	15	0.172	0.126	0.577	2.6	0.17

As can be seen, by analyzing Table 26, similarly to what was found in subchapter 4.4.2, it was not found an adequate correlation between WEC distance and scour depth. In order to assess the effect of distance in the scour depth around the WEC model, more tests for a wider range of distances to the foundation with smaller increments in distance should be performed in future works.

It is possible to observe a clear trend of a relation between scour depth and WEC paddle width, $S_{wec}/W = 0.15$. As previously referred, the tests 7.1 and 7.2 correspondent to the test “WEC5” present low values of scour due to the pump malfunctions. A possible explanation for the outlier values of scour in test 3.1 and 6.1 with $S_{wec}/W = 0.19$ and $S_{wec}/W = 0.21$, respectively, is a possible deficiency in the sand smoothing near the WEC model. However, note that in this experimental study, only one WEC paddle width, W , was tested. To observe and analyze the effects in scour of the WEC paddle width, W , a wider range of paddle dimensions should be investigated.

When analyzing the scour depth for the same distance and foundation model with different soil type in Figure 85, it was possible to observe that the layered sand tests experienced slightly larger values of scour.

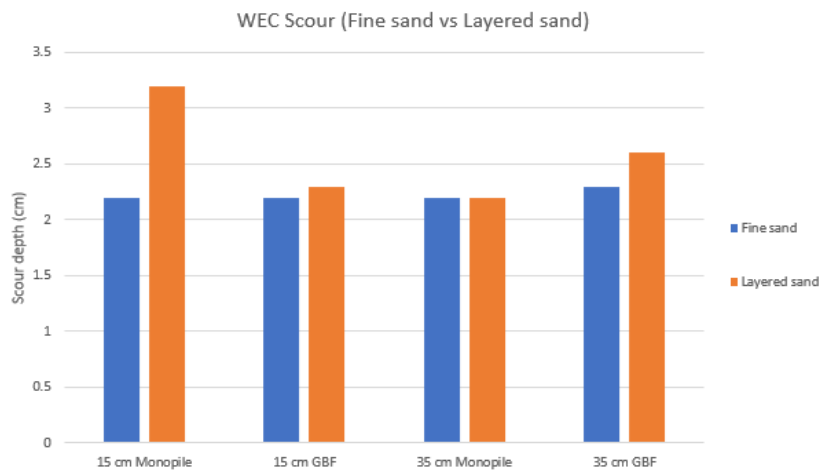


Figure 85 - WEC scour (fine sand vs layered sand).

In order to assess the possible negative or positive deposition effects in the scour protection near the foundation, the latter was also analyzed. In Table 27, it can be found the maximum deposition heights, dep_{max} , and their position downstream or upstream of the foundation, for each test performed. The deposition values upstream of the foundation for tests 1.1, 1.2, 5.1 and 5.2 were virtually zero since it was not visible that any deposition was registered apart from the forming of ripples. The increase in deposition downstream of the WEC, if coincident with scour area upstream of the foundation, constitutes a possible scour protection mechanism by filling the scour holes formed with the increased deposition coming from upstream.

Table 27 - Deposition results.

Test number	Foundation	Diameter, D (cm)	Width, W (cm)	WEC distance (cm)	dep_{max} (cm)	Position	dep_{max}/D or dep_{max}/W
1.1	Monopile	11	-	-	1.8	Downstream	0.16
1.2	GBF	18	-	-	1.3	Downstream	0.07
2.1	Monopile	-	15	15	1.7	Upstream	0.11
2.2	GBF	-	15	15	1.5	Upstream	0.10
3.1	Monopile	-	15	25	1.7	Upstream	0.11
3.2	GBF	-	15	25	1.4	Upstream	0.09
4.1	Monopile	-	15	35	2.2	Upstream	0.15
4.2	GBF	-	15	35	1.4	Upstream	0.09
5.1	Monopile	11	-	-	1.7	Downstream	0.11
5.2	GBF	18	-	-	1.2	Downstream	0.07
6.1	Monopile	-	15	15	1.9	Upstream	0.13
6.2	GBF	-	15	15	1.1	Upstream	0.07
7.1	Monopile	-	15	25	1.4	Upstream	0.09
7.2	GBF	-	15	25	1.0	Upstream	0.07
8.1	Monopile	-	15	35	1.1	Upstream	0.07
8.2	GBF	-	15	35	1.2	Upstream	0.08

Note that the current set of scour tests around the WEC model presents several shortcomings. In order to analyze the scour and deposition mechanisms around this type of WEC models more scour tests should be performed including the following variables:

- isolated scour tests;
- wider range of WEC paddle dimensions;
- wider range of distances from the foundation model; and
- smaller increments in distance in said range of distances.

One of the main objectives of the current dissertation was to assess the influence of the WEC in the scour patterns created in the base of the foundation. However, in order to further understand the scour/deposition interactions between the WEC and the foundation, it is important to test the WEC isolated from the foundation. One of the most critical variables in scour studies is the perpendicular-to-flow dimensions, for that reason a wider range of paddle dimensions should be tested. As referred before, to find a good relation between scour/deposition and distance to foundation in future works, it is necessary to perform scour test for a broader range of distances.

4.4.4. Scour pattern analysis

In this subchapter, it can be found a qualitative analysis of scour and deposition patterns observed in each performed test. This qualitative analysis was performed using the scour maps created with use of the CloudCompare software, as explained in subchapter 4.3.4. As referred in subchapter 4.1.1, the depth average current speed reached, $U_C=17.2$ cm/s, was significantly smaller than the theoretical value of critical depth average current speed for the model conditions, $U_C=27.7$ cm/s. However, as can be seen in Figure 86, the current speed of 17.2 cm/s in combination with the effect of the waves was enough to provoke the sediment transport responsible for the creation of the ripples observed.

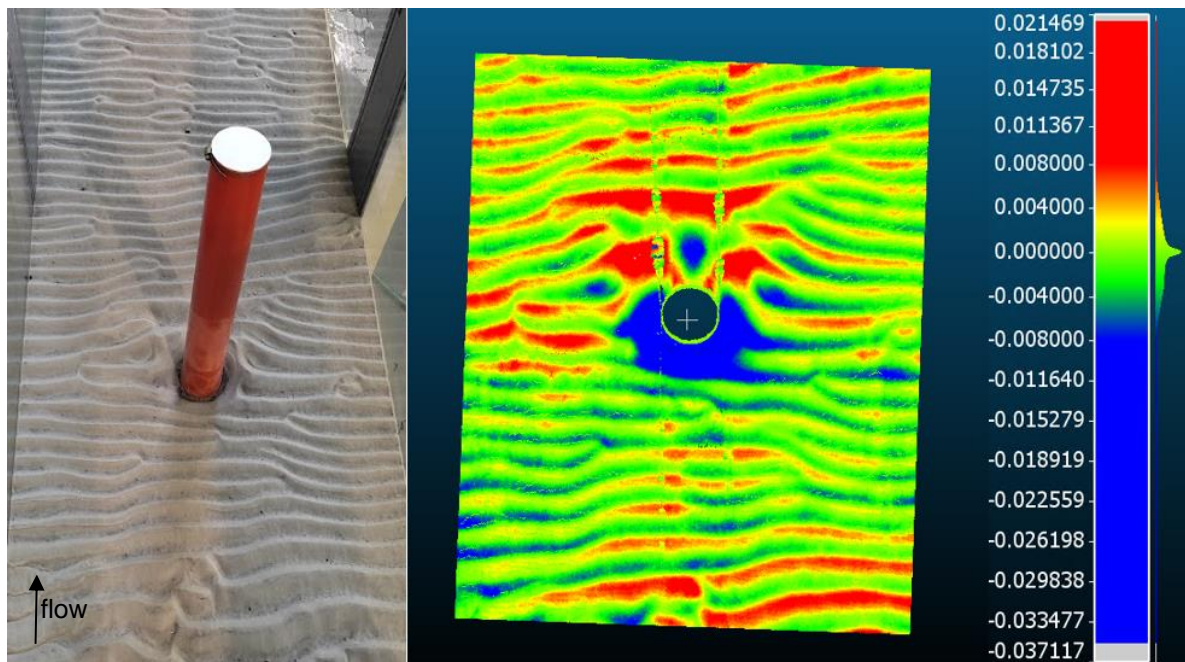


Figure 86 - "Waves 1" Monopile scour patterns (scour grading scale in meters).

However, as can be seen in Figure 87, the same rippling patterns were not found for the layered sand tests. The ripples were only found directly downstream of the monopile and a small area in the beginning of the sand box. The amplified bed shear stress formed due to the soil-fluid-structure interactions explained in 2.1, is responsible for the sediment transport observed and forming of the scour hole and ripples downstream of the monopile. A possible explanation for the small area of ripples, observed at the beginning of the sand box, is the local increase in flow velocity due to the flow interaction with the wave probe.

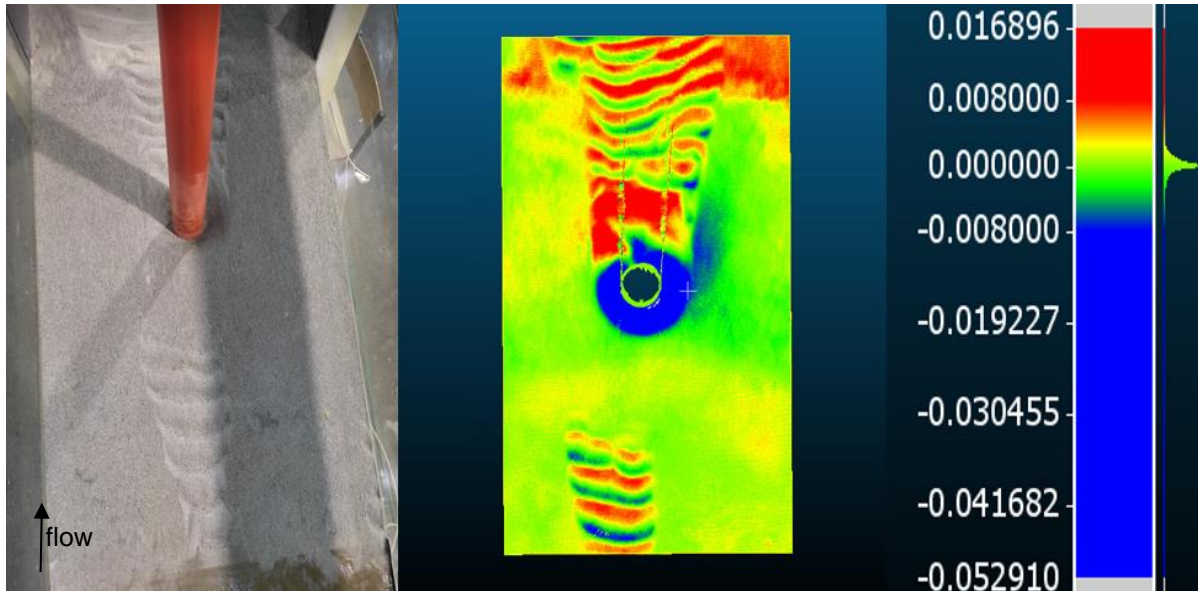


Figure 87 - "Waves 2" GBF scour patterns (scour grading scale in meters).

Similar observation can be found in the rest of the tests. However, another peculiarity was found in the GBF layered sand tests number 5.2, 6.2, 7.2 and 8.2. As visible in Figure 88, the forming of ripples was observed upstream of the WEC model. A possible explanation is the fact that due to the limited amount of available coarser sand the coarser sand layer did not cover the whole sand box. In Figure 89 it is possible to identify the limits of the coarser sand layer. Note that for the monopile test the coarser sand layer covered the whole study area, including the upstream buffer between the beginning of the sand box and the monopile model (Figure 90).

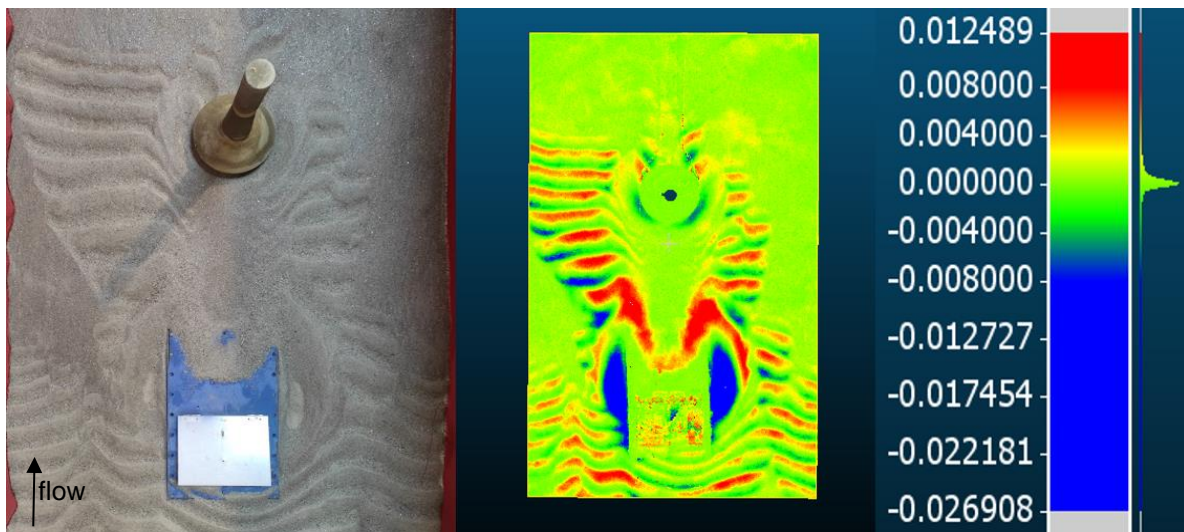


Figure 88 - "WEC 6" GBF Scour patterns (scour grading scale in meters).



Figure 89 - Coarser sand layer limits (GBF).

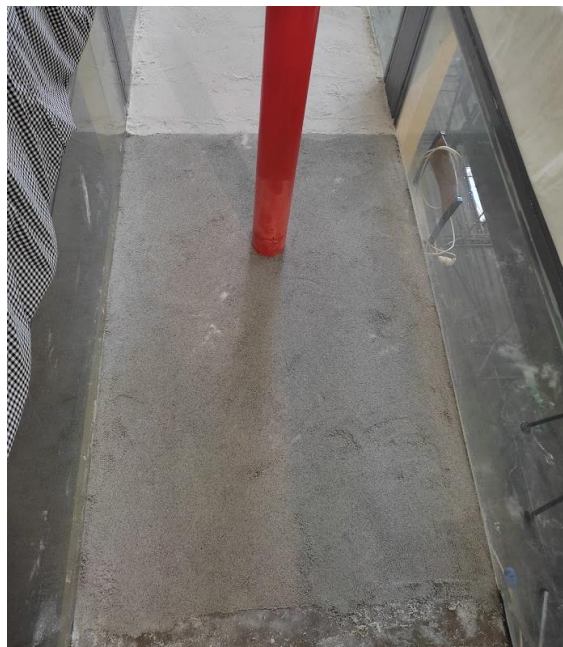


Figure 90 - Coarser sand layer limits (Monopile).

Another initially expected observation is the symmetry in scour patterns. In figure 91, the scour patterns in “WEC3” revealed a high degree of symmetry. Although symmetric scour patterns were observed in most tests, asymmetry ones were observed in tests number 5.2, 7.1, 7.2. The placement of the physical models unaligned to the flow is a possible explanation for the asymmetric patterns observed.

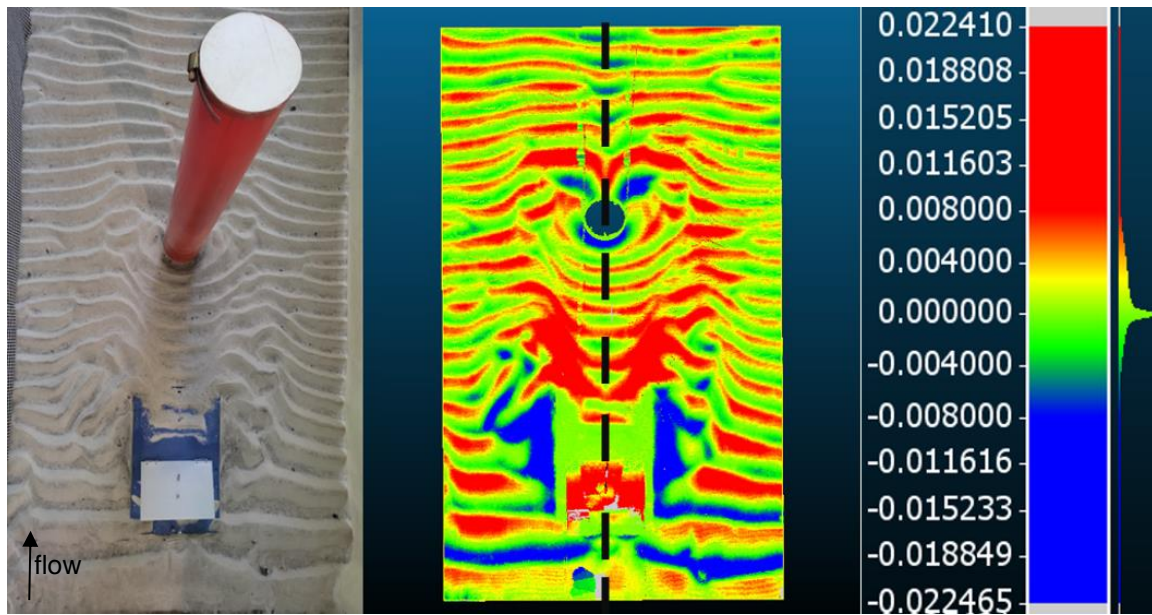


Figure 91 - "WEC3" Monopile scour pattern symmetry (scour grading scale in meters).

Differences in the shape of the scour hole were observed between correspondent scour test with fine sand and layered sand. Due to the forming of ripples in the surrounding areas in the fine sand tests, the limits of the scour hole are clearer for the layered sand tests as can be observed in Figure 92. The same observation was done for the WEC scour holes.

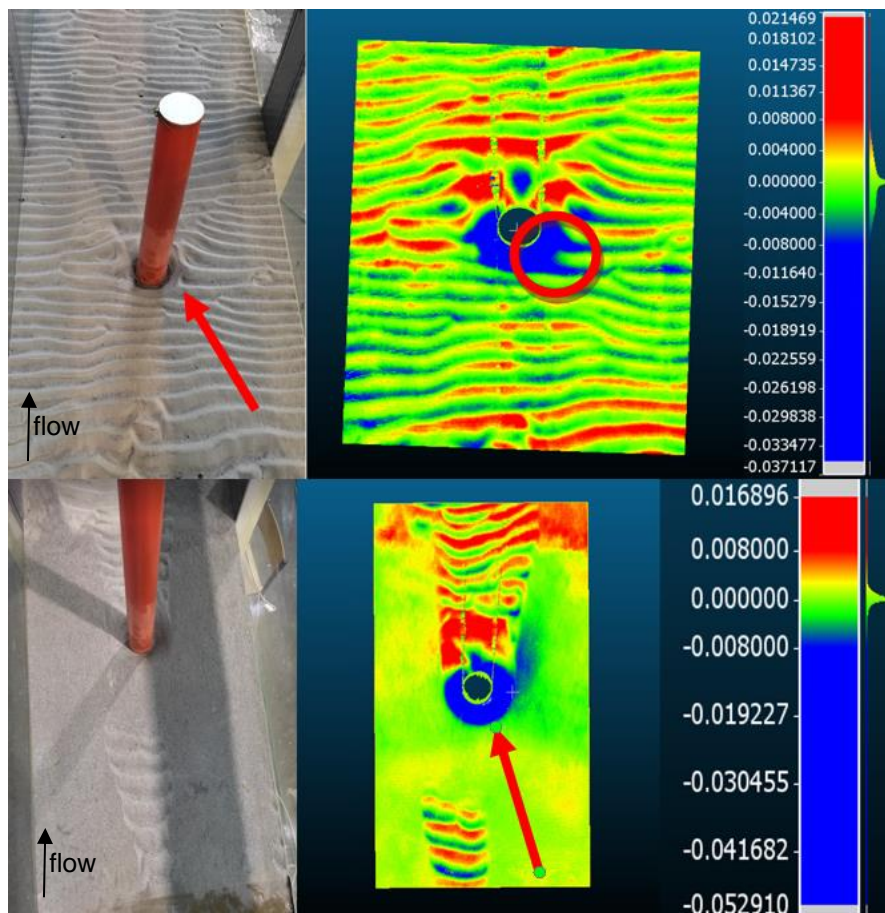


Figure 92 - Differences in shape of the scour hole "Waves1" (top); and "Waves2" (bottom).

As referred before in subchapter 4.4.2, the placement of the WEC device upstream of the foundation model increased the sediment deposition in the area between the WEC model and the foundation model. This is one of the main mechanisms responsible for the decrease in scour depth near the foundation models. This increase in sediment deposition can be clearly observed in Figure 93.

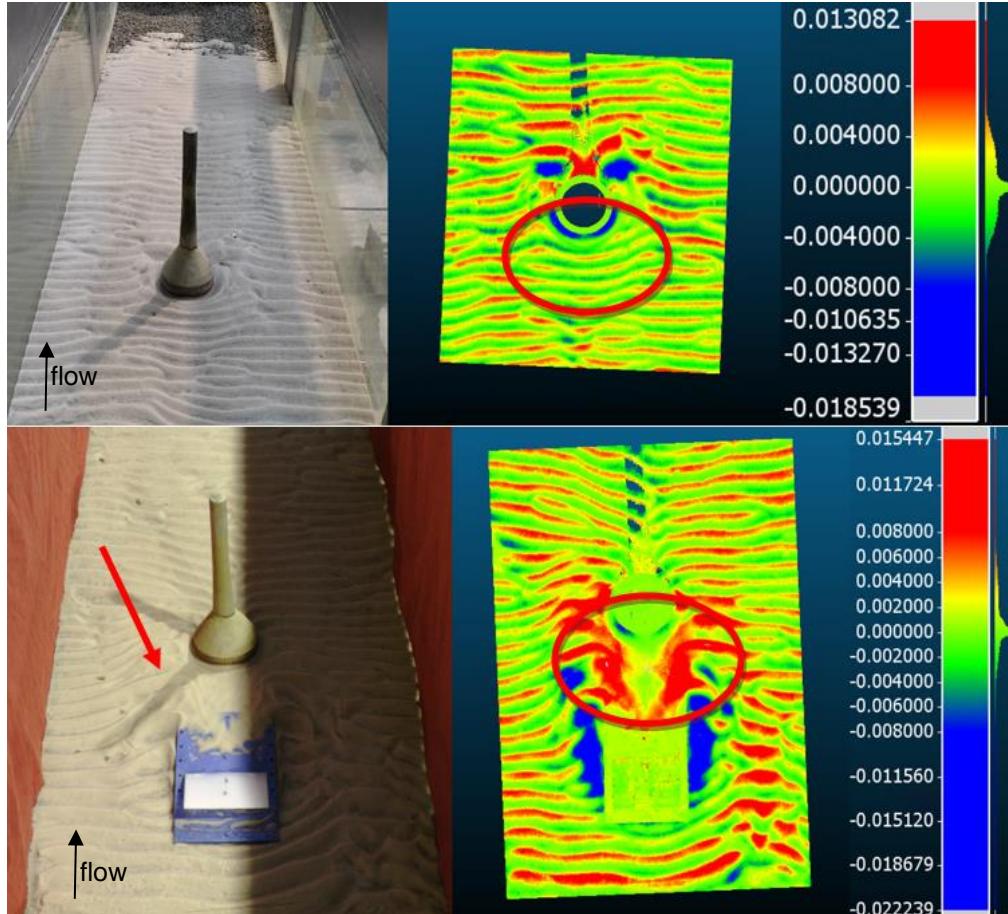


Figure 93 - Increased sediment deposition "Waves1" (top); and "WEC1" (bottom).

4.4.5. Layered sand scour holes analysis

As analyzed before in subchapter 4.4.1 and subchapter 4.4.2, the addition of a coarser sand layer does not necessarily decrease the scour depths experienced. The scour depth decrease was only observed when the scour depths did not reach the second sand layer. When analyzing the effects of the upper coarse sand layer on the GBF scour depth (Figure 83), it is possible to observe that the scour depth was increased in "Waves 2" and decreased in "WEC4", "WEC5", and "WEC6". As can be seen in Figure 94, the maximum scour depth of "Waves2" occurred in an area where the upper sand layer were totally washed, whilst to the maximum scour depth of "WEC4" was experienced in an area where the bottom layer was not reached.



Figure 94 - Layered sand scour hole "Waves2" (Left); and "WEC4" (Right).

These observations suggest that for layered sands, the scour is intensified in areas where the upper layer is completely washed away. Similar observations were obtained in laboratory studies made in Porter et al. (2012) and Porter et al. (2013).

5

Conclusions and Future Works

5.1. Conclusions

The present dissertation is focussed on the study of scour depths and scour patterns around the foundations of offshore marine energy harvesting technologies. Two sets of experimental tests were conducted in the hydraulic laboratory at FEUP. The current dissertation is an exploratory set of physical model testing laying the foundations for future studies on scour around monopile and GBF foundations in complex soils, and a preliminary study on hybridization of marine energy technologies. From the discussion of results in Chapter 4, and the following main conclusions can be withdrawn:

- Scour depth was reduced in the order of 60% when the oscillating wave surge converter was placed upstream of the foundation. By analysing the line charts from of Figure 80 and Figure 81, it is possible to observe these reductions of around 60% on the scour depth near the foundation except for the GBF scour tests in fine sand, which presented reductions in the order of 30%.
- It was not found any obvious relation between WEC distance to the foundation and reduction in scour depth.
- One of the mechanisms of scour protection observed was the increase in sediment deposition in the area between the WEC device and the wind foundation, as can be seen from Figure 93.
- In the layered sand tests, when the upper coarse sand layer was fully washed, the scour mechanisms were enhanced in the underlying layer. As referred in 4.4.5, higher values of scour were registered in the layered sand test except when the total scour did not reach the inferior layer. In those cases, the total scour was in fact reduced. Similar observations were also observed in an experimental study conducted by Porter et al. (2012), and Porter et al. (2013).
- The hydrodynamic conditions tested were enough to create live bed conditions for the fine sand soil. However, the same hydrodynamic conditions created clear water conditions for the layered sand soil. Using the method introduced in Soulsby (1997), the theoretical value of the critical depth averaged current speed of the model conditions was $U_c = 0.277$ m/s. However, due to the flume limitations the maximum depth-averaged current speed achievable was 0.172 m/s. Nevertheless, as shown by the development of the ripples, live bed conditions were reached for the fine sand tests.
- Significant scour hole shape differences were observed between the fine sand soil and layered sand soil. As shown in Figure 92, the shape of the scour holes significantly changed between the fine sand tests and the layered sand tests. These changes were attributed to the development of ripples for the first case.

Due to the short number of tests performed, the present study provides an analysis which is more qualitative than quantitative. However, this can be improved by more detailed analysis on a larger data-

set. Another limitation of the current experimental study was the fact that some model effects, such as the reflection of the flume were not eliminated. These limitations are addressed in the next subchapter 5.2.

The present study provides evidence that the presence of bottom-fixed wave energy converters in the vicinity of bottom-fixed offshore wind foundations has a significant impact on the local sediment transport and scour phenomena. This effect appears to be dependent on the soil's arrangement and the distance between the WEC and the wind foundation. Given the importance of this topic to the costs' of offshore wind foundations, further studies should be performed to establish methodologies that can relate the scour depth with the distance between both elements and the type of soil arrangement.

5.2. Future works

As explained before, the present experimental study presents several limitations. Firstly, in order to address the current limitations and increase the overall potential applicability of this work the following physical model and measurement methodology improvements should be done:

- Reduce significantly the reflection experienced. The dissipation beach configuration should be redefined. Following the works of Fraga (2017), a node and antinode analysis should be performed in order to find the optimal spacing between the metal sheets of the dissipation beach. Another possible improvement to the current dissipation beach configurations is the use of cork bottle caps in combination with a gravel profile.
- In future works, the depth average current velocity should be measured near both study areas before each test, in order to assess the flow conditions for each test more accurately.
- Improve the laser scanning process. In order to minimize the inaccuracies observed in the laser scanning process, a new laser scan positioning, such as the one described in sub-chapter 4.3.4, should be idealized.

Apart from the physical model and measurement methodology improvements, future works should primarily focus on the performance of a more extensive set of tests. As the current explores a wide variety of variables, the following intuitive future works were identified:

- Oscillating wave surge converter scour study. In order to further understand the viability of the implementation of these types of hybrid solutions to the foundations of offshore wind farms, a more in-depth oscillating wave surge converter scour study should be performed. This study should include: a set of oscillating wave surge converter scour tests to serve as reference; a wide range of oscillating wave surge converter dimensions and distance to the wind foundation.
- Tests designed to assess scour in a more comprehensive manner. In order to find more conclusive results, an higher number scour tests should be carried out. This extensive scour set of tests should include a wider range of flow conditions to compare the results obtained with previous experimental tests in the literature.
- Expand the complex soil scour testing. A more extensive complex soil scour testing should be done. This study should include more types of complex soils, such as the complex soil configurations studied in Porter et al. (2013), a scour time evolution study to assess the enhancement of scour mechanisms in the underlying layers.

References

- Abu Husain, M. K., Mohd Zaki, N. I., & Najafian, G. (2013). *Prediction of Extreme Offshore Structural Response: An Efficient Time Simulation Approach*. <https://doi.org/10.13140/2.1.5095.3924>
- Airy, G. B. (1845). *Tides and Waves*. B. Fellowes. <https://books.google.pt/books?id=LUDlnQEACAAJ>
- Baker, C. J. (1979). The laminar horseshoe vortex. *Journal of Fluid Mechanics*, 95(2), 347-367. <https://doi.org/10.1017/S0022112079001506>
- Bhattacharya, S. (2014). Challenges in Design of Foundations for Offshore Wind Turbines. *Institution of Engineering and Technology*, 1. <https://doi.org/10.1049/etr.2014.0041>
- Bond, A. J., Hight, D. W., & Jardine, R. J. (1997). *Design of piles in sand in the UK sector of the North Sea*. H. a. S. E.-O. T. Report.
- Bos, K. J., Verheij, H. J., Kant, G., & Kruisbrink, A. C. H. (2002). Scour Protection Around Gravity Based Structures Using Small Size Rock. In.
- Brandimarte, L., Paron, P., & Di Baldassarre, G. (2012). Bridge pier scour: A review of processes, measurements and estimates. *Environmental engineering and management journal*, 11. <https://doi.org/10.30638/eemj.2012.121>
- Breusers, H. N. C., & Raudkivi, A. J. (1991). *Scouring: Hydraulic structure design manual series - IAHR Design Manual*.
- Center for Wind Energy. (2012). *Review of Options for Offshore Foundation Substructures*.
- Chambel, J. (2019). *Analysis of Long-Term Damage of Offshore Wind Turbine Foundations*
- Chehaze, W., Chamoun, D., Bou-Mosleh, C., & Rahme, P. (2016). Wave Roller Device for Power Generation. *Procedia Engineering*, 145, 144-150. <https://doi.org/10.1016/j.proeng.2016.04.033>
- Colmenar-Santos, A., Perera-Perez, J., Borge-Diez, D., & dePalacio-Rodríguez, C. (2016). Offshore wind energy: A review of the current status, challenges and future development in Spain. *Renewable and Sustainable Energy Reviews*, 64, 1-18. <https://doi.org/https://doi.org/10.1016/j.rser.2016.05.087>
- Coughlan, M., Fleischer, M., Wheeler, A. J., Hepp, D. A., Hebbeln, D., & Morz, T. (2018). A revised stratigraphic framework for the Quarternary deposits of the German North Sea sector: a geological-geotechnical approach. *Boreas*, 47.
- Dahlberg, R. (1983). Observations of scour around offshore structures. *Canadian Geotechnical Journal*, 20, 617-628.
- De Vos, L. (2008). *Optimisation of scour protection design for monopiles and quantification of waver run-up* [PhD Thesis, Ghent University].
- De Vos, L., Rouck, J., Troch, P., & Frigaard, P. (2011). Empirical design of scour protections around monopile foundations: Part 1: Static approach. *Coastal Engineering*, 58, 540-553. <https://doi.org/10.1016/j.coastaleng.2011.02.001>
- Dixen, M., Dixen, F., Sumer, B., & Fredsoe, J. (2008). Wave boundary layer over a stone-covered bed. *Coastal Engineering*, 55, 1-20. <https://doi.org/10.1016/j.coastaleng.2007.06.005>
- Esteban, M. D., Couñago, B., Lopez-Gutierrez, J., Negro, V., & Vellisco, F. (2015). Gravity based support structures for offshore wind turbine generators: Review of the installation process. *Ocean Engineering*, 110, 281-291. <https://doi.org/10.1016/j.oceaneng.2015.10.033>
- Esteban, M. D., Lopez-Gutierrez, J., & Negro, V. (2019). Gravity-Based Foundations in the Offshore Wind Sector. *Journal of Marine Science and Engineering*, 7, 64. <https://doi.org/10.3390/jmse7030064>
- EY. (2015). *Ernst & Young Limited Offshore Wind in Europe - Walking the Tightrope to Success*. E. Young.
- Fazerer-Ferradosa, T. (2018). *Reliability Analysis Applied to The Optimization od Dynamic Scour Protections for Offshore Windfarm Foundations*

- Fazeres-Ferradosa, T., Chambel, J., Taveira-Pinto, F., Rosa-Santos, P., Taveira-Pinto, F. V. C., Giannini, G., & Haerens, P. (2021). Scour Protections for Offshore Foundations of Marine Energy Harvesting Technologies: A Review. *Journal of Marine Science and Engineering*, 9(3). <https://doi.org/10.3390/jmse9030297>
- Fenton, J. (1999). *NUMERICAL METHODS FOR NONLINEAR WAVES*. World Scientific.
- Fleischer, M., Abegunrin, A., Hepp, D. A., Kreiter, S., Coughlan, M., & Morz, T. (2022). Stratigraphic and geotechnical characterization of regionally extensive and highly competent shallow sand units in the southern North Sea. *Boreas*. <https://doi.org/https://doi.org/10.1111/bor.12595>
- Fraga, T. R. (2017). *ESTUDO DE METODOLOGIAS PARA CONTROLO DAS REFLEXÕES EM LABORATÓRIO FEUP*.
- Fredsøe, J., & Deigaard, R. (1992). *Mechanics of Coastal Sediment Transport*.
- Frostick, L. E., J., M. S., & Mercer, T. G. (2011). *Users Guide to Physical Modelling and Experimentation: Experience of the HYDRALAB Network*. CRC Press.
- Harris, J., Whitehouse, R., & Benson, T. (2010). The time evolution of scour around offshore structures. *Proceedings of The Institution of Civil Engineers-maritime Engineering - PROC INST CIVIL ENG-MARIT ENG*, 163, 3-17. <https://doi.org/10.1680/maen.2010.163.1.3>
- Hoffmans, G. J. C. M., & Verheij, H. J. (1997). *Scour Manual*.
- Lavanya, C., & Kumar, N. D. (2020). Foundation Types for Land and Offshore Sustainable Wind Energy Turbine Towers. *E3S Web of Conferences*, 184, 01094. <https://doi.org/10.1051/e3sconf/202018401094>
- LeBlond, P. H., Calisal, S. M., & Isaacson, M. (1982). *Wave spectra in Canadian waters*.
- Liu, Z. (1998). *Sediment Transport*.
- Loosveldt, N., & Vannieuwenhuysse. (2012). *Experimental validation of empirical design of a scour protection around monopiles under combined wave and current loading* Gent University].
- Melville, B., & Chiew, Y.-M. (1999). Time scale for local scour at bridge piers. *Journal of Hydraulic Engineering*, 125, 59-65. [https://doi.org/10.1061/\(ASCE\)0733-9429\(1999\)125:1\(59\)](https://doi.org/10.1061/(ASCE)0733-9429(1999)125:1(59))
- Melville, B., & Raudkivi, A. J. (1977). Flow Characteristics in Local Scour at Bridge Piers. *Journal of hydraulic Research*.
- Melville, B., & Sutherland, J. (1988). Design Method for Local Scour at Bridge Piers. *Journal of Hydraulic Engineering*.
- Mengé, P. (2008). Gravity Base Foundations for the Wind Turbines on the Thorntonbank – Belgium.
- Miles, J., Martin, T., & Goddard, L. (2017). Current and wave effects around windfarm monopile foundations. *Coastal Engineering*, 121, 167-178. <https://doi.org/Doi 10.106/j.costaleng.2017.01.003>
- MOREnergy lab. (2022). *WEC WAVE ENERGY CONVERTER* Retrieved 14/05/2022 from <http://www.moreenergylab.polito.it/wec/>
- Nielsen, A. W., Liu, X., Sumer, B. M., & Fredsøe, J. (2013). Flow and bed shear stresses in scour protections around a pile in a current. *Coastal Engineering*, 72, 20-38. <https://doi.org/https://doi.org/10.1016/j.coastaleng.2012.09.001>
- Nielsen, P. (1992). *Coastal Bottom Boundary Layers and Sediment Transport*.
- Nielsen, P., & Guard, P. (2010). Vertical scales and shear stresses in wave boundary layers over movable beds. *Proceedings of the International Conference on Coastal Engineering; No 32 (2010): Proceedings of 32nd Conference on Coastal Engineering, Shanghai, China, 2010.; sediment.1, 1*. <https://doi.org/10.9753/icce.v32.sediment.1>
- Oh, K.-Y., Kim, J.-Y., & Lee, J.-S. (2013). Preliminary evaluation of monopile foundation dimensions for an offshore wind turbine by analyzing hydrodynamic load in the frequency domain. *Renewable Energy*, 54.

- Petersen, T. U., Mutlu Sumer, B., Fredsøe, J., Raaijmakers, T. C., & Schouten, J.-J. (2015). Edge scour at scour protections around piles in the marine environment — Laboratory and field investigation. *Coastal Engineering*, 106, 42-72.
<https://doi.org/https://doi.org/10.1016/j.coastaleng.2015.08.007>
- Porter, K., Harris, J., Simons, R., & Fazerer Ferradosa, T. (2013). A laboratory study of scour in mixed and layered sand beds. *Coastal Engineering, to be published (date to be announced)*.
- Porter, K., Simons, R., Harris, J., & Fazerer Ferradosa, T. (2012). SCOUR DEVELOPMENT IN COMPLEX SEDIMENT BEDS. *Coastal Engineering Proceedings*, 1.
<https://doi.org/10.9753/icce.v33.sediment.3>
- Qi, W., & Gao, F. (2014). Equilibrium scour depth at offshore monopile foundation in combined waves and current. *Science China Technological Sciences*, 57(5), 1030-1039.
<https://doi.org/10.1007/s11431-014-5538-9>
- Raudkivi, A. J., & Ettema, R. (1977). Effect of Sediment Gradation on Clear Water Scour. *Journal of the Hydraulics Division*, 103(10), 1209-1213. <https://doi.org/10.1061/jycej.0004853>
- Rosa-Santos, P. (2010). *Análise da Interação de Navios com Dispositivos de Acostagem e Amarração. Estudo em Modelo Físico do Posto "A" do Terminal de Petroleiros do Porto de Leixões* [PhD Thesis, University of Porto].
- Roulund, A., Sumer, B., Fredsoe, J., & Michelsen, J. (2005). Numerical and experimental investigation of flow and scour around a circular pile. *Journal of Fluid Mechanics*, 534, 351-401.
<https://doi.org/10.1017/S0022112005004507>
- Saruwatari, A., Yoneko, Y., & Tajima, Y. (2014). EFFECTS OF WAVE, TIDAL CURRENT AND OCEAN CURRENT COEXISTENCE ON THE WAVE AND CURRENT PREDICTIONS IN THE TSUGARU STRAIT. *Coastal Engineering Proceedings*, 1, 42.
<https://doi.org/10.9753/icce.v34.currents.42>
- Shields, A. (1936). *Application of similarity principles and turbulence researche to bed-load movement (Translated from German)*.
- Silva, R. C. A. F. D. (2010). *Avaliação Experimental e Numérica de Parâmetros Associados a Modelos de Evolução da Linha de Costa* University of Porto].
- Soulsby, R. (1997). *Dynamics of marine sands: A manual for practical applications*.
- Sumer, B., & Fredsøe, J. (2001). Scour around Pile in Combined Waves and Current *Journal of Hydraulic Engineering*, 127.
- Sumer, B., & Fredsøe, J. (2002). *The Mechanics of Scour in the Marine Environment*.
- Sumer, B., Fredsøe, J., & Christiansen, N. (1992). Scour around vertical pile in waves. *Journal of Waterway, Port, Coastal, Ocean Engineering*, ASCE, 118.
- Sumer, B., N, C., & Fredsøe, J. (1992). *Time Scale Of Scour Around A Vertical Pile*.
- Sumer, B. M., Whitehouse, R. J. S., & Tørum, A. (2001). Scour around coastal structures: a summary of recent research. *Coastal Engineering*, 44(2), 153-190. [https://doi.org/https://doi.org/10.1016/S0378-3839\(01\)00024-2](https://doi.org/https://doi.org/10.1016/S0378-3839(01)00024-2)
- Taveira-Pinto, F. V. C. (2021). *Physical Modelling in Marine Hydraulics - PRODEC048 "Scour Assessment on a Detached Rubble-Mound Breakwaters using advanced measurement equipment"*.
- Tavouktsoglou, N. S. (2018). *Scour and scour protection around offshore gravity based foundations* UCL].
- Thomas, S. (1989). *Geotechnical investigation of UK test sites for the foundations of offshore structures*. HMSO.
- Us Army Corps of Engineers. (2002). *Coastal Engineering Manual*.

Vogel, F., Holm, S., & Lingjærde, O. (2001). SPECTRAL MOMENTS AND TIME DOMAIN REPRESENTATION OF PHOTOACOUSTIC SIGNALS USED FOR DETECTION OF CRUDE OIL IN PRODUCED WATER.

Whitehouse, R. (1998). *Scour at marine structures: A manual for practical applications*.

Whitehouse, R., Harris, J., & Sutherland, J. (2004). Evaluating scour at marine gravity structures.

Whitehouse, R., Sutherland, J., & Harris, J. (2011). Evaluating scour at marine gravity foundations. *Proceedings of the ICE - Maritime Engineering*, 164, 143-157.
<https://doi.org/10.1680/maen.2011.164.4.143>

Wiberg, P. L., & Sherwood, C. R. (2008). Calculating wave-generated bottom orbital velocities from surface-wave parameters *Computers and Geoscience* 34.

WindEurope. (2022a). North Sea Offshore Wind to Help Repower the EU Retrieved 01/06/2022, from

WindEurope. (2022b). *Wind energy in Europe: 2021 Statistics and the outlook for 2022-2026*. Retrieved 24 February 2022 from

Wu, M., De Vos, L., Arboleda, C., Stratigaki, V., Fazeres Ferradosa, T., Santos, P., Taveira-Pinto, F., & Troch, P. (2020). Large Scale Experimental Study of the Scour Protection Damage Around a Monopile Foundation Under Combined Wave and Current Conditions. *Journal of Marine Science and Engineering*, 8. <https://doi.org/10.3390/jmse8060417>

APPENDIX

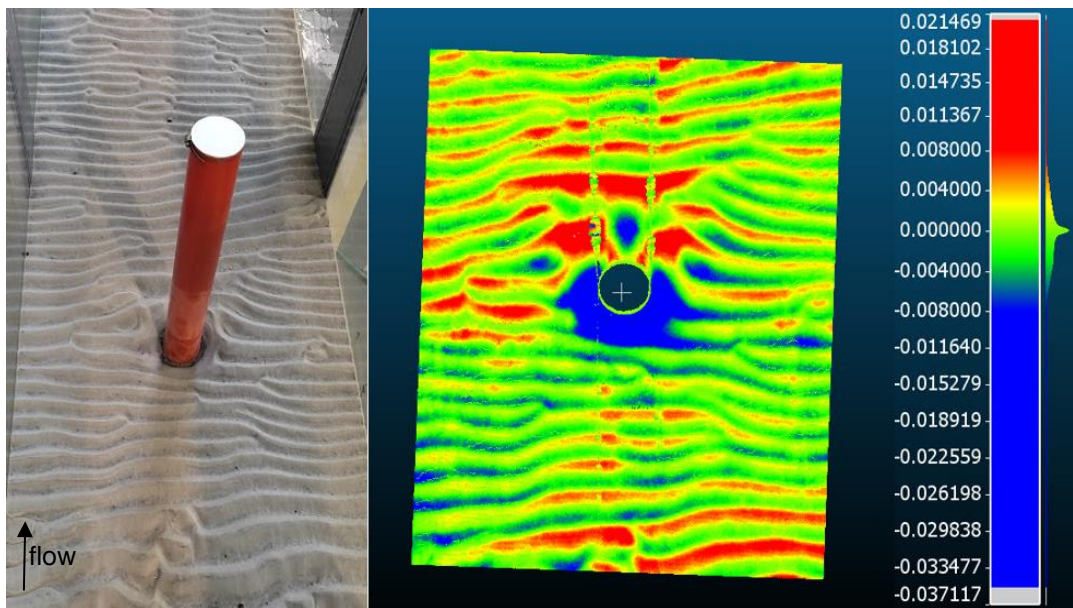


Figure 95 - "Waves 1" Monopile Scour patters; Scour grading scale in meters.

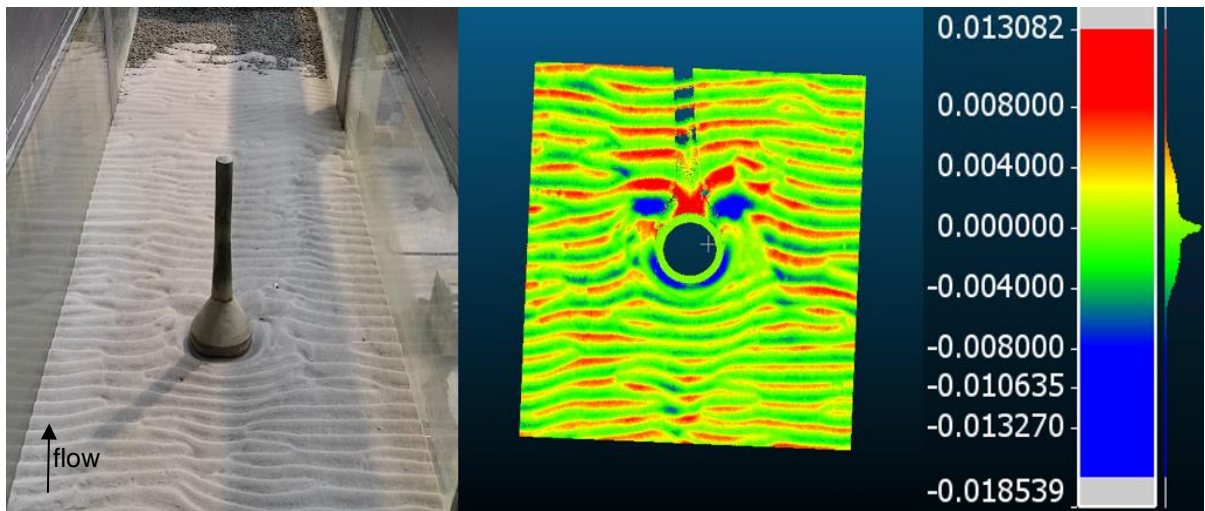


Figure 96 - "Waves 1" GBF scour patterns; Scour grading scale in meters.

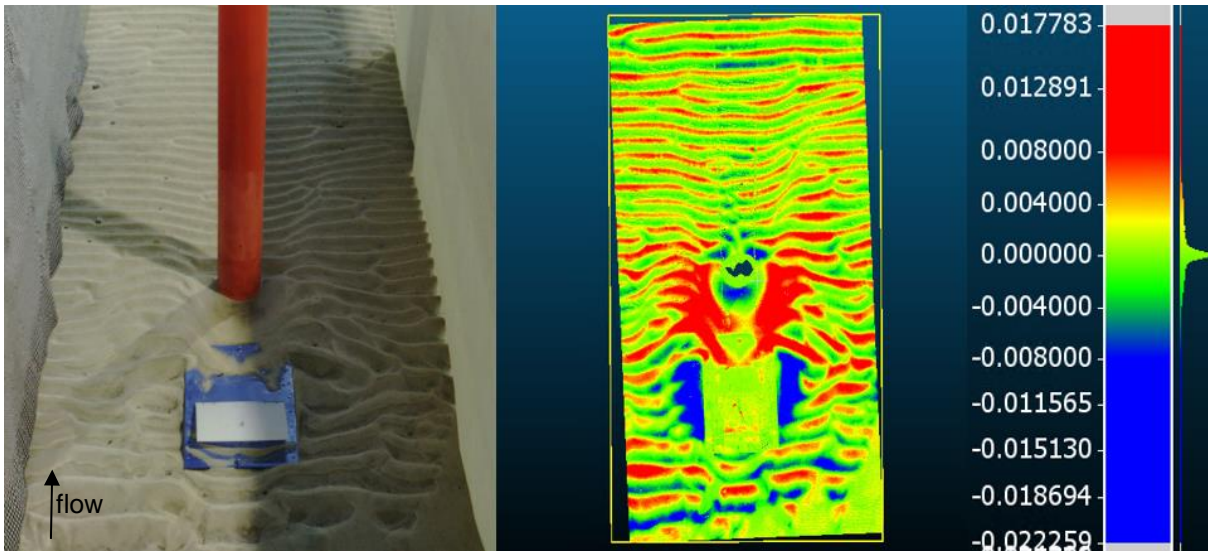


Figure 97 - "WEC1" Monopile scour patterns; Scour grading scale in meters.

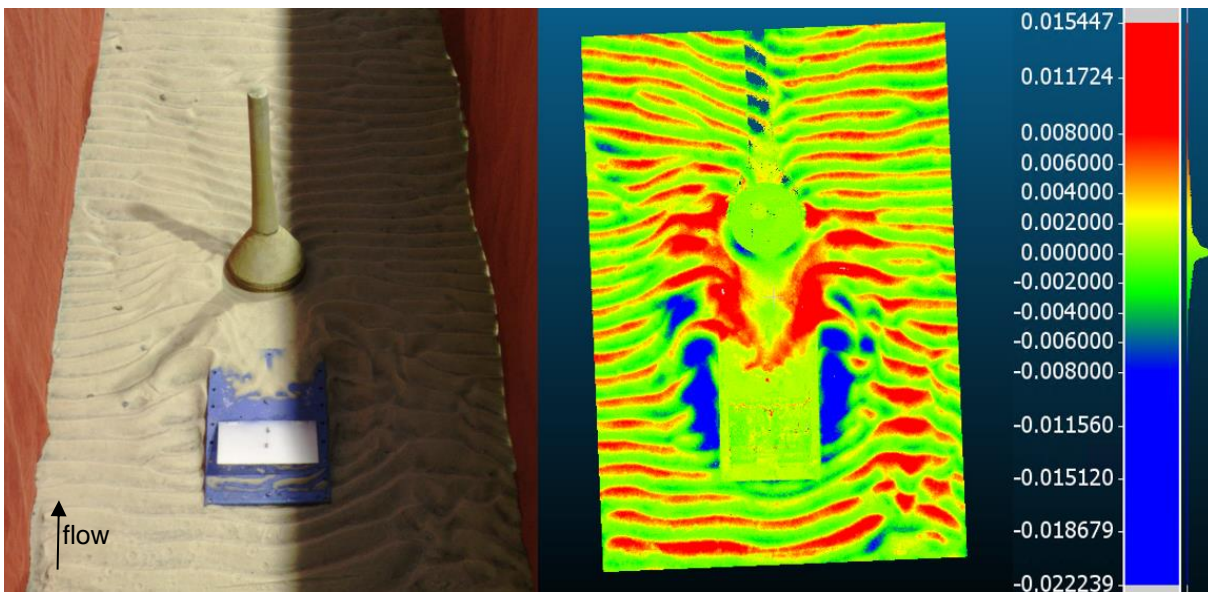


Figure 98 - "WEC1" GBF scour patterns; Scour grading scale in meters.

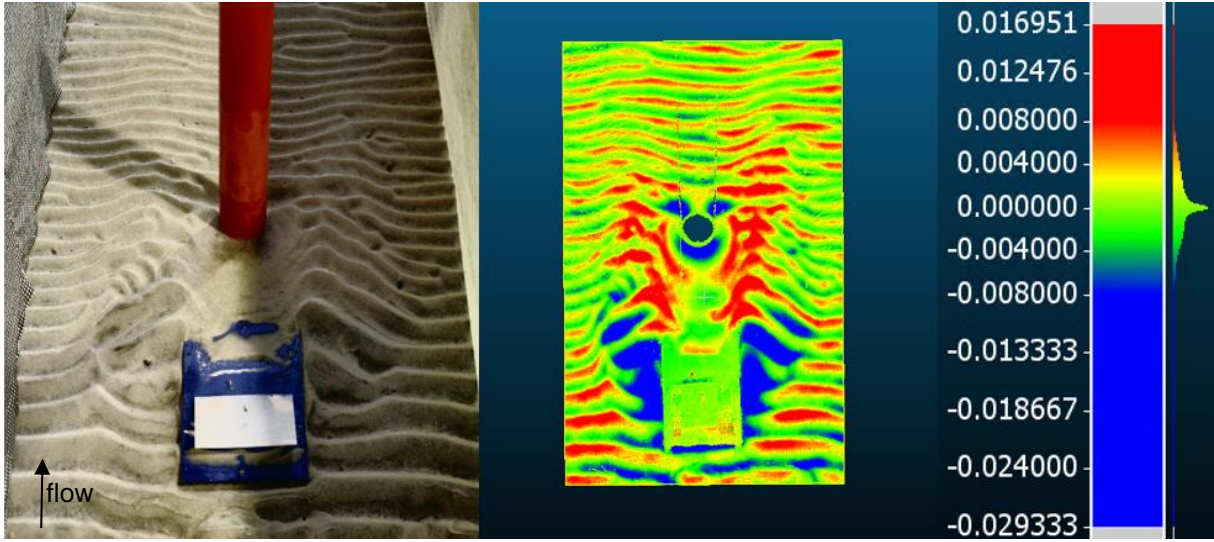


Figure 99 - "WEC2" Monopile scour patterns; Scour grading scale in meters.

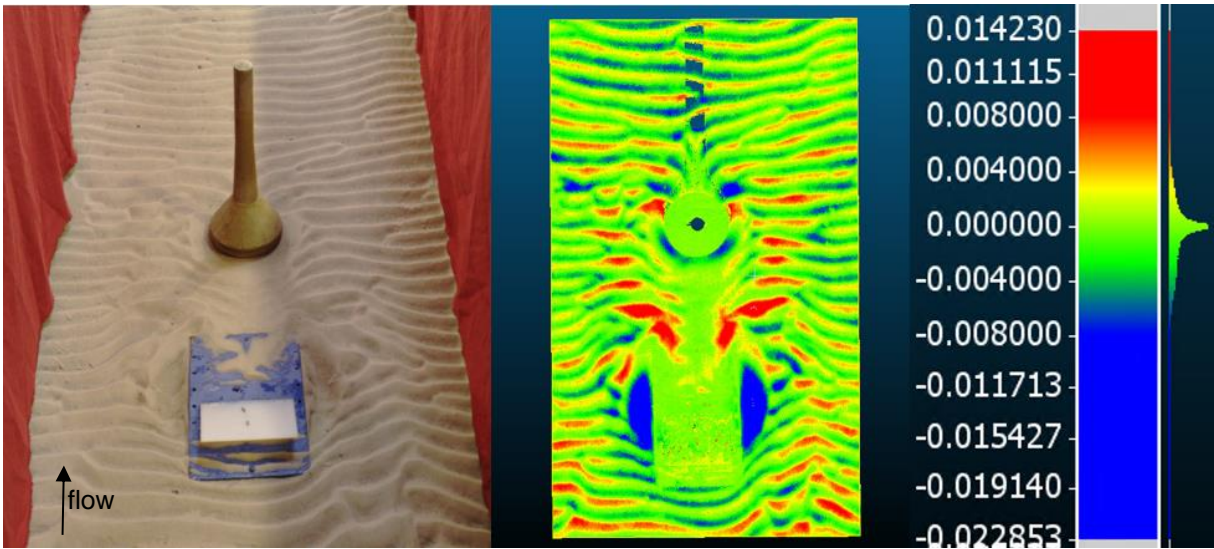


Figure 100 - "WEC2" GBF scour patterns; Scour grading scale in meters.

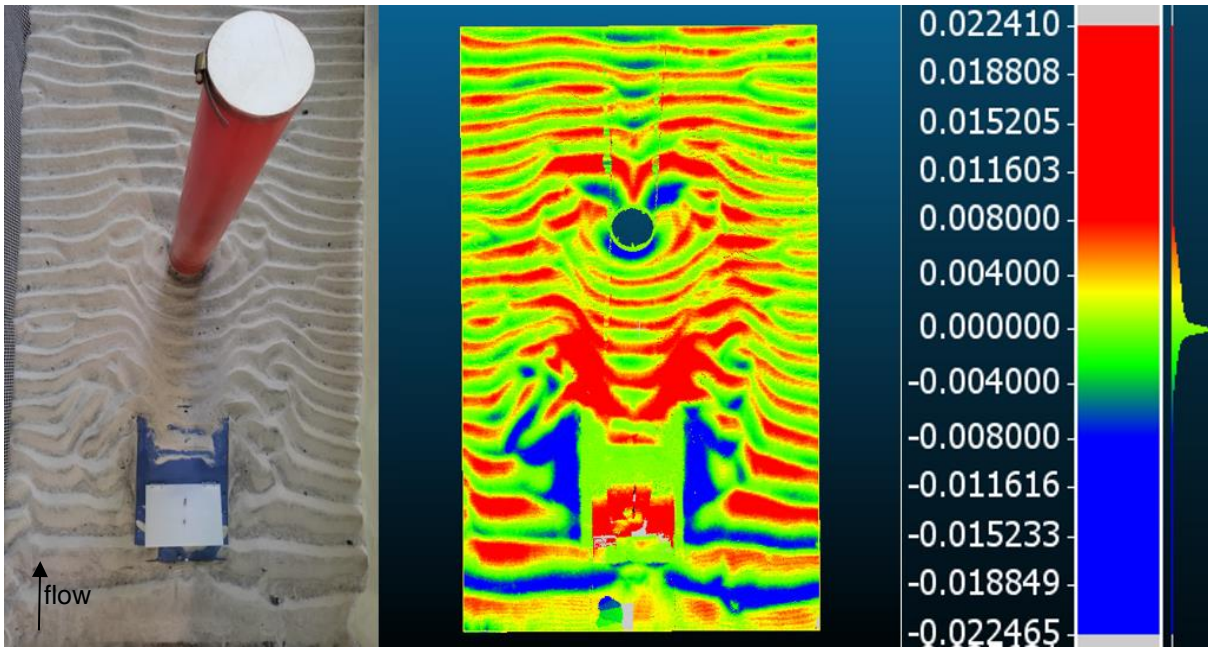


Figure 101 - "WEC3" Monopile scour patterns; Scour grading scale in meters.

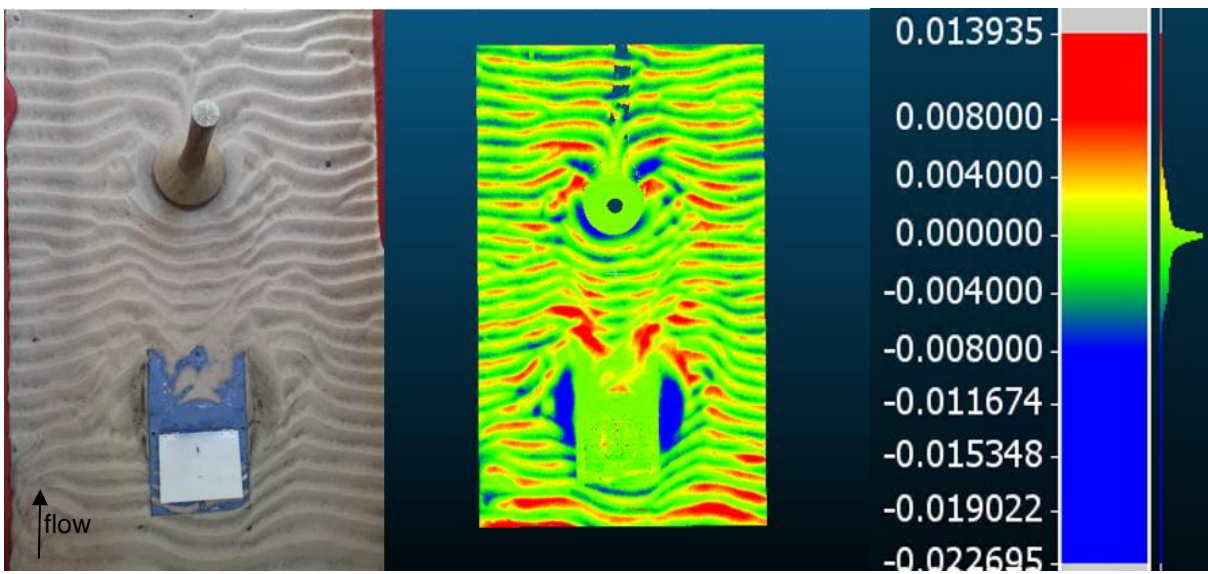


Figure 102 – "WEC3" GBF Scour patterns; Scour grading scale in meters.

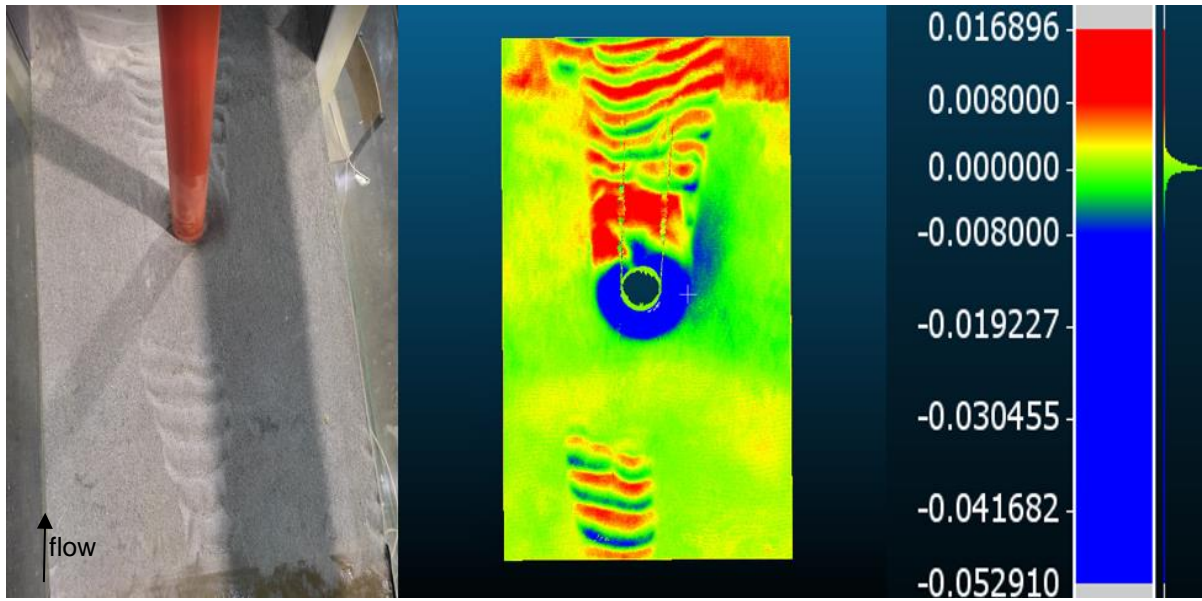


Figure 103 - "Waves 2" Monopile scour patterns; scour grading scale in meters.

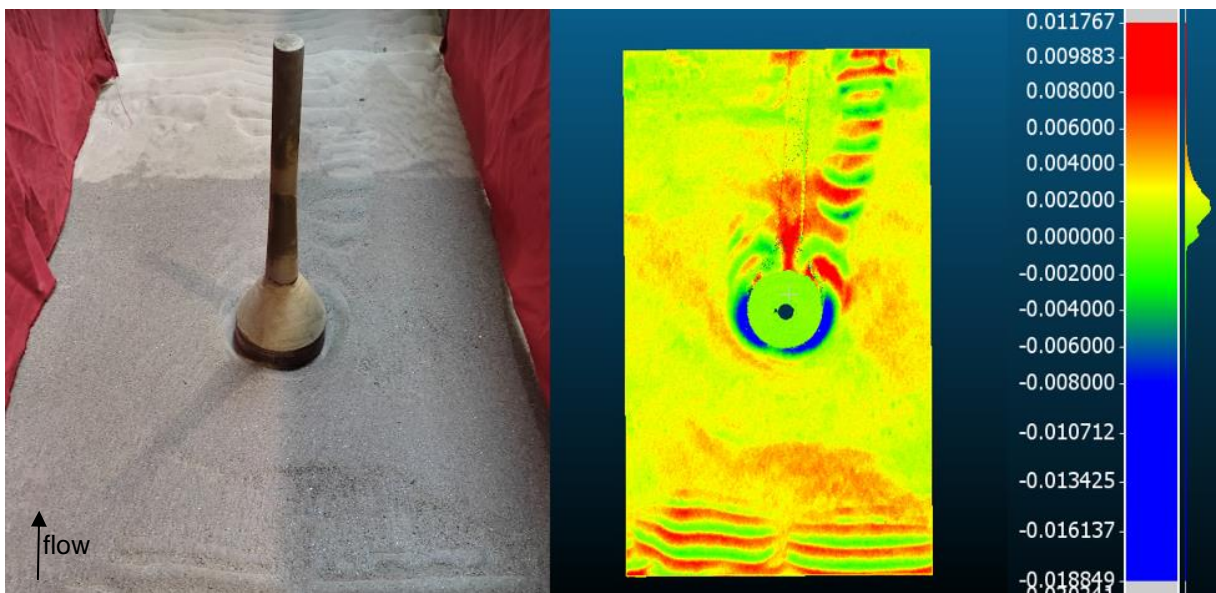


Figure 104 - "Waves 2" GBF scour patterns; Scour grading scale in meters.

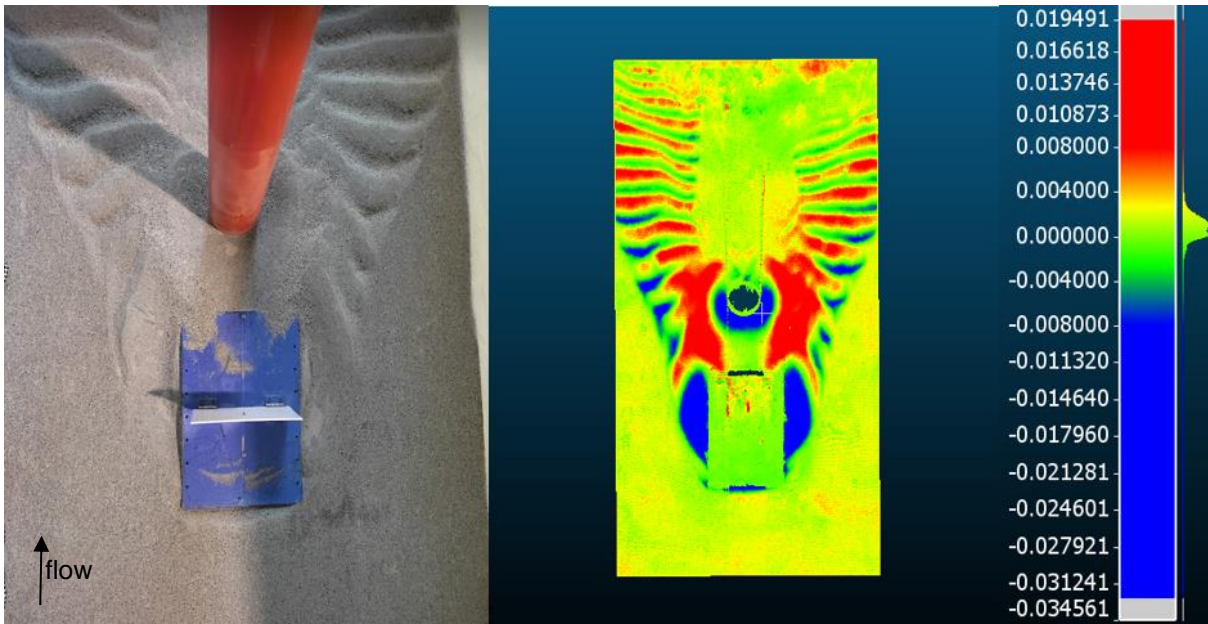


Figure 105 - "WEC4" Monopile scour patterns; Scour grading scale in meters.

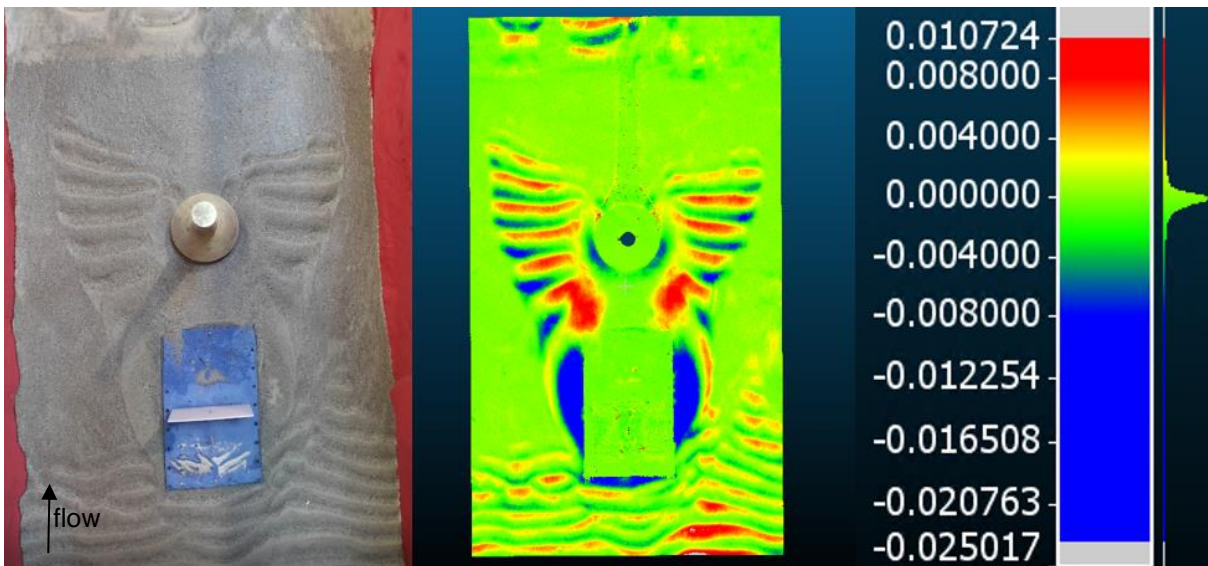


Figure 106 - "WEC4" GBF scour patterns; Scour grading scale in meters.

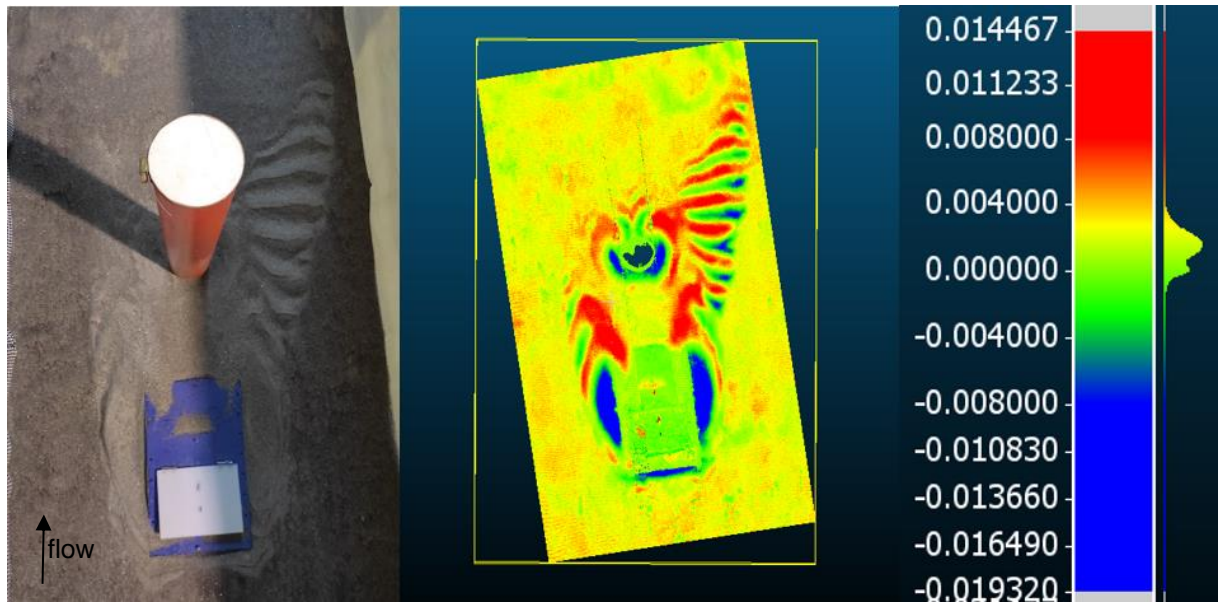


Figure 107 - "WEC5" Monopile scour patterns; Scour grading scale in meters.

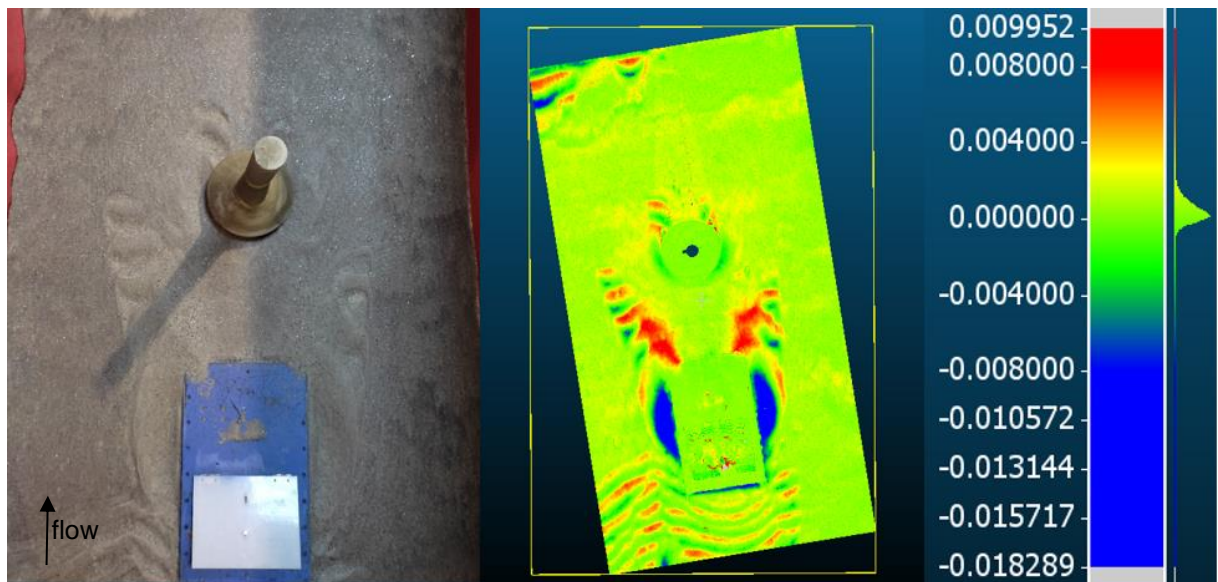


Figure 108 - "WEC5" GBF scour patterns; Scour grading scale in meters.

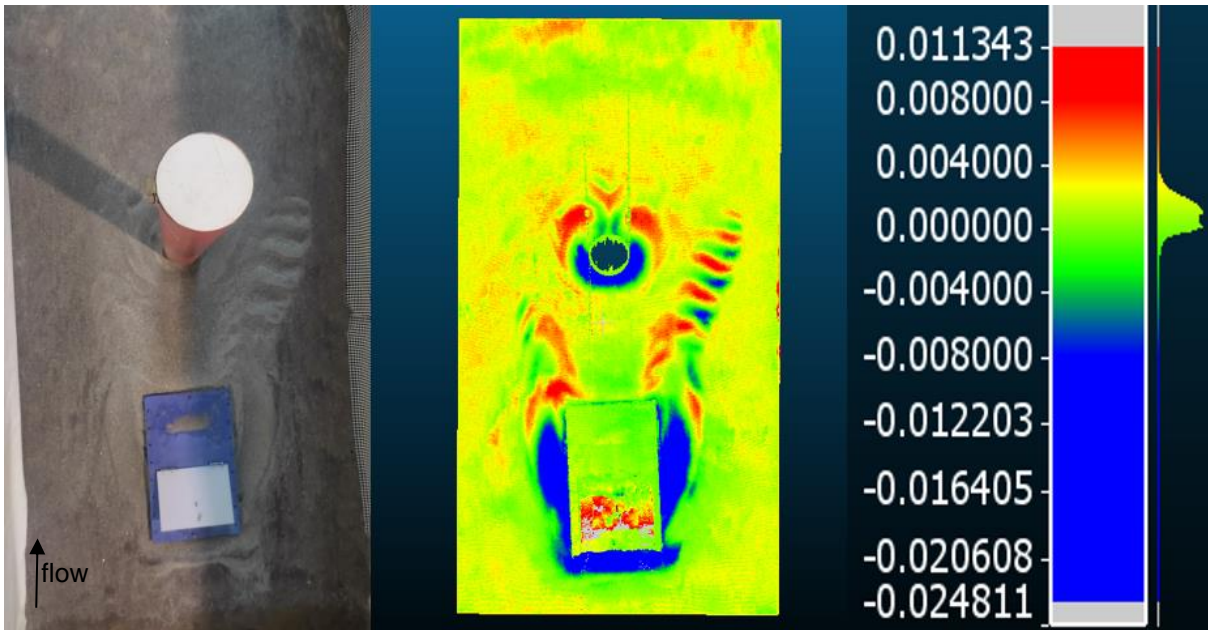


Figure 109 - "WEC6" Monopile scour patterns; Scour grading scale in meters.

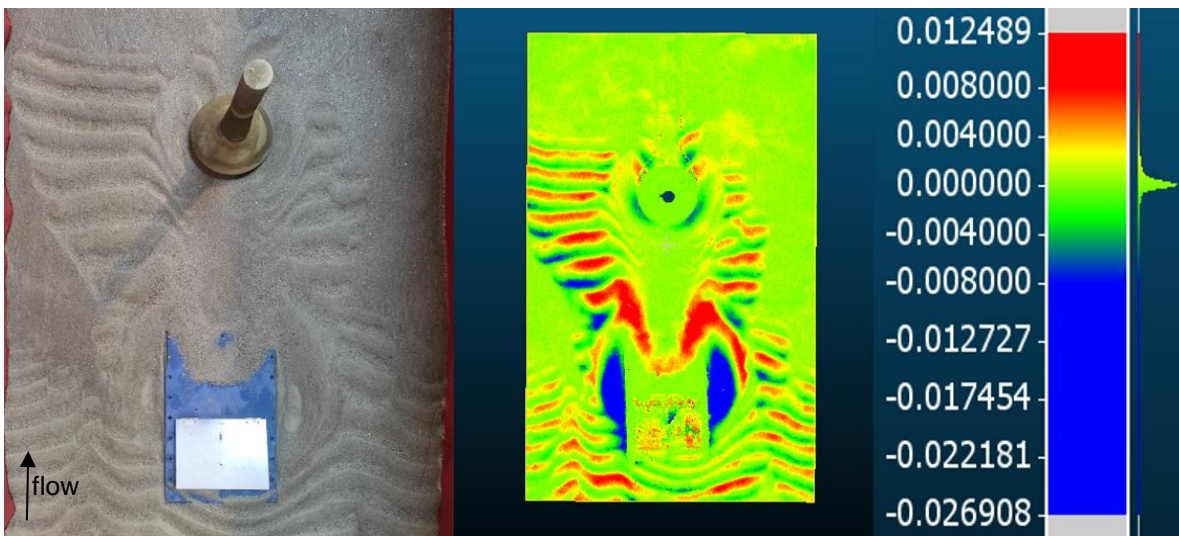


Figure 110 - "WEC6" GBF scour patterns; Scour grading scale in meters.